

CONSTRAINING NUCLEAR WEAK INTERACTIONS IN
ASTROPHYSICS AND NEW MANY-CORE ALGORITHMS FOR
NEUROEVOLUTION

By

Christopher James Sullivan

A DISSERTATION

Submitted to
Michigan State University
in partial fulfillment of the requirements
for the degree of

Physics — Doctor of Philosophy
Computational Mathematics, Science and Engineering — Dual Major

2018

ABSTRACT

CONSTRAINING NUCLEAR WEAK INTERACTIONS IN ASTROPHYSICS AND NEW MANY-CORE ALGORITHMS FOR NEUROEVOLUTION

By

Christopher James Sullivan

Weak interactions involving atomic nuclei are critical components in a broad range of astrophysical phenomenon. As allowed Gamow-Teller transitions are the primary path through which weak interactions in nuclei operate in astrophysical contexts, the constraint of these nuclear transitions is an important goal of nuclear astrophysics.

In this work, the charged current nuclear weak interaction known as electron capture is studied in the context of stellar core-collapse supernovae (CCSNe). Specifically, the sensitivity of the core-collapse and early post-bounce phases of CCSNe to nuclear electron capture rates are examined. Electron capture rates are adjusted by factors consistent with uncertainties indicated by comparing theoretical rates to those deduced from charge-exchange and β -decay measurements. With the aide of such sensitivity studies, the diverse role of electron capture on thousands of nuclear species is constrained to a few tens of nuclei near $N \sim 50$ and $A \sim 80$ which dictate the primary response of CCSNe to nuclear electron capture. As electron capture is shown to be a leading order uncertainty during the core-collapse phase of CCSNe, future experimental and theoretical efforts should seek to constrain the rates of nuclei in this region.

Furthermore, neutral current neutrino-nuclear interactions in the tens-of-MeV energy range are important in a variety of astrophysical environments including core-collapse supernovae as well as in the synthesis of some of the solar systems rarest elements. Estimates for inelastic neutrino scattering on nuclei are also important for neutrino detector construction

aimed at the detection of astrophysical neutrinos. Due to the small cross sections involved, direct measurements are rare and have only been performed on a few nuclei. For this reason, indirect measurements provide a unique opportunity to constrain the nuclear transition strength needed to infer inelastic neutrino-nucleus cross sections. Herein the (${}^6\text{Li}$, ${}^6\text{Li}'$) inelastic scattering reaction at 100 MeV/u is shown to indirectly select the relevant transitions for inelastic neutrino-nucleus scattering. Specifically, the probes unique selectivity of isovector-spin transfer excitations ($\Delta S = 1$, $\Delta T = 1$, $\Delta T_z = 0$) is demonstrated, thereby allowing the extraction of Gamow-Teller transition strength in the inelastic channel.

Finally, the development and performance of a newly established technique for the sub-field of artificial intelligence known as neuroevolution is described. While separate from the physics that is discussed, these algorithmic advancements seek to improve the adoption of machine learning in the scientific domain by enabling neuroevolution to take advantage of modern heterogeneous compute architectures. Because the evolution of neural network populations offloads the choice of specific details about the neural networks to an evolutionary search algorithm, neuroevolution can increase the accessibility of machine learning. However, the evolution of neural networks through parameter and structural space presents a novel divergence problem when mapping the evaluation of these networks to many-core architectures. The principal focus of the algorithm optimizations described herein are on improving the feed-forward evaluation time when tens-to-hundreds of thousands of heterogeneous neural networks are evaluated concurrently.

Copyright by
CHRISTOPHER JAMES SULLIVAN
2018

ACKNOWLEDGMENTS

There are many students, staff, faculty, friends, family, and others whom I regret having not listed in these acknowledgments by name. To each and everyone of you, thank you for the role you have played in this season of my life.

I must begin by thanking my advisor, Remco Zegers. Remco's leadership has been unparalleled, knowing not only when to direct and when to withdraw, but also recognizing potential and encouraging growth in ways that were genuinely for my benefit alone. His scientific expertise and vision for the field of nuclear astrophysics is as accessible as it is energizing. Under his guidance I have been able to cultivate my identity as a physicist and as a computational scientist and have been supported uniformly along both paths. Remco, your passionate commitment to science, service, and stewardship is remarkable and I am truly honored to have been exposed to your level of professional investment on a daily basis.

I also owe the other members of the charge-exchange group a debt of gratitude. Every member of that group has aided in the efforts described in this work. Thank you all for your insight over the years, your willingness to travel with me to Japan for the ${}^6\text{Li}$ measurement, and for the intentionality each of you brought to making the group a friendly and welcoming place to grow.

I must also thank each of the members of my thesis committee, Drs. Dirk Colbry, Sean Couch, Morten Hjorth-Jensen, Sean Liddick, Hendrik Schatz, (and Ed Brown in my first few years). They, as much as I, have seen my interests grow and evolve over the past several years. Thank you for your continued guidance and for providing me with the space to mature in those areas which I am most energized. Thank you Morten for recognizing my passion for computational science and suggesting I pursue it as part of my degree. Your relentless

optimism and encouragement is contagious.

Many thanks are also in order for Evan O'Connor, whose willingness to partner with an experimental group to achieve the sensitivity study outlined in this work was exceptional. His mentorship during our time at CITA and thereafter were some of my first experiences in collaborative scientific software development. Thank you for your helpful explanations of the physics and numerics and for being an excellent collaborator.

I am also particularly thankful for the sense of community among the MSU and NSCL graduate students, and for a number of close relationships I've developed over the years. I had the great fortune of joining MSU in 2012 with Charles Loelius, Eric Lunderberg, and Sam Lipschutz, who have been constant companions throughout the past six years. It has been a pleasure to learn, laugh, and complain with each of you. To my officemates, it was an honor to see you grow, to work beside you, and to be consistently inspired by your stewardship to our communities. In response to the thesis acknowledgments of Chris Morse: in fact, suggesting that you pursue a Physics degree at Westmont was likely one of the most lucrative actions of my professional career. You have been an always willing and capable source of advice and mentorship over the past decade, and I am thankful for your close friendship.

The unwavering love and support of my mother, Theresa Sullivan, and my grandparents, Ronald and Martha Sullivan, cannot be overstated. You have invested in me and my education in ways that only very few people experience. While your involvement in my Ph.D. has looked different than when I was young, it was equally foundational. I also must thank my mother and father-in-law, Chris and Jim Hansen, who have been extraordinary in their selfless support and encouragement. To both the Hansens and the Sullivans, your radical generosity and love have brought genuine vitality to Rachel and I during many long months

of my degree, and for that I am eternally grateful.

Finally, to Rachel Sullivan, my spouse and closest friend, I owe nearly all of my accomplishments over these past years in Michigan to you. In a period of life that is statistically plagued with doubt, anxiety, and depression, you have filled my life with continuous joy and purpose. I am beyond privileged to have had your unceasing love and support at every stage of my academic career, from secondary school until now. Thank you for your love, your willingness to uproot with me, and for your encouragement to reach past what was easy and well beyond what I would have ever been capable of otherwise.

PREFACE

*The fence we walked between the years
Did balance us serene
It was a place half in the sky where
In the green of leaf and promising of peach
We'd reach our hands to touch and almost touch the sky
If we could reach and touch, we said,
'Twould teach us, not to, never to, be dead*

*We ached and almost touched that stuff;
Our reach was never quite enough.
If only we had taller been
And touched God's cuff, His hem,
We would not have to go with them
Who've gone before,
Who, short as us, stood as they could stand
And hoped by stretching tall that they might keep their land
Their home, their hearth, their flesh and soul.
But they, like us, were standing in a hole*

*O, Thomas, will a Race one day stand really tall
Across the Void, across the Universe and all?
And, measured out with rocket fire,
At last put Adam's finger forth
As on the Sistine Ceiling,
And God's hand come down the other way
To measure man and find him Good
And Gift him with Forever's Day?
I work for that*

*Short man, Large dream
I send my rockets forth between my ears
Hoping an inch of Good is worth a pound of years
Aching to hear a voice cry back along the universal mall:
We've reached Alpha Centauri!
We're tall, O God, we're tall!*

Ray Bradbury
NASA Mariner 9 Symposium
Nov. 12, 1971, Caltech

TABLE OF CONTENTS

LIST OF TABLES	xi
LIST OF FIGURES	xii
Chapter 1 Introduction	1
1.1 Nuclear weak interactions	3
1.2 Accessible machine learning via neuroevolution	7
Chapter 2 The sensitivity of core-collapse supernovae to nuclear electron capture	12
2.1 Astrophysical weak interaction rates	16
2.2 Core collapse and the role of electron capture	23
2.3 Codes & Methods	25
2.3.1 NuLib	25
2.3.2 GR1D	26
2.3.3 Neutrino emission via electron capture	27
2.4 Sensitivity study	30
2.4.1 Reference simulations	30
2.4.2 Species dependent sensitivity	33
2.4.3 Systematic variations	38
2.4.3.1 Progenitor model sensitivity	45
2.4.4 Monte-Carlo variations	48
2.5 Conclusion	51
2.5.1 Most important nuclei	52
2.5.2 Impact of uncertainties	53
2.5.3 Goals for future studies	54
2.6 Updates	54
2.6.1 Implementation procedure for future updates	57
Chapter 3 The (${}^6\text{Li}$, ${}^6\text{Li}' + \gamma$) reaction	59
3.1 Experiment	63
3.1.1 The CAGRA+Grand Raiden Coincidence Setup	65
3.1.1.1 Grand Raiden Spectrometer	65
3.1.1.2 CAGRA	66
3.2 Methods & Analysis	70
3.2.1 Data acquisition and analysis framework	70
3.2.2 Grand Raiden calibrations	73
3.2.2.1 Sieve-slit scattering angle reconstruction	73
3.2.2.2 Energy calibration	75
3.2.3 CAGRA calibrations	77
3.2.3.1 Energy calibration	77

3.2.4	Invariant missing mass reconstruction	79
3.2.5	Doppler reconstruction	82
3.2.6	Excitation energy resolution	83
3.2.7	Cross-section calculations	86
	3.2.7.1 Normalization of the number of incident particles	88
	3.2.7.2 Multipole Decomposition Analysis	89
3.3	Results	95
3.3.1	The $^{12}\text{C}(^6\text{Li}, ^6\text{Li}' + \gamma)$ measurement	95
3.3.2	The $(^6\text{Li}, ^6\text{Li}')$ unit cross-section	103
3.3.3	Competition with isoscalar resonances	108
3.4	Conclusion	112
Chapter 4	Many-core algorithms for topologically divergent neural networks	114
4.1	Applications in physics	118
4.2	Network Structures & Evaluation	121
4.3	Directed acyclic graph concurrency	124
	4.3.1 Topological connection sort	125
	4.3.2 Neural network operations	130
	4.3.2.1 Neural network node lifecycle	131
	4.3.3 Generalized concurrent neural network evaluation	132
4.4	Composite population evaluation	135
4.5	CUDA implementation	138
	4.5.1 Performance results	140
4.6	Conclusion	144
Chapter 5	Summary & Outlook	146
BIBLIOGRAPHY	151

LIST OF TABLES

Table 2.1: Density, temperature and mass ranges for the compiled weak rate set . . .	18
Table 4.1: Neural network connection dependency comparator	129

LIST OF FIGURES

<p>Figure 1.1: Diagrams of the weak interactions studied in this work, and the corresponding strong-force reactions that were utilized to indirectly extract the relevant nuclear transitions. As can be seen in the Charged-Current (CC) column of the diagram, even though nuclear charge-exchange is mediated by a π^+ meson instead of the weak W^+ boson for electron capture, the operator responsible for the nuclear transition, $\hat{O}(GT_+)$, is the same in both reactions. This implies that charge-exchange can be used as a surrogate or indirect measurement of the nuclear matrix element relevant for electron capture. Similarly, in the Neutral-Current (NC) channel, nuclear probes can be used to estimate the response of nuclei to inelastic excitation via neutrinos, if the GT_0, component of the M1 operator can be extracted. This is the case for certain proton inelastic scattering measurements, and in chapter 3, ${}^6\text{Li}$ inelastic scattering is shown to be directly sensitive to these weak NC transitions.</p>	6
<p>Figure 2.1: Chart of the nuclear species depicting the nuclei included in each rate tabulation as well as the full reach of the weak rate library presented in this work. The table to which a species belongs is given by the color and legend in the figure. The Oda set contains rates for lower mass sd-shell nuclei (light blue), the LMP set contains rates for the intermediate mass pf-shell nuclei (green), and the LMSH set contains rates for the heavier mass pf/sdg-shell nuclei near stability (red). The FFN tabulation provides rates across the sd and pf-shells (dark blue). Squares individually bordered in black are stable nuclei. The tables are mutually exclusive except for FFN which spans many nuclear shells. To distinguish between nuclei with rates from FFN and another table, the border of the FFN set has been outlined with a black and white line.</p>	19
<p>Figure 2.2: Panel (a): Q-value dependence of electron-capture rates at two points along a core-collapse trajectory. The scattered points are tabulated (shell-model and SMMC) rates for each electron-capture reaction, while the black points are the approximate rates given by Eq. 2.1. Panel (b): The residual differences between \log_{10} of the shell-model rates and the approximate rates for each nucleus in the weak-rate library. An example residual is indicated on panel (a). When the density and temperature of a simulation evolve outside the range of the rate tables (see Table 2.1), rates are calculated via the approximate routines in order to avoid an artificial cut off imposed by the table boundaries. Rates are estimated between density and temperature grid points via monotonic cubic-spline interpolation as described by Steffen [63].</p>	21

- Figure 2.3: The average nuclear mass (divided by two), charge, and electron-capture rate versus central density for the three EOS utilized in this study. The colors indicate different EOS, while the line style indicate which quantity is plotted. All three EOS have nearly identical abundance distributions up to densities of $2 \cdot 10^{12} \text{ g cm}^{-3}$. Beyond this point the TMA EOS has a heavier and slightly more neutron rich mass distribution compared to both SFHo and DD2, but maintains a comparable average electron capture rate overall. These simulations each utilize the s15WW95 progenitor. 32
- Figure 2.4: The contribution of nuclear electron capture to the change of the matter electron-fraction with time. The contours are the binned sums of $|\dot{Y}_e|$ for each species in several mass regions. For reference, the central density at $t - t_b = -20, -10, -5, -2,$ and -1 ms is $1.41 \cdot 10^{11}, 4.06 \cdot 10^{11}, 1.42 \cdot 10^{12}, 8.49 \cdot 10^{12}, 3.30 \cdot 10^{13} \text{ g cm}^{-3}$ respectively. 35
- Figure 2.5: Top 500 electron capturing nuclei with the largest absolute change to the electron fraction up to neutrino trapping. The color scale indicates $|\dot{Y}_e|$ integrated up to the trapping time, occurring when $\rho_c \sim 2 \cdot 10^{12} \text{ g cm}^{-3}$, such that the total electron-fraction at this point is equal to its initial value less the sum of ΔY_e , the plotted quantity, over all nuclides. Calculations are based on the s15WW95+SFHo reference simulation. The black contour that runs parallel to the valley of stability on the neutron-rich side is the boundary between measured [77] and theoretical masses used in the approximate rate estimates of Eqs. 2.1 and 2.2. The rectangular outline indicates the size of the sampling region used in the statistical resampling study, and also the set of nuclei which exhibited the largest changes to the simulations when excluded from the electron-capture calculations. . . 36
- Figure 2.6: Projection of the (trapped) lepton fraction at $\rho_c = 4 \cdot 10^{12} \text{ g cm}^{-3}$ as a function of the electron-capture rate scaling factor for progenitor+EOS reference simulation. In all the cases the lepton fraction begins to increase if the capture rate becomes too high because of a dramatic increase in the electron neutrino absorption cross section. The asymmetry seen here indicates that those quantities which depend on $Y_{l/e}$ are likely to be more sensitive to a reduction of the electron-capture rates due to a systematic overestimate in the base rates, than they are to an increase due to an underestimate. 39
- Figure 2.7: Comparison of the central electron, electron-neutrino (left) and lepton (right) fractions in which the nuclear electron-capture rate for every species has been scaled by factors shown in the legend. Warmer colors indicate a higher overall electron capture rate, and cooler colors indicate a lower rate. The dashed black line indicates the reference s15WW95+SFHo simulation. 41

Figure 2.8: The electron fraction, entropy, density, and velocity as a function of enclosed mass at four times during a core-collapse simulation, spanning 6 ms around bounce, including the collapse phase just after the onset of neutrino trapping (a), core bounce (b), and 1 ms (c) and 5 ms (d) after bounce during which the shock has begun its outward trajectory. The reference simulation (s15WW95+SFHo) is shown in dashed black. Simulations shown in color have electron-capture rates scaled systematically for all species by factors of 10, 4, 2, 0.5, 0.25, and 0.1. Core bounce ($t - t_b = 0$) shown in panel (b) is defined as when the entropy at the shock front exceeds $3.0 k_b/\text{baryon}$ 42

Figure 2.9: The neutrino luminosity as measured at a radius of 500 km as a function of time after bounce in the s15WW95+SFHo simulation set. Electron-capture rate scaling factors are shown in the legend, where contours with warmer colors have higher rates, and cooler colors have lower rates. While the peak electron-neutrino luminosity is considered particularly stable across core-collapse simulations, it varies significantly with variations of the electron-capture rates on medium-heavy nuclei. When the rates are at their lowest ($\times 0.1$ case), the shock reaches the neutrinosphere more quickly than in the other simulations. This results in a larger luminosity in the peak electron-neutrino burst because more ν_{es} are able stream out of the core at early times. The opposite is true when the rates are higher, the neutrinosphere and shock converge much more slowly, and so the neutrinos spend more time diffusing out of the inner core, reducing the peak luminosity but distributing it out to later times. 44

Figure 2.10: The full range of sensitivity of the PNS inner-core mass, central entropy, and central temperature at bounce as well as the peak ν_e -luminosity, the peak average ν_e energy, and the average ν_e energy prior to neutrino trapping, owing to variations of the progenitor model and electron-capture rates. Thirty two progenitors were utilized from the WH07 model set of Woosley and Heger [79] for producing the progenitor bars (red) in the figure. Each bar of the electron-capture rate variations derives from simulations where the rates have been systematically scaled by factors of 10, 4, 2, 0.5, 0.25, and 0.1. The horizontal tick represents the value of the reference simulation for the tested Progenitor + EOS combination. The window ranges are chosen so that the progenitor sensitivity bars are of equal size across each of the plotted parameters. 46

Figure 2.11: Lepton fraction band as a function of central density for the Monte Carlo (MC) described in the text. The band represents data points from seven MC simulations based on the s15WW95+SFHo reference, where the band width represents the min to max range of Y_l . The rates are varied by drawing from the Q-value dependent residual function shown in Figure 2.2 after binning it into 2.5 MeV energy bins. This binning was chosen as it best tracks the Q-value dependence of the residual distribution.	50
Figure 2.12: Updated version of Figure 2.1 showing the addition of the recently added rate tabulations since the libraries first implementation in [2].	55
Figure 3.1: A simplified level diagram of ${}^6\text{Li}$ based on Ref. [103]. The α decay of the $J^\pi = 0^+, T = 1$ state at $E_x = 3.56$ MeV is parity-forbidden, and thus this state mainly decays to the ground state via γ emission.	63
Figure 3.2: The primary facility beam line layout for the Research Center for Nuclear Physics (RCNP) located at Osaka University, Japan. In this experiment, the ${}^6\text{Li}$ beam was transported from the ring cyclotron (shown in green) into the WS hall. It was then transported achromatically to the Grand Raiden target position. See text for details.	64
Figure 3.3: Top panel: Layout of the Grand Raiden Spectrometer which was used to momentum analyze the inelastically scattered ${}^6\text{Li}$ nuclei. The spectrometer was configured with seven magnets in the QSQDMDD configuration (where Q, D, S, and M are Quadrupole, Dipole, Sextupole, and Multipole magnets, respectively). Bottom panel: configuration of the spectrometer end station and focal-plane detectors. Figure adapted from [106, 95]. See text for details.	67
Figure 3.4: The CAGRA array of HPGe clover detectors. CAGRA consisted of two rings of clover detectors with 8 detector slots at 90 degrees and 4 at 135 degrees. There were also 4 forward slots for LaBr ₃ detectors at 45 degrees, but they were not used in this work due to their large angular coverage which made Doppler reconstruction challenging.	68
Figure 3.5: The range of energies the 3.56 MeV γ -ray from ${}^6\text{Li}$ in the laboratory frame. The γ -ray emitted from the de-excitation of the ${}^6\text{Li}[0^+; T = 1; 3.56\text{MeV}]$ state is 3.56 MeV in the rest frame of ${}^6\text{Li}$. In the laboratory frame this gamma is Doppler boosted due to the momentum of the ${}^6\text{Li}$ ($\beta \sim 0.43$), according to its emission angle in the lab-frame. Shown in red are the clover crystal positions in the CAGRA array. Each clover has crystals at two distinct azimuthal angles. Thus, the two rings of clover detectors span for separate angular ranges. For the purpose of Doppler reconstruction, the centroid of the clover crystal is used as the gamma interaction point.	69

Figure 3.6:	The analysis software stack that was used in the RCNP CAGRA+Grand Raiden campaign. Dashed blue lines show application and library boundaries. Solid arrows that cross these boundaries represent communication by local memory, shared memory or disk I/O. See text for details. . . .	71
Figure 3.7:	The image of the sieve slit in the focal plane for 3 separate magnetic rigidity settings (left) and the reconstructed scattering angles at the target using a least squares fit to Eqs. 3.6 & 3.7 (right).	74
Figure 3.8:	The time-dependence of the Grand Raiden energy calibration for the centroid of the $^{12}\text{C}[2^-;T=1;19.4\text{ MeV}]$ state in the $^{12}\text{C}(^6\text{Li},^6\text{Li}')$ excitation energy spectrum. Due to the coincident excitation of the ^6Li ejectile to its 3.56 MeV state, this isovector state in ^{12}C appears at $\sim 23\text{ MeV}$ ($=19.4\text{ MeV} + 3.56\text{ MeV}$).	76
Figure 3.9:	Rate dependence of the CAGRA clover crystals. Panel (a) shows an example count rate spectrum as a function of time for the CAGRA array. Panel (b) details the rate dependence of the energy calibration offset for a specific HPGe crystal in the array. This trend was established for each crystal and then used to correct the energy calibration on a second-by-second basis. Panels (c) and (d) show the rate dependent gamma-ray energy and (corrected) rate independent gamma-ray energy for the 511 keV line, respectively.	78
Figure 3.10:	The kinematics of the ^6Li reaction.	80
Figure 3.11:	(a) A comparison of the contribution of the intrinsic energy resolution, opening angle uncertainty, and velocity spread of the ejectile, to the overall uncertainty in the Doppler reconstructed gamma-ray energy for the detection of the 3.56 MeV de-excitation gamma from ^6Li in CAGRA. The uncertainty in the emission angle of the γ -ray is the dominant component of the overall resolution. (b) The resulting estimated resolution of the reconstructed invariant ^6Li ejectile given the resolution of the measured de-excitation gamma.	82

Figure 3.12: Comparison of the simulated reconstruction of the $^{12}\text{C}[1+;T=1;15.1\text{ MeV}]$ excited state with the measured result. In the left panel, the purple line represents the (simulated) best-case scenario for the missing mass reconstruction of the 15.1 MeV peak, if the invariant $^6\text{Li}[0+;T=1;3.56\text{ MeV}]$ is ignored. By comparing this with the data in the right panel, it is apparent that the data follows a much broader distribution. In order to reproduce the data, the simulated missing mass reconstruction of this state in ^{12}C (purple) had to be smeared with a gaussian of a variety of widths. The shape of the smeared state was interpolated and fit to the data using a normalization factor. The best fit was found with a gaussian smearing of FWHM=1.75 MeV (shown by the black scatter crosses and red line in the left and right panels, respectively). The smearing that was required suggests that the intrinsic beam energy resolution was 1.75 MeV. 85

Figure 3.13: Calculated angular distributions for isovector spin-transfer excitations of different orbital angular momentum transfer for the $^{12}\text{C}(^6\text{Li},^6\text{Li}')$ inelastic scattering measurement. Each panel is the angular distribution for a particular angular momentum multipole, and the different color lines are the excitation energy (Q-value) dependence of the angular distribution. 93

Figure 3.14: The gamma-ray energy and target excitation energy matrix for the $^{12}\text{C}(^6\text{Li},^6\text{Li}'+\gamma)$ reaction. In the top panel, the gamma energies shown are those measured in the detectors, without any transformation applied and in the bottom panel, the gamma energies have been Doppler reconstructed according to the clover crystal angular positions. Both panels are drawn as a function of the excitation energy in ^{12}C which is calculated via the missing mass formalism. The red arrow in the top panel indicates the width of the $^{12}\text{C}(15.1\text{ MeV})$ state owing to the momentum kick that is imparted to the ^6Li and which is not accounted for in the missing-mass-only reconstruction. This width is analogous to the FWHM of the excitation energy spectrum shown in Figure 3.12. By comparing the two panels, the effect of the doppler reconstruction can be seen, where the photopeak and Compton edge owing to the 3.56 MeV gamma from ^6Li is more prominent in the bottom panel after reconstruction. In addition, gamma decay from the strong isoscalar resonance (occurring above 20 MeV in excitation energy) is clearly evident. 96

Figure 3.15: The Doppler-corrected γ -ray energy gated on the $^{12}\text{C}[15.1\text{ MeV}; T=1]$ state for emphasis. The 3.56 MeV γ -line from the $^6\text{Li}[0+; T=1]$ excited state is clearly evident. The resolvability of this γ -ray is crucial for tagging isovector spin-transfer reactions in the target nucleus. The inset plot compares the signal to noise achieved with the clover detectors to what is expected were a gamma-ray tracking detector was utilized. See text for details. 97

- Figure 3.16: The reconstructed excitation energy spectrum of ^{12}C , for different angular bins, when applying the two gates shown in the Doppler-reconstructed gamma energy spectrum (Fig. 3.15). The red spectrum corresponds to the 3.56 MeV photopeak gate, and the blue spectrum corresponds to the sideband, representative of the gamma background in the photopeak gate. The $^{12}\text{C}[1+;T=1;15.1\text{ MeV}]$ state, which is populated via an isovector spin-transfer reaction, is clearly seen in the photopeak gated spectra, but not in the sideband data. 98
- Figure 3.17: Comparison of the ^{12}C inelastic scattering singles and coincidence excitation energy dependent double differential cross section for the $^{12}\text{C}(^6\text{Li}, ^6\text{Li}')$ and the $^{12}\text{C}(^6\text{Li}, ^6\text{Li}' + \gamma)$ reactions, respectively. The coincidence spectrum shown is the result of the subtraction of the differential cross section resulting from a gate on the photopeak of the 3.56 MeV γ -ray and a sideband in the region directly above this gamma (shown as the red and blue cross-hatched regions in Fig 3.15, respectively). The coincidence spectrum corresponds to the isovector spin-transfer excitations in ^{12}C , whereas the singles spectrum contains all types of transitions but is primarily dominated by isoscalar excitations. See text for details. 100
- Figure 3.18: Double differential cross section for the $^{12}\text{C}(^6\text{Li}, ^6\text{Li}' + \gamma)$ reaction as a function of excitation energy and center of mass scattering angle, in which the 3.56 MeV state was measured in coincidence. Due to conservation of spin and isospin, this coincidence measurement extracts the isovector spin-transfer response of ^{12}C . In addition, a multipole decomposition analysis (MDA) has been performed utilizing DWBA angular distributions to extract the components of orbital angular momentum transfer. Shown in the right panel are the angular distributions for states in ^{12}C dominated by Gamow-Teller transitions (top panel) and spin-dipole transitions (bottom panel). The absolute scale has a systematic uncertainty of $\pm 20\%$ due to uncertainty in the beam normalization which is not depicted in the statistical error bars. 102

Figure 3.19: The mass dependence of the Gamow-Teller unit cross-section for ${}^6\text{Li}$ calculated from theoretical estimates of the inelastic GT strength and DWBA estimates for the cross section of several nuclei (black). Filled circles indicate that the underlying GT strengths were estimated via shell-model or normal-modes calculations. A postulated unit cross section mass-dependence for heavy-ion reactions (Eq. 3.36) is fit to these theoretical unit cross-sections and is shown in the plot (dashed black line). In addition, the experimentally derived Gamow-Teller UCS for the inelastic (${}^6\text{Li}, {}^6\text{Li}'$) reaction established in this work is shown alongside an estimated unit cross section from data available for the (${}^6\text{Li}, {}^6\text{He}$) charge-exchange reaction [135]. The error bar shown for the inelastic UCS includes systematic and statistical uncertainties, while no error on the charge-exchange data was available. 106

Figure 3.20: Comparison of the achievable signal-to-noise for the 3.56 MeV γ -ray emitted from inelastic scattering of ${}^6\text{Li}$ on ${}^{12}\text{C}$ (top panel), ${}^{24}\text{Mg}$ (middle panel), and ${}^{93}\text{Nb}$ (bottom panel). The Doppler reconstructed gamma is resolvable in the ${}^{12}\text{C}$ measurement but not in the ${}^{24}\text{Mg}$ other measurements. The purple and red line-shapes are the simulated response of the clover and tracking detectors, respectively. In the ${}^{12}\text{C}$ case, the purple line shape is fit to the data, and used to estimate the number of counts in the 3.56 MeV peak. The excitation energy was gated on the 15.1 MeV state in ${}^{12}\text{C}$ which has a $B(\text{GT}) \sim 1$. Assuming a comparable $B(\text{GT})$ in ${}^{24}\text{Mg}$ and ${}^{93}\text{Nb}$, over an equal-width range in excitation energy, and accounting for the change in the unit cross-section with mass, the purple and red line-shapes have been scaled to reproduce the expected number of isovector counts in the other two measurements. This clearly illustrates that resolving the ${}^6\text{Li}$ 3.56 MeV gamma becomes increasingly difficult in heavier systems where the isoscalar giant resonances remain strong. Decay from these resonances contribute a significant background in the region of the 3.56 MeV γ -ray from ${}^6\text{Li}$, and this background increases in magnitude with increasing nuclear mass. 109

Figure 3.21: The differential cross sections for the ${}^{24}\text{Mg}({}^6\text{Li}, {}^6\text{Li}')$ and the ${}^{93}\text{Nb}({}^6\text{Li}, {}^6\text{Li}')$ singles measurements. The cross sections in both cases are dominated by isoscalar giant resonances which become larger with heavier mass systems. 110

Figure 3.22: Mass dependence of the calculated zero-degree differential cross section for the isoscalar giant monopole and dipole resonances (IVGMR and IVGDR, respectively) corresponding to 100% exhaustion of the energy weighted sum-rule. These calculations illustrate the increase in the isoscalar cross-section as a function of nuclear mass number and were provided at the courtesy of Umesh Garg [139]. 111

Figure 4.1:	The basic components an artificial neural network. Each node (shown as the circle in the figure) accumulates inputs modulated by the weights of its inbound connections. After all of the inbound connections have been accumulated into the node, a non-linear activation function, such as a logistic sigmoid, transforms the nodes value. The transformed node value is then used as an output along outbound connections to other nodes in the network.	115
Figure 4.2:	(a) A common feedforward neural-network structure with a single hidden layer. x_i^0 , x_i^1 , and x_i^2 correspond to the input, hidden and output layers respectively, while $w_{ij}^0, 1$ refer to the connection weight matrices between two layers. (b) An unstructured neural network in which the connections are not constrained to specific layers. Such network structure is common in neuroevolution populations. Each connection in (b) is labeled with an integer indicating the lock-free set in which it can be evaluated. See section 4.3.1 for details.	118
Figure 4.3:	An illustration of the structural divergence than can exist in populations of neural networks evolved via neuroevolution. In this case, each network has a fixed number of input and output nodes (3 and 1, respectively).	123
Figure 4.4:	An example neural network and two directed acyclic dependency graphs for the evaluation of the neural network’s connections. The left dependency graph includes only <i>logical</i> dependencies whereas the graph on the right includes both <i>logical & memory</i> dependencies. Each circle in the dependency graphs represent connections in the top neural network figure. The arrows in the two dependency graphs indicate the dependency relationship between the connections . For example, the arrow between A1 and B1 indicates that connection A1 must be evaluated prior to B1. By inspecting the neural network, this relationship is evident as connection B1 relies on node 1, which in turn relies on connection A1 (as well as other connections).	126
Figure 4.5:	Prototype of sorting connections into concurrent lock-free sets. For n connections, scales as $\mathcal{O}(n^2)$	128

Figure 4.6:	The full directed acyclic dependency graphs for two structurally different neural networks. The different symbols in the graph, squares, circles, and triangles, represent the three neural network operations: zero-node, apply-connection, and activate-node, respectively. Even though the two networks have very different structure, the algorithm proposed in this work organizes the network evaluation graphs into evaluations steps that are component-wise parallel. On the right of the figure, each evaluation step is shown with the number of SIMD operations that can be performed simultaneously.	133
Figure 4.7:	Top panel: A representative example population of neural networks consisting of three members. In classic neuroevolution simulations, each of these neural networks are separately evaluated, and the correctness of their outputs is used to judge their fitness. Bottom panel: The same population as in the top panel, but constructed as nodes and connections of a single composite neural network. On the left, the resulting composite network in which each of the constituting sub-networks requires heterogeneous inputs for evaluation. On the right, a composite network in which each of the sub-networks will process the same inputs.	136
Figure 4.8:	NVIDIA CUDA kernels for the proposed concurrent neural network evaluation.	139
Figure 4.9:	GPU speed up factor when evaluating a population of N evolved neural networks concurrently. The ratio of time taken for the sequential evaluation of each network on a single CPU thread to the time for transferring inputs to the device, evaluation on the GPU, and transferring the outputs back to the host. With a population of approximately 65k networks, a performance boost of 50x relative to the serial implementation is observed.	140

Chapter 1

Introduction

Advances in computational capabilities, astrophysical observations, nuclear theory and experimental methods over the past two decades have enabled a new era of multidisciplinary research in the fields of nuclear science and computational astrophysics. For example, we now have the capability of probing the impact of specific nuclear processes to large-scale astrophysical events via sensitivity studies, which can direct new experimental and theoretical efforts [1, 2, 3].

Ultimately, the interdisciplinary nature of these efforts is fundamentally self-sustaining. Experimental measurements for all nuclei relevant to a specific astrophysical context are often unfeasible due to the large number of nuclei that are involved. Therefore, nuclear theory must be relied upon for the majority of the relevant nuclear information, where key measurements can help to constrain theoretical calculations. Then, astrophysical sensitivity studies—which probe the impact of specific nuclear reactions to astrophysical simulations—can reveal the key nuclei that should be studied experimentally and theoretically. These new measurements and calculations then feed back into the astrophysical simulations, constraining the uncertainty of the nuclear physics inputs to the astrophysical phenomenon. Finally, with high fidelity astrophysical simulations, predictions about multi-messenger astronomical observations from such events can be made and verified at earth based electromagnetic, neutrino, and gravitational wave observatories.

In addition, the dramatic increase in computational capabilities and the increasingly large amounts of data that have enabled the above cycle are also fueling growth in the fields of artificial intelligence and machine learning. Specifically, the development of novel algorithmic techniques in machine learning, which take advantage of these computational advancements, are beginning to provide new and less expensive solutions to challenging scientific problems [4, 5].

The research described in this work embodies these principle advancements. In the following sections, the motivation of the projects that compose this body of work are outlined. Each subsequent chapter will focus on the specific implementation of what is presented here, as well as the the scientific results and conclusions that can be drawn. The three research directions that will be discussed are,

Chapter 2. An investigation into the sensitivity of core-collapse supernovae (CCSNe) to the nuclear reaction known as electron capture,

Chapter 3. The establishment of a new experimental method, the (${}^6\text{Li}, {}^6\text{Li}'$) reaction, which can provide access to astrophysically relevant neutrino-nucleus reactions,

Chapter 4. The development of many-core algorithms for topologically divergent neural networks which better enable neuroevolution to compete in the automated machine-learning ecosystem.

While these are quantitatively distinct focuses, each of these projects principally explore new ways to accelerate the process of scientific discovery: sensitivity analyses can direct experimental and theoretical efforts; new experimental techniques can replace or supplement previously difficult-to-study avenues of research; and novel high-performance automated

machine-learning algorithms can reduce the implementation barrier of artificial intelligence in the scientific domain.

1.1 Nuclear weak interactions

The physics motivation of the research presented in this work is largely rooted in the topic of weak interactions with atomic nuclei. The weak interaction is one of the four fundamental physical forces in nature. Weak interactions that involve nuclei include β^\pm -decay (positron/-electron emission), forward and inverse neutrino interactions (nuclear capture of neutrinos and heavy leptons, respectively), and neutrino-nucleus scattering.

In a terrestrial context, weak-processes play an important role in modern technology. For example, beta emitting isotopes are commonly used in medical diagnostics, nuclear medicine, imaging (positron emission tomography; PET-scans), portable energy generation, natural gas production, and radioactive dating [6].

In astrophysics, however, the influence of the weak interaction is pervasive. This is historically evident in that nearly every new insight that has arisen about the weak interaction over the course of the past century has been coupled with significant changes in our understanding of astrophysical processes [7]. For example, after the existence of the neutrino was proposed by Pauli and the first weak-interaction theory was developed by Fermi [8], it was not long before it was suggested and established that the production of weakly-interacting neutrinos is the primary source of energy loss in stars [9]. Following the theory of neutral-current neutrino interactions with nucleons [10], it was recognized that neutrino scattering in core-collapse supernovae would create the phenomenon known as neutrino-trapping, which prevents neutrinos from escaping the collapsing core of a massive star [11, 12] and has a

dramatic impact on the evolution of the supernovae.

The class of weak interactions focused on in this work (those involving interactions with atomic nuclei) are known as semi-leptonic weak interactions, and they fall into two categories: charged- and neutral-current interactions. Subatomic particles interacting via charged-current (CC) and neutral-current (NC) weak interactions are mediated by the W^\pm and Z^0 bosons of the standard model, respectively. Both types of interactions are studied in this work, where electron-capture (a CC reaction) is discussed in chapter 2, and inelastic neutrino-nucleus scattering (a NC reaction) is discussed in chapter 3.

Whereas the unified model for the electro-weak theory can accurately predict weak-interaction cross-sections involving elementary particles, for semi-leptonic weak interactions involving nuclei, the problem is more complex. By treating the weak-interaction with nuclei perturbatively, the calculation of weak-interaction cross-sections can be reduced to the many-body nuclear-structure problem well within the domain of nuclear physics. Unfortunately, the difficulties that arise when solving the many-body nuclear-structure problem often introduce large uncertainties into the weak reaction rates that are important for astrophysics [7, 13]. This suggests that experimental input is necessary. While measurements cannot be made for all of the nuclear weak interactions that are important, they can provide invaluable constraints on theoretical models. This will be discussed in detail in chapter 2.

The complication in the nuclear weak-interaction (the semi-leptonic case) arises principally from the need for detailed information about the nuclear transitions and states that are involved. However, this relationship also implies that if one is able to attain information about the nuclear many-body configurations and transitions involved in the weak reaction, the weak-interaction cross-section and reaction rate can be indirectly constrained. Experimentally, this means that if the direct weak-interaction measurement is difficult or

impossible, as is the case for many astrophysically relevant weak reactions, an indirect measurement which probes the same nuclear transitions can be utilized. The ability to indirectly extract the necessary information to constrain weak reaction rates and cross-sections form the basis for the experimental programs discussed in the following two chapters.

Nuclear charge-exchange and inelastic scattering, as shown in Figure 1.1, are two independent accelerator-based experimental techniques which are capable of inducing the same nuclear transitions as CC and NC weak interactions, but are induced via reactions mediated by the strong force. Also shown in the figure are the two weak reactions studied in this work, electron capture and inelastic neutrino-nucleus scattering.

The similarity between reactions mediated by the weak and the strong force is evident when considering the interaction diagrams, also shown in Figure 1.1. In the case of the electron-capture process, the mediating particle is the W^+ boson, and in charge-exchange reactions the mediating particles are mesons (such as the π^+ meson, and others). In both cases, the interacting nucleus undergoes the same transition between initial and final states, and so both processes probe the same nuclear matrix elements, albeit with separate couplings (weak vs strong). An analogous argument can be made for the inelastic neutrino scattering and the hadronic inelastic scattering shown in the figure; that is, instead of a mediating Z^0 boson, a π^0 meson (for example) is exchanged and the same nuclear transition occurs. However, a few subtleties arise in the NC channel that are reserved for discussion in chapter 3.

These indirect techniques are of immense value primarily because the direct measurements are often extremely challenging. For example, very few neutrino-inelastic scattering measurements on nuclei have been performed to date because of the very small cross-sections involved ($\sim 10^{-42}$ mb/sr). This specific example is the primary motivation for the development of the (${}^6\text{Li}, {}^6\text{Li}'$) reaction probe, and is discussed at length in chapter 3. Even so,

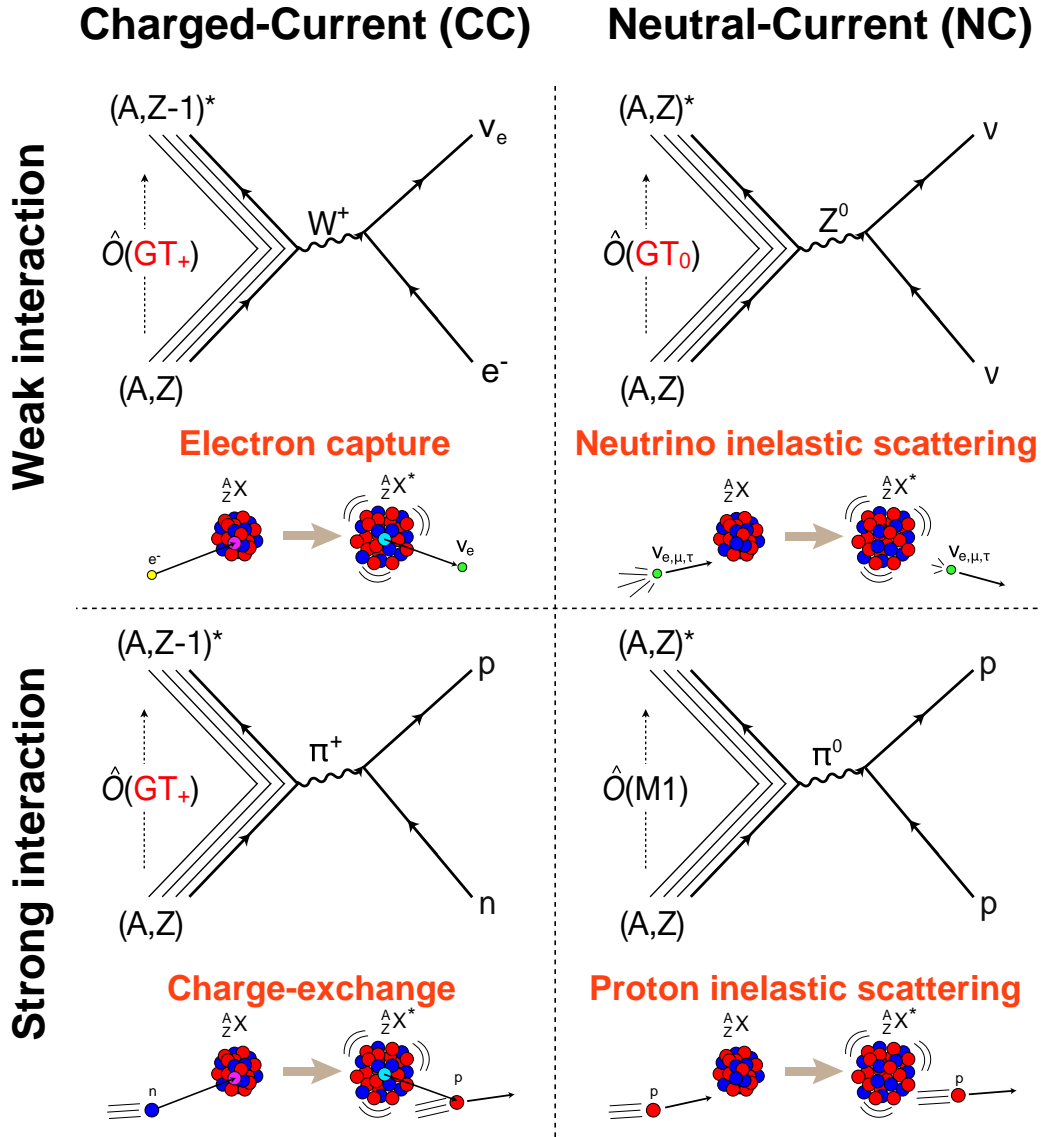


Figure 1.1: Diagrams of the weak interactions studied in this work, and the corresponding strong-force reactions that were utilized to indirectly extract the relevant nuclear transitions. As can be seen in the Charged-Current (CC) column of the diagram, even though nuclear charge-exchange is mediated by a π^+ meson instead of the weak W^+ boson for electron capture, the operator responsible for the nuclear transition, $\hat{O}(GT_+)$, is the same in both reactions. This implies that charge-exchange can be used as a surrogate or indirect measurement of the nuclear matrix element relevant for electron capture. Similarly, in the Neutral-Current (NC) channel, nuclear probes can be used to estimate the response of nuclei to inelastic excitation via neutrinos, if the GT_0 , component of the M1 operator can be extracted. This is the case for certain proton inelastic scattering measurements, and in chapter 3, ${}^6\text{Li}$ inelastic scattering is shown to be directly sensitive to these weak NC transitions.

measurements of *all* the astrophysically relevant nuclei for which weak reactions are important is an impossible task. Thus, those nuclei which are the most important in astrophysical simulations should be measured, providing the best possible constraints for the theoretical methods which are needed to estimate the majority of the weak reactions. It is for this reason that in chapter 2, a sensitivity analysis of core-collapse supernovae to nuclear electron-capture rates is described, and the important weakly interacting nuclei are identified.

While chapters 2 & 3 have fundamentally different focuses, together they represent a coordinated effort to constrain the nuclear weak-response of nuclei through both the charged and neutral current channels. As weak interactions with nuclei are critical components of many astrophysical processes, these constraints strongly impact the field of nuclear astrophysics.

The final chapter of this work departs from discussion of weak interactions in nuclear astrophysics, and instead focuses on algorithmic advancements in artificial intelligence research. This work aims to lower the accessibility barrier of machine learning, and in chapter 4 evidence will be provided that suggest the application of these methods will improve the applicability of modern neural-network classification techniques in experimental nuclear astrophysics.

1.2 Accessible machine learning via neuroevolution

Many efforts in recent years have been directed toward increasing the accessibility of machine learning, through new university programs, internet-based educational opportunities, as well

as the development of high-level programming interfaces that abstract away the mathematical details of building machine-learning models [14, 15, 16, 17]. These efforts have been driven by an increased demand for machine-learning tools and models that can be applied by users with limited machine-learning knowledge, as a result of its numerous successes in a variety of industrial, scientific, and engineering domains.

Unfortunately, while machine learning has the capability to provide novel insights for an extremely diverse set of problem domains, most applications require in-depth knowledge of machine learning techniques in order to arrive at suitable solutions. The reason for this is that the application of machine learning to any problem domain requires at least three principle choices:

1. The choice of the optimal machine learning model for the application;
2. How to pre-process the data for consumption by the chosen model;
3. How the model training parameters (known as the hyperparameters) should be set for a particular dataset.

For the general domain scientist and engineer that wishes to focus on their field of expertise, (1-3) can present a significant obstacle [18]. Even if the scope of (1) is limited specifically to artificial neural networks (ANNs; hereafter simply referred to as neural networks), picking the correct network hyperparameters such as the neural-network topology, learning rate, and others, is a task for which there is no scientifically rigorous method [19]. Instead, hyperparameter searches are often performed manually via rules-of-thumb and by testing large sets of models with a predefined grid of parameter values [20]. While grid-based searches are effective, they are very computationally expensive, and manual searches by hand often require considerable expertise and can lead to poor reproducibility [21]. As methodological

reproducibility is a core tenant of the scientific method, such implementations of machine learning are not viable in scientific applications.

The essence of the hyperparameter problem can be captured in a rudimentary description of supervised learning with neural networks. Supervised learning is a class of machine-learning algorithms which make use of a set of training data (\mathbf{x}, \mathbf{y}) , where the vector of inputs \mathbf{x} are transformed into output estimates $\hat{\mathbf{y}}$ that approximate the true outputs \mathbf{y} . The process is supervised by the provision of data where the expected output response is known, and thus the model itself can be adjusted so that the output response is closely representative of the true desired output response. Mathematically, the problem can simply stated as,

$$\mathcal{F}(\mathbf{x}, \mathbf{w}; \mathcal{C}) = \hat{\mathbf{y}}, \tag{1.1}$$

where \mathcal{F} is the neural network (or other machine learning model), \mathbf{w} are learned parameters of the neural network which are adjusted so that $\hat{\mathbf{y}}$ approaches the true outputs \mathbf{y} , and \mathcal{C} are the model hyperparameters (e.g. the fixed structure of the network, the learning rate, et cetera).

Typically, supervised learning with neural networks follows three steps, a learning phase with training data, a validation phase with testing data, and a prediction phase. In the learning phase, a set of training data is used to solve an optimization problem, where the set of learned parameters are adjusted so that a loss or error function—which represents the difference between the true output response (\mathbf{y}) and the inferred output response ($\hat{\mathbf{y}}$)—is minimized. After this process is complete, two conclusions and consequent actions can be reached: (1) if the neural network performs well on the training data (the loss function is sufficiently minimized), it is then validated with the testing data to see if the model has been

over fit; or (2) the neural-network was unable to sufficiently reproduce the desired output response of the training data (could not minimize the loss function sufficiently). Ascertaining the reason for training failure, as in (2), is a particularly difficult problem to assess, as it may have occurred because of bias in the training data, or the machine-learning model of choice may not be well suited to the application, or the model hyperparameters were ill-chosen, such as the choice of a non-optimal neural-network structure.

In this context, the role of a data scientist [22] is clear: identifying the machine-learning models which will generalize well to a given dataset, and knowing how to increase the model complexity in cases of training failure. However, for the domain scientist who wishes to employ machine-learning as a tool, these choices are not immediately obvious. Furthermore, the process of trial and error is arduous because of the long feedback cycles: in most applications, the training phase takes a non-trivial amount of time. The potentially long delay in feedback regarding the model adjustments makes manually searching the model complexity space excessively burdensome for new users.

The concept of automated machine-learning seeks to remove these complexities, by automating the process of model choice, data processing, and hyperparameter tuning [23]. By doing so, automated methods seek to lower the machine-learning implementation barrier for novice users.

One method that is beginning to see more use in the automated machine-learning space is *Neuroevolution* [24, 25]. Neuroevolution is a form of artificial intelligence that utilizes evolutionary genetic algorithms to evolve neural networks for specific applications [26]. Instead of requiring human input to refine a single neural-network model, neuroevolution automatically performs the search process by allowing a population of many neural networks to evolve, where only those networks which improve in performance survive. In this way, man-

ually tuned hyperparameters of a neural network are transformed into learned parameters.

The application of neuroevolution as a method for automated machine learning has a few important consequences. Because the neural network model complexity search is done across a population of many networks, the speed to convergence for an optimal solution scales with the number of neural networks in the population. The more networks that are employed, the faster the space can be searched. This thereby increases the computational complexity significantly. If population sizes are in the tens to hundreds of thousands, the evaluation complexity is large enough to motivate the transition to modern multi- and many-core compute architectures. As will be described in chapter 4, one of the hallmarks of neuroevolution—its ability to evolve neural networks of diverse structure—has so far prevented the development of generalized many-core algorithms which scale well with the network population size. This is primarily because the diversity in the evolved neural network structure leads directly to divergent evaluation graphs for these networks. On the one hand, many-core architectures—which employ single-instruction-multiple-data (SIMD) processors—perform optimally when execution branching is minimal. On the other hand, evolving neural networks with differing topologies has the opposite effect, execution branching is enhanced.

Presented in chapter 4 is a novel many-core algorithm for the concurrent evaluation of entire populations of topologically-divergent neural networks. This work represents the first general-purpose mapping of large numbers of heterogeneous neural networks to many-core architectures. The achieved evaluation speed up is a step toward enabling neuroevolution to play a more competitive role in the automated machine-learning space. Given the abundant computational resources available in most scientific laboratories, this work has the potential to lower the barrier of entry for domain scientists interested in achieving meaningful results from machine learning with neural networks.

Chapter 2

The sensitivity of core-collapse supernovae to nuclear electron capture

The study of interactions mediated via the weak nuclear force is of importance to a large number of fields in physics. However, it is of particular importance to the field of astrophysics because of the longer timescale on which weak interactions operate as compared to the strong and electromagnetic interactions. This is evidenced by the impact that new insights into weak reaction physics have on astrophysical models [7]. Specifically, electron-capture reactions play a prominent role in high-density environments such as those found in the late stages of massive star evolution [27, 28], thermonuclear [29, 30] and core-collapse supernovae (CCSNe) [31, 32], neutron stars [33, 34], and compact object merger events [35]. Realistic simulations of these environments rely on accurate nuclear physics inputs including electron-capture rates.

Electron-capture rates depend sensitively on allowed Gamow-Teller (GT) transition-strength distributions in the β^+ direction. These transition strengths characterize nuclear excitations in which a single unit of spin and isospin are transferred ($\Delta S = \Delta T = 1$), with

no transfer of orbital angular momentum ($\Delta L = 0$).¹ While the main component of electron capture occurs on the ground state configuration of a nucleus, in high temperature stellar environments electron captures on thermally-populated excited states of the parent nucleus can also contribute significantly to the overall rate [36]. Unfortunately, it is difficult to obtain information about transitions from excited states in the laboratory. Compounding the problem is the fact that in order to accurately include electron capture in simulations, one must include electron captures on a wide range of nuclei. Hence, in general one must rely on theoretical models for a complete description of stellar electron-capture rates. On the other hand, measurements of Gamow-Teller strength distributions in a representative set of nuclei are important for the development and benchmarking of robust theories. At the same time, it is critical that theoretical and computational efforts provide guidance to experimenters on which measurements to perform.

Presently, configuration-interaction (shell-model) calculations are the primary method for producing reliable GT strength distributions near stability in the *sd*- and *pf*- shells ($8 < [N, Z] < 20$ and $20 < [N, Z] < 40$, respectively) for electron capture on both ground and excited states [37, 38]. Quasi-particle random-phase approximation (QRPA) calculations have also been utilized to estimate GT strengths for large sets of nuclei, but only where transitions from the ground state are considered [39, 40, 41, 42, 43]. Furthermore, comprehensive sets of electron-capture rates (as a function of density and temperature) for a large number of nuclei based on QRPA calculations have not been published.

Direct and indirect experiments, such as β -decay and charge-exchange (CE) measurements respectively, provide robust benchmarks for theoretical GT strengths and therefore

¹Transitions which follow these selection rules are referred to as “allowed” transitions, and those which do not—for example, transitions with $\Delta L > 0$ —are known as “forbidden” transitions which typically proceed at a much reduced rate as compared to allowed transitions.

are crucial to understanding astrophysical electron-capture rates. Unfortunately, electron-capture and β -decay experiments can only access states in a limited Q-value window. Furthermore, for neutron-rich nuclei β -decay only provides information in the β^- direction, which is of limited use for electron-capture studies. Intermediate energy ($\gtrsim 100$ MeV/u) CE reactions in the β^+ direction, however, connect the same initial and final states as electron capture, providing information about transitions up to high excitation energies, and are thus well suited to study the full Gamow-Teller strength distribution of interest. At these energies, CE measurements have been empirically established to be accurate at the $\sim 10\%$ level and are therefore able to provide rigorous tests of theoretical Gamow-Teller strengths and derived electron-capture rates [13].

Recently, the results from (n,p), ($d,^2\text{He}$), and ($t,^3\text{He}$) CE reactions on nuclei in the pf -shell were systematically compared [13, 44, 45] with shell-model calculations using the KB3G [46] and GXPF1a [47] effective interactions in the pf -model space, and with calculations based on the QRPA formalism of Möller and Randrup [40]. The authors compared shell-model and QRPA derived electron-capture rates against those derived from CE measurements. It was found that the QRPA calculations systematically overestimate the electron-capture rates ($\sim 100\text{-}3000\%$, depending on density and temperature), whereas the shell-model estimates produce rates similar to those measured experimentally ($\sim 1\text{-}50\%$) [13]. Unfortunately, shell-model calculations are computationally challenging for nuclei beyond the pf -shell, and therefore weak rates used in high-density astrophysical calculations most commonly rely on less accurate methods. In each of these cases, systematic and random error exist, and it is therefore important to understand the sensitivity of astrophysical simulations to uncertainties in these rates.

Sensitivity studies are useful tools for guiding theoretical and experimental efforts because

they highlight nuclei that should be given particular focus, and they indicate the accuracy with which the parameters of interest need to be known. They also illustrate how strongly the current parameter uncertainties affect the outcome of the astrophysical simulations. In this chapter, results from a recent sensitivity study are examined in which ~ 150 collapse simulations were performed with systematic and statistical variations of the electron-capture rates [2]. The impact these rate variations have on the collapse, bounce and pre-explosion phases of core-collapse supernovae simulations for a range of presupernova progenitors and equations of state (EOS) will be described.

As part of this work, a modular and open-source weak reaction rate library¹ was developed for use in astrophysical simulations. For the simulations described in this work it was implemented in the stellar core-collapse code `GR1D` [48], but has also since been used in the multi-dimensional CCSNe codes `FLASH` [49, 50], and `COCONUT` [51, 52].²

In the following sections, the inner core of the protonneutron star (PNS) and the observable peak neutrino-luminosity from core bounce are shown to depend sensitively on the electron-capture rates of neutron-rich nuclei (+16/-4% and $\pm 20\%$, respectively). As variations on this level are not easily reproduced from uncertainties in other inputs to the simulations, they motivate the development of new theoretical models for electron-capture rates as well as relevant measurements, which together will constrain these and other key parameters discussed in this work.

²<http://www.jinaweb.org/weakrates>

2.1 Astrophysical weak interaction rates

The weak nuclear force is important for a number of processes that influence the evolution of massive stars [7]. For example, interactions mediated by the weak force are important ingredients for nucleosynthesis and also for the internal structure of evolving stars, as they sensitively determine the electron-to-baryon ratio Y_e and the iron-core mass just prior to core-collapse [27]. Unlike the conditions present during quasi-static stellar evolution, however, in the core of a collapsing star the density and temperature are high enough that nuclear and electromagnetic reactions equilibrate [53]. This is not the case for weak reactions which operate much more slowly and thus continue to affect the nuclear composition, the neutrino emission, and ultimately the dynamics of the entire event.

As compared to other semi-leptonic weak interactions (weak interactions with nuclei), electron capture has a particularly remarkable impact on the core-collapse environment [54]. In the final stages of a star’s life, the nuclear-energy generation rate of the core that normally sustains a star against gravitational collapse is absent because the core is composed of highly stable iron-group nuclei. Instead, at these late times the electron-degeneracy pressure provides the primary stability against collapse. It is therefore apparent that electron captures that remove electrons from the system will have dramatic consequences for this environment. Furthermore, the electron chemical potential μ_e is sufficiently large to overcome Q-value³ restrictions, and so the electron-capture rates are significant.

Just prior to and during the early moments of collapse, other weak interactions can also play a role. Martínez-Pinedo *et al.* [55] have shown that β^- decay can temporarily compete

³The Q-value refers to the rest mass energy difference between the final and initial nucleus, $Q = M_f - M_i$, and describes either the energy required for the reaction to occur ($Q < 0$), or the energy deposited by the reaction ($Q > 0$). For stellar electron-capture on neutron rich nuclei, $Q < 0$.

with electron capture when $Y_e=0.42-0.46$, which can occur during Si shell burning and the early stages of collapse. However, as collapse ensues, μ_e quickly becomes large enough that β -decay electrons are energetically blocked due to degeneracy. Similarly, β^+ decay can also compete with electron capture for nuclei with $Q_{e^+} > 2m_e c^2$, but in the core-collapse environment neutron-rich conditions are favored, and Q_{e^+} is below this threshold.

The importance of reactions mediated by the weak nuclear force, and specifically electron capture, as it pertains to core-collapse was first demonstrated by Bethe *et al.* [56]. Not long after, the theory of stellar electron capture was formalized by Fuller, Fowler, and Newman (FFN) [57]. In their pioneering work they published the first tabulation of weak interaction rates (β^\pm -decay and e^\pm -capture) considering presupernova conditions where allowed Fermi and Gamow-Teller (GT) transitions dominate. Since then, advancements in computational resources have allowed for detailed nuclear shell-model calculations that have increased the accuracy of the weak-interaction theory first outlined by FFN. Major weak-interaction rate tabulations that derive from a combination of experimental data and shell-model effective interactions are the Oda *et al.* [37] and Langanke and Martínez-Pinedo [36] tabulations for *sd*- ($A=17-39$) and *pf*-shell ($A=45-65$) nuclei respectively. For heavier nuclei, where full shell-model calculations are computationally unfeasible, the Shell Model Monte Carlo (SMMC) approach has been employed which preserves nuclear properties in very large model spaces. Langanke *et al.* [38] have combined this method with an RPA technique to estimate electron-capture rates at densities and temperatures relevant during core-collapse for nuclei in the *pf**g*/*sd**g*-shell ($A=65-112$), which have come to be known as the LMSH rates. Juodagalvis *et al.* [58] have also produced a set of more than 2200 additional rates based on the same RPA technique but utilizing a Fermi–Dirac parameterization instead of the more computationally expensive SMMC calculations. The individual rates were not released, but instead these

rates were averaged over NSE abundances and reported along a characteristic core-collapse (ρ, T, Y_e) trajectory. However, such a prescription is not suitable for sensitivity studies in which the detailed response of simulations to individual nuclei is desired.

The rate tabulations listed in Table 2.1 have been implemented into the weak rate library used in this work. Together these tabulations contain 445 rates for 304 unique nuclei over a large density and temperature grid. This library has been built as a standalone module and has also been implemented into the neutrino-interaction library `NuLib` [59] for use in neutrino-transport routines employed by the spherically-symmetric, general-relativistic stellar collapse code `GR1D` [59]—see Section 2.3 for more information. Details on the density and temperature range for each of the included rate tabulations are shown in Table 2.1. The mass coverage of each rate table is shown in Figure 2.1.

Table 2.1: Density, temperature and mass ranges for the compiled weak rate set

Model space								
Table	s	p	sd	pf	pfg/sdg	T (GK)	$\text{Log}_{10}(\rho Y_e \text{ g cm}^{-3})$	Ref.
FFN	x		x	x		0.01 - 100	1.0 - 11	Fuller <i>et al.</i> [57]
ODA	x		x			0.01 - 30	1.0 - 11	Oda <i>et al.</i> [37]
LMP	x			x		0.01 - 100	1.0 - 11	Langanke <i>et al.</i> [38]
LMSH					x	8.12 - 39.1	9.22 - 12.4	Hix <i>et al.</i> [31], Langanke <i>et al.</i> [60]
Approx.	x	x	x	x	x	-	-	Langanke <i>et al.</i> [38]

The LMP+LMSH rates were first implemented into a spherically-symmetric core-collapse simulation by Hix *et al.* [31]. They compared simulations with this set of shell-model based electron-capture rates against simulations that utilized the Bruenn [61] prescription for electron capture. The evolution of the core-collapse phase and the structural differences in the core at bounce seen in that work were significant. In light of the differences that exist between theoretical estimates for electron-capture rates and those inferred from CE experiments, these results motivate the need for a detailed sensitivity study.

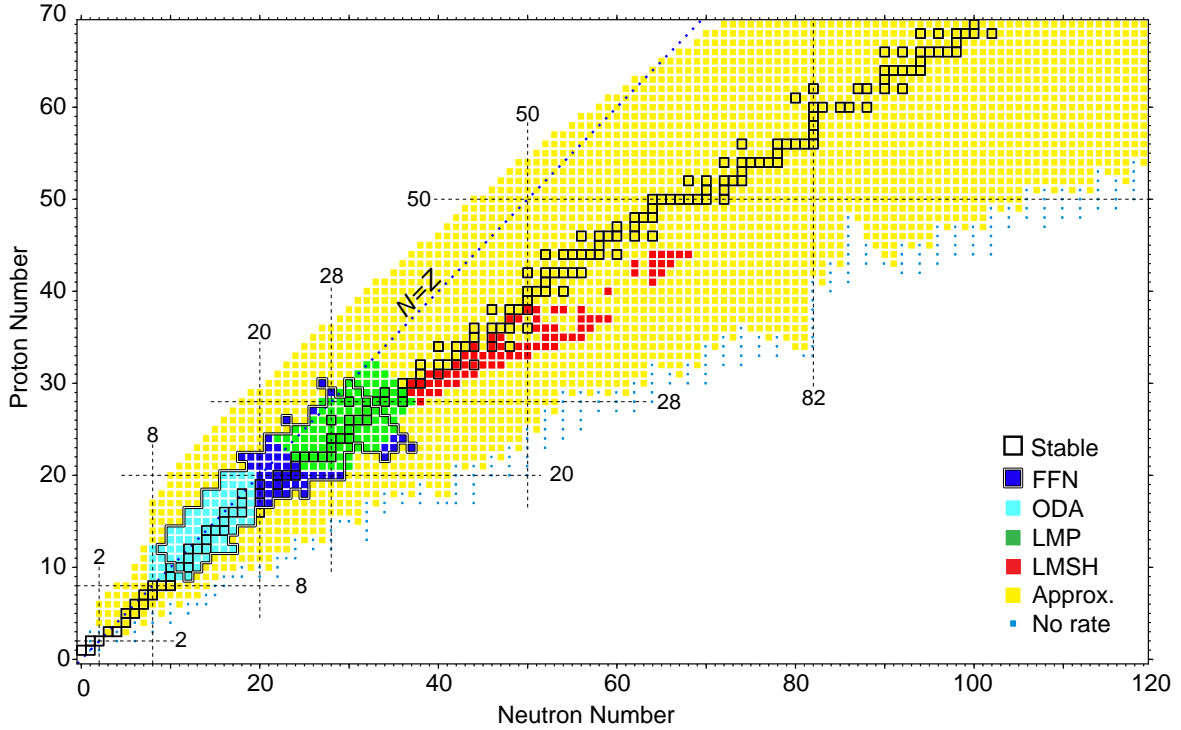


Figure 2.1: Chart of the nuclear species depicting the nuclei included in each rate tabulation as well as the full reach of the weak rate library presented in this work. The table to which a species belongs is given by the color and legend in the figure. The Oda set contains rates for lower mass *sd*-shell nuclei (light blue), the LMP set contains rates for the intermediate mass *pf*-shell nuclei (green), and the LMSH set contains rates for the heavier mass *pf**g*/*sd**g*-shell nuclei near stability (red). The FFN tabulation provides rates across the *sd* and *pf*-shells (dark blue). Squares individually bordered in black are stable nuclei. The tables are mutually exclusive except for FFN which spans many nuclear shells. To distinguish between nuclei with rates from FFN and another table, the border of the FFN set has been outlined with a black and white line.

To handle the large number of nuclei not included in the tables, Hix *et al.* [31] utilized an average electron-capture neutrino emissivity for all nuclei which lacked a shell-model based rate. In this work, instead of performing averaging, the approximate routine of Langanke *et al.* [38] is employed, which is based on the parameterization of the electron-capture rate as a function of the ground state to ground state Q-value. This approximation was first described by Fuller *et al.* [62] and was later parameterized and fit to shell-model calculations in the *pf*-shell by Langanke *et al.* [38]. In this approximation, the electron-capture rate is,

$$\lambda_{\text{EC}} = \frac{\ln 2 \cdot B}{K} \left(\frac{T}{m_e c^2} \right)^5 [F_4(\eta) - 2\chi F_3(\eta) + \chi^2 F_2(\eta)] \quad (2.1)$$

and the neutrino-energy loss rate is,

$$\lambda_{\nu_e} = \frac{\ln 2 \cdot B}{K} \left(\frac{T}{m_e c^2} \right)^6 [F_5(\eta) - 2\chi F_4(\eta) + \chi^2 F_3(\eta)], \quad (2.2)$$

where m_e is the electron mass, $K = 6146$ s, F_k are Fermi integrals of rank k and degeneracy η , $\chi = (Q - \Delta E)/T$, $\eta = \chi + \mu_e/T$, and T and μ_e are the temperature and electron chemical potential. B ($= 4.6$) and ΔE ($= 2.5$ MeV) are fit parameters taken from Langanke *et al.* [38] and respectively represent effective values for the transition strength and energy difference between final and initial excited states.

Figure 2.2 compares the rate estimates from this approximation and from the shell-model rate tabulations in Table 2.1. As is easily seen from the figure, the variance of the shell-model rates depends sensitively on the density of the environment. At lower densities, where the electron chemical-potential and electron capture Q-value are comparable ($\mu_e \approx Q_{\text{EC}}$), the location of excited states in the daughter nucleus, and the associated Gamow-Teller transition

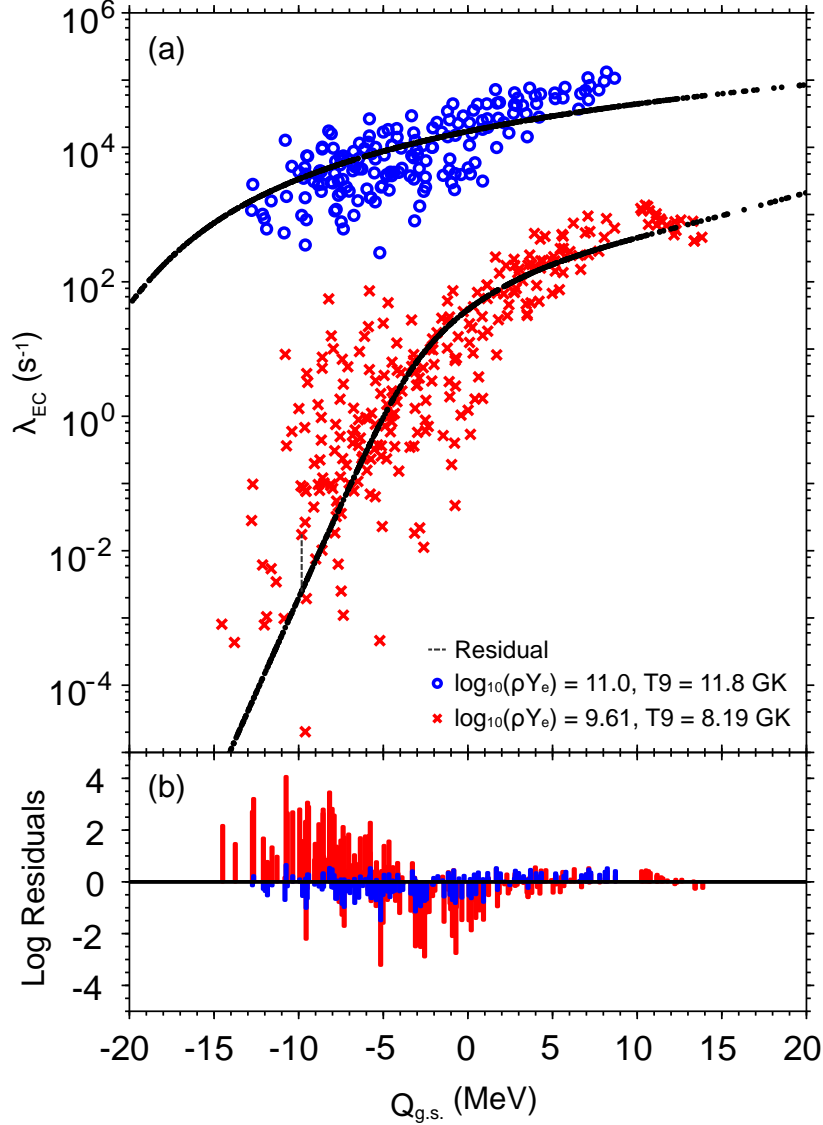


Figure 2.2: Panel (a): Q -value dependence of electron-capture rates at two points along a core-collapse trajectory. The scattered points are tabulated (shell-model and SMMC) rates for each electron-capture reaction, while the black points are the approximate rates given by Eq. 2.1. Panel (b): The residual differences between \log_{10} of the shell-model rates and the approximate rates for each nucleus in the weak-rate library. An example residual is indicated on panel (a). When the density and temperature of a simulation evolve outside the range of the rate tables (see Table 2.1), rates are calculated via the approximate routines in order to avoid an artificial cut off imposed by the table boundaries. Rates are estimated between density and temperature grid points via monotonic cubic-spline interpolation as described by Steffen [63].

strength, sensitively determine the total electron-capture rate for a nucleus. New final states in the daughter nucleus become accessible as the electron Fermi-energy, which scales with μ_e , increases beyond the energy required to populate them via allowed electron capture. The large scatter of the electron-capture rates at lower densities (Fig. 2.2) is because the Fermi energy is comparable to the excited state energies of the daughter nuclei and the internal structure of each nucleus varies significantly. During collapse, as the density increases and the material becomes more neutron rich due to successive electron captures, both the magnitude of the average electron capture Q-value and μ_e increase. However, μ_e increases more quickly with density than the reaction Q-values do, and eventually $\mu_e \gg Q_{\text{EC}}$ implying that the majority of the electron-capture channels are open. In this regime the rate is less sensitive to the excitation energy spectrum of the daughter nucleus, and instead depends more strongly on the total GT strength across all possible final states. The decrease in the variance of the shell-model electron-capture rates in the higher density case of Figure 2.2 is a result of this.

While the parameters of Eqs. 2.1 and 2.2 were originally fit from the LMP nuclei, there is reasonable agreement of the approximation with the other tabulated rates. Outside of these tables, significant deviations from the estimates of this approximation may exist, specifically for heavier neutron rich nuclei [64]. But for the purpose of a sensitivity study, this approximation—from which the majority of the rates are calculated—is used as a base estimate off which the electron-capture rates may be varied. Given this set of rates, it is shown in section 2.4.2 that the simulations are most sensitive to intermediate mass neutron-rich nuclei. However, electron-capture rates developed from sophisticated theoretical models do not exist for individual nuclei in this region, and thus cannot be benchmarked against experimental measurements. Therefore, the estimates provided by the approximation of Eqs. 2.1 and 2.2 may be systematically off by a considerable amount. As will be shown, changes in the

predicted rates for these nuclei have significant consequences for the simulations, motivating the need for experimental and theoretical efforts to constrain the rates of these species.

2.2 Core collapse and the role of electron capture

Just prior to collapse, the temperature of the stellar core becomes high enough ($T \gtrsim 0.5 \text{ MeV}$) that the photon gas has sufficient energy to photodissociate nuclei into alpha particles and free nucleons. However, the density is also high ($\rho \gtrsim 10^9 \text{ g cm}^{-3}$) resulting in large nuclear reaction rates that rapidly form nuclei from these light particles. The balance reached between these competing processes is known as Nuclear Statistical Equilibrium (NSE). If the entropy is sufficiently low and the mass fraction of free nucleons is small compared to that of nuclei, the most abundant nucleus in NSE is the species with the highest binding energy for a given electron-fraction, $Y_e (= Z/A)$ [55]. A broad distribution of abundant nuclei forms due to finite temperatures which distribute the abundances around these peak nuclei.

As collapse ensues and the central density increases through the first few decades, electron captures are the primary engine of deleptonization. Electrons are removed from the system and the produced electron-neutrinos (ν_e) are able to freely stream out of the core, decreasing both Y_e and total lepton fraction Y_l . As Y_e decreases, peak abundances move toward neutron-rich nuclei, and the core begins to cool as ν_e 's carry away energy and entropy. Electron captures continue to dominate the neutrino transport during collapse until the last few milliseconds before core bounce. In these final moments, the central density reaches a few times $10^{12} \text{ g cm}^{-3}$, which is large enough that the neutrino mean free path begins to shorten due to coherent scattering on nucleons and heavy nuclei. This increase in the ν_e -scattering cross section results in a neutrino diffusion time that exceeds the collapse time, thereby

trapping the electron neutrinos in the inward flow of matter. After this occurs, the conversion of electrons into electron-neutrinos via electron captures no longer removes leptons from the core. Instead, further electron captures increase the electron-neutrino fraction Y_{ν_e} in order to conserve the now constant lepton fraction and bring the system of electrons and electron neutrinos into equilibrium.

Prior to the work of Langanke *et al.* [60] it was believed that electron captures on free protons were of greater importance than captures on nuclei during collapse. The main considerations involved were that electron capture on free protons has a higher rate owing to a smaller in magnitude Q-value. Additionally, nuclei with neutron number $N \geq 40$ have full pf -shell single particle states and so the addition of another neutron via an allowed electron-capture transition would be Fermi-blocked. Langanke *et al.* [60] recognized that the many-body nuclear states have mixed configurations and do not follow a simple Hartree-Fock filling of single particle orbitals. They also suggested that thermal excitation of nucleons to the $g_{9/2}$ orbital creates vacancies in the pf -shell, and together with configuration mixing, electron capture on bound protons is unblocked. Furthermore, because of the low entropy in the core, and the neutron-rich conditions, the abundance of heavy nuclei is several orders of magnitude higher than that of free protons, resulting in a higher overall electron-capture rate. Thus, because electron captures on nuclei dominate, it is of great value to future experimental and theoretical efforts to investigate the contribution each species has, and to identify which nuclei are most important, as these efforts would provide direct constraints to CCSNe simulations.

2.3 Codes & Methods

2.3.1 NuLib

In addition to electron-capture rates, other rates are needed to perform core-collapse simulations. The collection of rates used is contained in NuLib [59], an open-source, neutrino-interaction library.¹ NuLib contains routines for calculating electron-type neutrino/antineutrino charged-current absorption opacities on nucleons with corrections for weak magnetism and nucleon recoil based on the formalism of Burrows *et al.* [65] and Horowitz [66]. Neutrino emissivities for these processes are determined via Kirchhoff's law which equates the absorption rate of a equilibrium neutrino distribution to the emission rate of the underlying matter. Elastic scattering of neutrinos on nucleons, and coherent scattering of neutrons on alpha particles and heavy nuclei is also included in NuLib. For the former, corrections for weak magnetism and nucleon recoil are included, and for the latter, corrections from ion-ion correlations [67], electron polarization, and the nuclear form factor are employed. Inelastic scattering of neutrinos on electrons is included based on the expressions of Bruenn [61]. Emissivities of heavy-lepton neutrino/antineutrino pairs via electron-positron annihilation and nucleon-nucleon Bremsstrahlung are computed ignoring final state neutrino blocking. For neutrino-antineutrino annihilation, instead of computing the non-linear absorption opacity during the simulation, an effective absorption opacity is used which has been shown to be an excellent approximation for core-collapse supernovae [59].⁴

⁴<http://www.NuLib.org>

2.3.2 GR1D

The electron-capture rate implementation described in the previous sections is used to study the sensitivities of the core-collapse phase to these rates using the code `GR1D` [48, 59]. `GR1D` is an open-source spherically-symmetric general-relativistic neutrino-transport and hydrodynamics code used for studying stellar collapse and the early stages of a core-collapse supernova. For details of the hydrodynamics module of `GR1D` see reference [48]. The neutrino transport is handled through a general-relativistic, energy-dependent two-moment formalism for which extensive details can be found in O’Connor [59]. The employed scheme numerically solves for the time evolution of the first two moments of the neutrino distribution function: the neutrino energy density and the neutrino momentum density. The simulations utilize 18 energy groups logarithmically spaced between 0 and 250 MeV. Only electron type neutrinos are evolved until the central density reaches $10^{12} \text{ g cm}^{-3}$, after which electron anti-neutrinos and a characteristic heavy lepton neutrino are included. However, these latter two neutrinos do not become important until core bounce has occurred. Spatial fluxes of the neutrino moments are treated explicitly. Inelastic neutrino-electron scattering is handled explicitly until the central density reaches $10^{12} \text{ g cm}^{-3}$ at which point an implicit treatment is used.

Simulations in spherical symmetry (one dimension) such as those facilitated by `GR1D`, afford the computational resources needed for the inclusion of a highly detailed and complete set of microphysics. The same is not true for multidimensional simulations, as the computational requirements are more extensive, forcing the inclusion of only a small subset of the physical interactions. Fortunately, the core-collapse and early post-bounce phases of core-collapse supernovae are well represented in one dimension due to the lack of turbulent convection in the core. Thus, together `NuLib` and `GR1D` are able to provide a robust and

extendable code base for CCSNe simulations with state of the art microphysics.

2.3.3 Neutrino emission via electron capture

Electron capture is associated with the emission of electron neutrinos and so the electron-capture rate is proportional to the integrated spectrum of ν_e emitted per second. The rate for a particular nuclide, as tabulated in the implemented rate tables, is defined as the sum of the rates for each of the individual nuclear transitions

$$\lambda = \sum_{ij} \lambda_{ij}, \quad (2.3)$$

where indices i and j correspond to levels in the parent and daughter nucleus respectively. The spectra of emitted neutrinos from the electrons capturing on nuclei, described by the matter temperature T and electron chemical potential μ_e , will vary based on the initial and final states involved owing to a different reaction Q-value,

$$Q_{ij}^{\text{EC}} = Q_{g.s.} + E_i - E_j \quad (2.4)$$

where $Q_{g.s.}$ is the atomic mass difference of the initial and final nuclei, and E_i and E_j are the excitation energies of the populated states in the parent and daughter nucleus respectively. The most comprehensive solution to constructing neutrino spectra would be to coherently sum the spectra of neutrinos emitted from each nuclear transition. However this would rely upon rate tabulations for individual transitions which are not presently available. Thus, an effective neutrino spectra is implemented in terms of a single reaction Q-value, q , that is chosen to constrain the average energy of the spectrum to match that from the tabulated

rates [68],

$$n(E_\nu, q) = E_\nu^2 (E_\nu - q)^2 \frac{N}{1 + \exp\{(E_\nu - q - \mu_e)/kT\}} \quad (2.5)$$

$$\langle E_\nu \rangle = \frac{\int_0^\infty E_\nu n(E_\nu, q) dE_\nu}{\int_0^\infty n(E_\nu, q) dE_\nu} = \frac{\lambda_\nu}{\lambda_{\text{EC}} + \lambda_{\beta^+}}, \quad (2.6)$$

where $n(E_\nu, q)$ is the neutrino distribution function and is normalized to the total electron-capture rate for a particular nuclear species. λ_ν , λ_{β^+} , and λ_{EC} are the neutrino energy loss, positron emission, and electron-capture rates respectively. Eq. 2.6 is solved numerically for the effective Q-value, $q = q_{\text{eff}}$, which then defines the effective neutrino spectrum for the electron-capture reaction of interest at a given ρ , T , and Y_e . The approximate neutrino spectra generated in this way are unable to reproduce complex structure such as double peaking in the true neutrino distribution, which may occur when there is a resonant allowed transition ($Q_{ij}^{\text{EC}} \sim 0$) between an excited parent state and the daughter-nucleus ground state. However, it approximates singly-peaked neutrino distributions quite well [68]. The spectrum is normalized to the total electron-capture rate via Gaussian-Legendre quadrature with an adaptive algorithm, developed in this work, that adjusts the range of integration to the full width of the spectrum.

Utilizing these spectra, the electron-capture neutrino emissivity for a given nuclear species is calculated as

$$\eta_i(E_k) = \frac{1}{4\pi} E_k n_i n(E_k, q_{\text{eff}}), \quad (2.7)$$

where the ν_e 's are assumed to be emitted isotropically, n_i is the number density for the i -th nucleus, $n(E_k, q_{\text{eff}})$ is the neutrino spectra evaluated at the effective Q-value that solves Eq. 2.6, and E_k indicates the energy of energy group k . Evaluation of the emissivity is done point wise at the centroid of each energy bin, and has units $\text{erg}/(\text{cm}^3 \cdot \text{sr} \cdot \text{s} \cdot \text{MeV})$.

For estimates of the NSE number densities used above, several EOS from Hempel and Schaffner-Bielich [69] were used. In particular, the SFHo EOS and internally consistent NSE distribution developed by Steiner *et al.* [70] was the primary EOS employed. Results were also compared against the DD2 [71] and TMA [72] EOS, each with self-consistent, but different, NSEs. The SFHo and DD2 EOS were chosen because they currently best satisfy both nuclear and astrophysical constraints [73]. Instead of meson self-interactions, the DD2 EOS implements density-dependent meson-nucleon couplings which have been used successfully to describe nuclear structure in a wide region of the nuclear chart and have also been tested in heavy-ion collisions [71]. For nuclear masses, the SFHo and DD2 NSE distributions rely on the Finite Range Drop Model (FRDM) from [74] and [75], whereas the TMA EOS utilizes a mass table calculated by Geng *et al.* [76]. Both mass tables incorporate experimentally determined masses from Audi *et al.* [77] and only resort to theoretical estimates where no experimental measurements are available. For consistency, in addition to NSE abundances, these mass distributions are also utilized in the calculation of reaction Q-values for use in Eq. 2.1.

2.4 Sensitivity study

2.4.1 Reference simulations

In order to establish reference simulations off which variations are performed, the widely studied 15 solar mass, solar metallicity progenitor star s15WW95 [78] was used, as well as s12, s20, and s40 from WH07 [79], which span the range of stellar compactness $\xi_{2.5}$ [80] in this model set. The core compactness, ξ_M , is the ratio of the mass enclosed M to its enclosing radius, and for this model set, s12 (s40) has the least (most) compact core. This variety in compactness is an important factor for assessing the global sensitivity of core-collapse supernovae to detailed microphysics, as progenitors with similar compactness will likely have similar sensitivities to microphysical variations. More details on the progenitor model set utilized in this work can be found in the progenitor sensitivity subsection 2.4.3.1. For each simulation the SFHo EOS is utilized, and in addition, for simulations with the s15WW95 progenitor star the DD2 and TMA EOS, and NSE distributions, are employed.

A full complement of neutrino-interaction microphysics is incorporated via NuLib in each reference simulation, which includes the newly implemented weak rates library described here. The weak-rate tables were included using the following priority hierarchy: $LMP > LMSH > Oda > Approx.$, ensuring that rates from sources with higher priority are utilized where rate estimates from multiple sources exist. *Approx.* indicates the parameterized rate approximation of Eqs. 2.1 and 2.2, which is used for nuclei not included in the tables and for regions of density and temperature which are beyond the limits found in Table 2.1. For consistency, only tables that derive from shell-model calculations are utilized.

For each progenitor and EOS collapse simulations are performed in GR1D and follow the evolution until at least ~ 100 ms after bounce. The collapse proceeds as described in Section

2.2. Differences in the collapse evolution for different progenitors stem from the hydrostatic conditions in the cores of these massive stars at the onset of collapse. For stars with large $\xi_{2.5}$, larger central⁵ temperatures are needed to balance gravity. This gives lower central densities, and therefore less electron capture during the final stages of stellar evolution. The range of initial central Y_e goes from ~ 0.422 for the s15WW95 model to ~ 0.447 for the s40WH07 model, or a range of $\sim 6\%$. After neutrino trapping sets in, a range of trapped lepton-fraction of $\sim 0.288 - 0.297$ is observed, where s40WH07 and s12WH07 have the minimum and maximum trapped Y_l , respectively. The overall higher deleptonization rate for the more compact progenitors is due to both longer collapse times and larger matter temperatures, which enhance the electron-capture rates.

Simulations utilizing different EOS, while holding all else constant, demonstrate only small variations in the density, temperature, and Y_e central-zone trajectories up to bounce. Figure 2.3 details the abundance distributions for each EOS, as well as the resulting average electron capture rate along a collapse trajectory. The NSE distributions of all three EOS are largely similar early on, but differences in the mass table of the TMA EOS cause it to diverge from the others starting around $1 - 2 \times 10^{12} \text{g cm}^{-3}$. However, differences are seen in the electron-capture rate only after central densities of $2 \times 10^{12} \text{g cm}^{-3}$, where any effect on the evolution is suppressed because of neutrino trapping. Near nuclear saturation density, however, the differences in EOS begin to play a more important role. The density-dependent couplings of the DD2 EOS, for instance, result in higher central temperatures at bounce. However, since the average rate in simulations utilizing each of the EOS are nearly identical, they result in a difference of trapped lepton-fraction of only a fraction of a percent. For more information on the sensitivity of the electron and lepton fractions to the EOS during

⁵*Central* used in this context refers to the inner most zone of the core-collapse simulation.

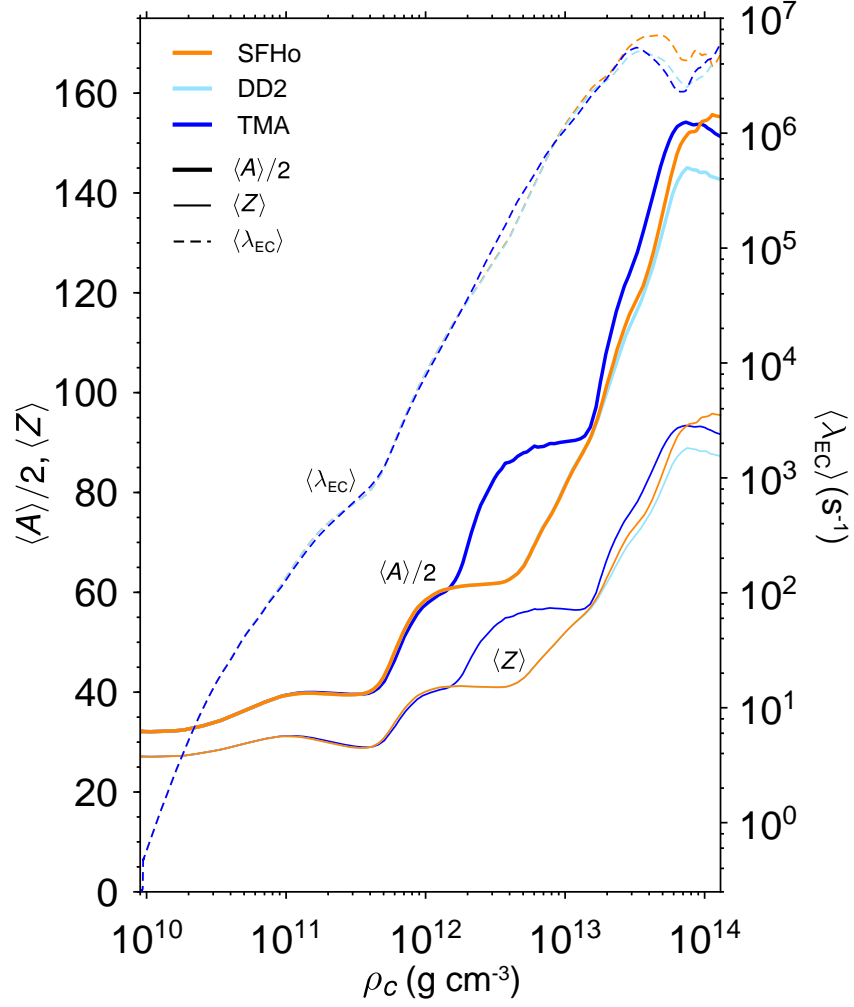


Figure 2.3: The average nuclear mass (divided by two), charge, and electron-capture rate versus central density for the three EOS utilized in this study. The colors indicate different EOS, while the line style indicate which quantity is plotted. All three EOS have nearly identical abundance distributions up to densities of $2 \cdot 10^{12} \text{ g cm}^{-3}$. Beyond this point the TMA EOS has a heavier and slightly more neutron rich mass distribution compared to both SFHo and DD2, but maintains a comparable average electron capture rate overall. These simulations each utilize the s15WW95 progenitor.

collapse see Fischer *et al.* [73].

Together, these reference calculations span a wide range of progenitor and EOS dependences that ensure a configuration-independent assessment of the core-collapse sensitivity to electron capture on nuclei, and furthermore demonstrate the universality of collapse. In what follows, results are discussed for variations on the s15WW95+SFHo reference simulation but any significant differences in relation to variations on the other progenitor+EOS reference simulations are pointed out.

2.4.2 Species dependent sensitivity

To understand the sensitivity of core-collapse to different regions of electron capturing nuclei, the central zone collapse profile from the reference simulation is used to decompose the change of the electron fraction with time, \dot{Y}_e , into the electron captures of each nuclear species. While using only the central zone is an approximation, it is justified by noting the observation by Liebendorfer [81] that the electron fraction profiles typically correlate quite well with density during the collapse phase. Therefore, matter will generally have the same electron capture history. The rate of change of the electron fraction with time, \dot{Y}_e , that is estimated accounts for ν_e re-absorption in an energy-dependent way,

$$\dot{Y}_e^i = \frac{4\pi\alpha}{\rho N_a} \sum_k \frac{\Delta\epsilon_k \cdot \eta_i(\epsilon_k)}{\epsilon_k} \cdot \left(1 - \frac{E_k}{B_k}\right) \quad (2.8)$$

where \dot{Y}_e^i is the time derivative of the electron fraction due to electron captures on the i th nuclear species, α accounts for the general relativistic time dilation, N_a is Avogadro's constant, ρ is the density, ϵ_k is the energy of the k th energy bin, $\Delta\epsilon_k$ is the k th energy bin width, η_i is the emissivity of species i and $1 - \frac{E_k}{B_k}$ is the neutrino blocking factor that

accounts for re-absorption as collapse approaches weak equilibrium. Along with a hydrodynamical correction due to advection of electrons into the central zone, the time integral of Eq. 2.8 added for all nuclei reproduces the full time dependent Y_e profile of the central zone during collapse, indicating that electron captures on heavy nuclei singularly drive the deleptonization of the central zone.

With this method, the deleptonization history due to each nucleus can be individually investigated. At these densities and temperatures, NSE diversifies the abundant nuclei, ensuring that no single nucleus dominates the deleptonization. There are, however, subsets of nuclei that contribute more than others to the reduction of Y_e . A nuclear-mass dependence can be studied by binning the contribution to $|\dot{Y}_e|$ from each nuclide into nuclear mass bins and tracking the evolution of each region up to neutrino trapping. Figure 2.4 plots the deleptonization rate in the core for different nuclear mass bins, as the central Y_e progresses from its progenitor value to its value when weak equilibrium is achieved, just prior to bounce. Early on, before the collapse becomes strongly dynamical, nuclei in both the mass range $25 < A < 65$ (*sd+pf*-shell) and those in the $65 < A < 105$ (*pf**g*/*sd**g*-shell) comprise the main component of the deleptonization. However, during the strongest push toward neutron-rich conditions, where Y_e rapidly changes from ~ 0.41 to ~ 0.28 , nuclei with mass $A > 65$ dominate the evolution as seen by the red and light blue curves in Figure 2.4. Unfortunately, the most precise electron-capture rate estimates fall below this region and instead, the rates are set primarily by the approximation of Eq. 2.1.

It is also useful to understand the specific nuclei that have the largest integrated contribution to core deleptonization up to neutrino trapping. Shown in Figure 2.5 are the 500 nuclei with the largest integrated $|\dot{Y}_e|$ from $t = 0$ to the trapping time—when densities are in excess of $2 \cdot 10^{12}$ g cm⁻³. This reveals the channel through which the bulk of electron captures

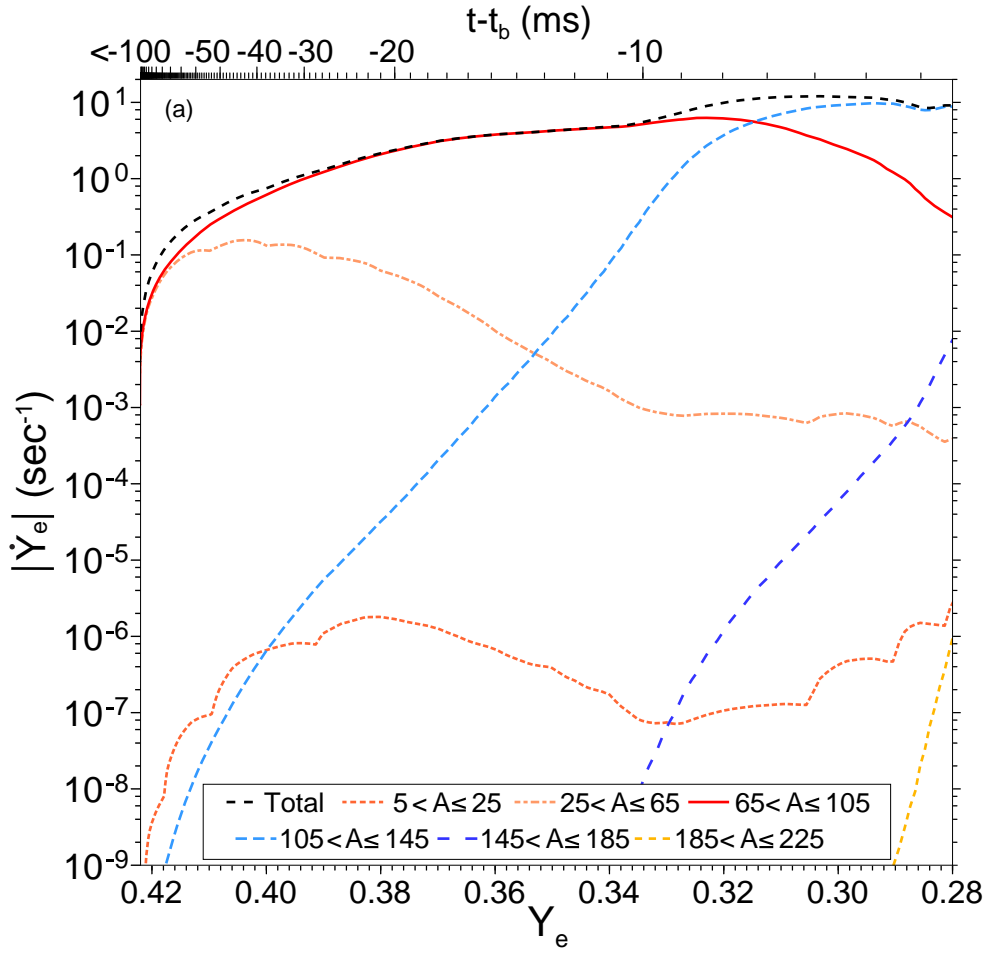


Figure 2.4: The contribution of nuclear electron capture to the change of the matter electron fraction with time. The contours are the binned sums of $|\dot{Y}_e|$ for each species in several mass regions. For reference, the central density at $t - t_b = -20, -10, -5, -2,$ and -1 ms is $1.41 \cdot 10^{11}, 4.06 \cdot 10^{11}, 1.42 \cdot 10^{12}, 8.49 \cdot 10^{12}, 3.30 \cdot 10^{13}$ g cm $^{-3}$ respectively.

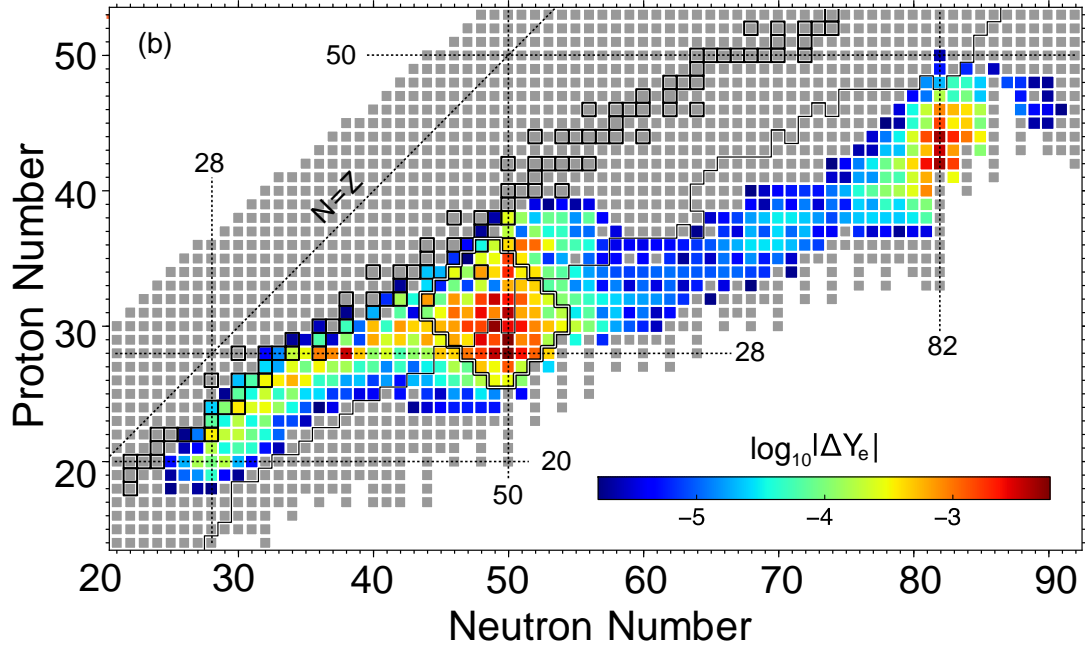


Figure 2.5: Top 500 electron capturing nuclei with the largest absolute change to the electron fraction up to neutrino trapping. The color scale indicates $|\dot{Y}_e|$ integrated up to the trapping time, occurring when $\rho_c \sim 2 \cdot 10^{12} \text{ g cm}^{-3}$, such that the total electron-fraction at this point is equal to its initial value less the sum of ΔY_e , the plotted quantity, over all nuclides. Calculations are based on the s15WW95+SFHo reference simulation. The black contour that runs parallel to the valley of stability on the neutron-rich side is the boundary between measured [77] and theoretical masses used in the approximate rate estimates of Eqs. 2.1 and 2.2. The rectangular outline indicates the size of the sampling region used in the statistical resampling study, and also the set of nuclei which exhibited the largest changes to the simulations when excluded from the electron-capture calculations.

operate. The central electron-fraction at the trapping density is reproduced by subtracting the sum of this quantity over all nuclear species from the initial electron-fraction,

$$Y_e(t = t_{\text{trapping}}) \simeq Y_e(t = 0) - \sum_i \Delta Y_e^i, \quad (2.9)$$

where ΔY_e^i is shown in Figure 2.5, and the component of Y_e due to advection of electrons into the central zone (otherwise making this relation exact) is left out for simplicity. Within the *pf*g and *sd*g-shells the primary contributors to the deleptonization phase of collapse are neutron rich nuclei near the N=50 and N=82 closed neutron shells (see the dashed vertical lines in the figure).

To confirm these results, they are gauged against the sensitivity of the collapse phase to localized groups of nuclei by employing a statistical resampling technique where sets of nuclei are removed from the simulation. This method is based on well known statistical resampling methods such as bootstrap and jackknife resampling [82]. Specifically, a rectangular region centered on a nucleus and spanning all nuclei within ± 3 isobars and ± 5 isobaric chains is removed from the calculation of the electron-capture neutrino emissivity. An example of such a removed region is drawn on Figure 2.5. This technique is employed in 48 simulations with resampling performed uniformly across the nuclear chart.⁶ Using this technique the simulations are found to be most sensitive to nuclei in the mass range 74-84 with $Z/A (= Y_e)$ between 0.36-0.44, corresponding to nuclei near ^{78}Ni , ^{79}Cu , and ^{79}Zn . These results agree with the \dot{Y}_e calculations performed above, and indicate that species near the N=50 magic number have the largest contribution in magnitude to the change in the electron fraction overall. The impact of removing these species from the simulation corresponded to a change

⁶The resampling regions were allowed to overlap, but were chosen such that uniform coverage across the nuclear chart was achieved in the resampling study.

of inner-core mass at bounce of $\gtrsim 10\%$, whereas resampling in other regions resulted in variations of only a few percent.

The electron-capture rates for these nuclides rely entirely on the approximation of Eqs. 2.1 and 2.2, which were fit originally to rates of lower-mass mid-shell nuclei near stability. Therefore, in the region indicated by the above two studies, the approximation is largely uncertain and may be systematically off by a significant amount. For instance, these estimates do not account for nuclear structure effects that may occur near the $N=50$ closed neutron shell. Depending on the nuclear configurations, thermal excitations, and increasing dependence on forbidden transitions, Pauli blocking⁷ may considerably reduce the electron-capture rates in this area. Given that the change of inner-core mass at bounce was largest when the rates of these nuclides were decreased to zero as compared to any other set, and that without any evaluative measurements the uncertainties in these rates remain large, experimental and theoretical work should focus here. Any substantial changes to the electron-capture rate estimates for these nuclei will likely have a relatively large impact on simulation predictions for the PNS formation, and will therefore help to constrain important collapse and pre-explosion phase quantities.

2.4.3 Systematic variations

To study the strongest impact of variations in the electron-capture rates, simulations in which the rate for each $A>4$ nuclide is systematically scaled by factors of 10, 4, 2, 0.5, 0.25, and 0.1. In this way, the structure of the rates as seen in Figure 2.2 is preserved (the

⁷Pauli blocking arises as a result of the Pauli exclusion principle in which identical fermions are unable to occupy the same quantum mechanical state. In the case of neutron-rich nuclei, $N=50$ represents a $g_{9/2}$ orbital fully occupied by neutrons. Unless the electron capturing nuclei are highly excited such that there are holes in this or other lower energy orbitals, allowed Gamow-Teller transitions cannot occur.

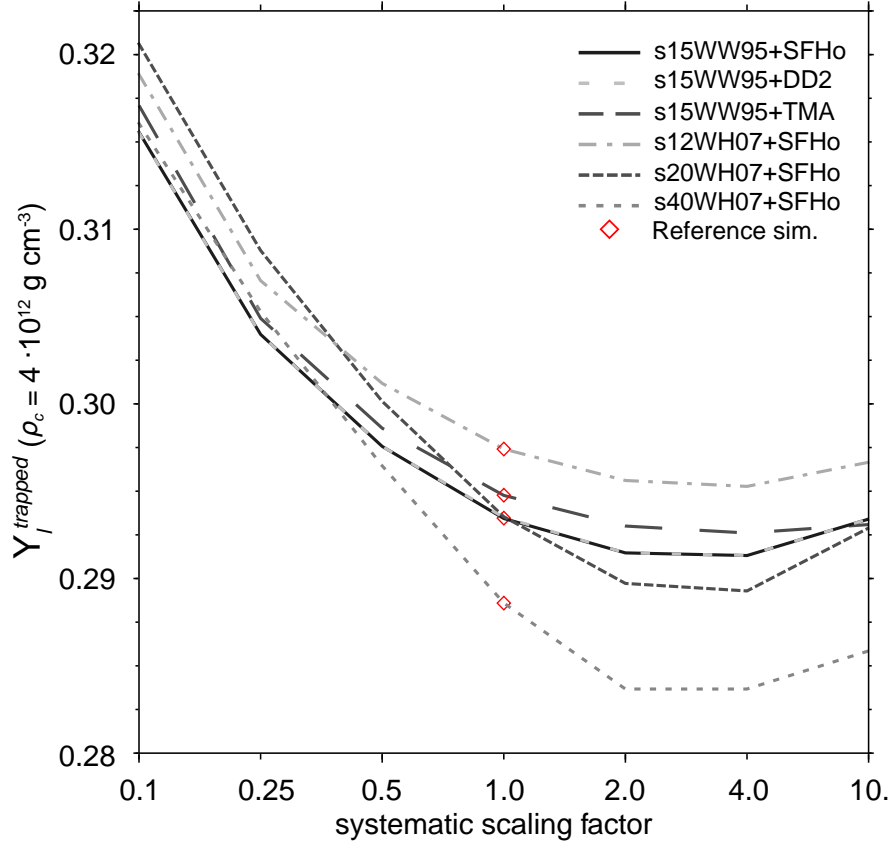


Figure 2.6: Projection of the (trapped) lepton fraction at $\rho_c = 4 \cdot 10^{12} \text{ g cm}^{-3}$ as a function of the electron-capture rate scaling factor for progenitor+EOS reference simulation. In all the cases the lepton fraction begins to increase if the capture rate becomes too high because of a dramatic increase in the electron neutrino absorption cross section. The asymmetry seen here indicates that those quantities which depend on $Y_{l/e}$ are likely to be more sensitive to a reduction of the electron-capture rates due to a systematic overestimate in the base rates, than they are to an increase due to an underestimate.

lower panel of residuals is unaffected), but the distribution of rates is shifted to larger or smaller values depending on the scaling factor. Systematic shifts of the rates emphasize the role of electron capture as a regulator for entropy and temperature in the simulations. By increasing the rates, more neutrinos are emitted and escape during the initial stages of collapse, thereby increasing the evaporative neutrino-cooling. Furthermore, because the dominant source of matter pressure is electron degeneracy, increased electron-capture rates accelerate the collapse. This impacts the matter profiles outside the shock in the early post-bounce phase. Decreasing the rates has the opposite effect, the entropy, temperature, and electron fraction of the core are significantly higher because less cooling takes place.

The evolution prior to and right at $\rho_c = 2 \cdot 10^{12} \text{ g cm}^{-3}$ (which is the density that defines neutrino trapping) is what sets the final value of the trapped lepton and electron fractions, which are important due to their direct impact on the formation of the PNS. For all the reference simulations, a minimum in the trapped lepton fraction was found to occur with a systematic scaling factor of approximately four. The minimum that forms can be seen in Figure 2.6. Scaling by ten slightly reverses the downward trend, and increases the trapped lepton-fraction from its minimum value. This behavior is the result of electron-neutrino capture on heavy nuclei becoming the primary source of opacity, exceeding what is typical as a result of coherent ν_e -scattering. When the rates have been enhanced by a factor of ten, the ratio of the absorption and scattering opacities, κ_a/κ_s , surpasses unity already by central densities of $3 \cdot 10^{11} \text{ g cm}^{-3}$ and $\kappa_a \sim 4\kappa_s$ by the time $\rho_c = 10^{12} \text{ g cm}^{-3}$. Absorption cross sections are then large enough to trigger an early onset of neutrino trapping at densities lower than what is found for the reference rates. The consequence is that electron capture has a smaller window of deleptonization, leading ultimately to a higher Y_l overall.

The range of electron fractions near core bounce is commensurate with the range of

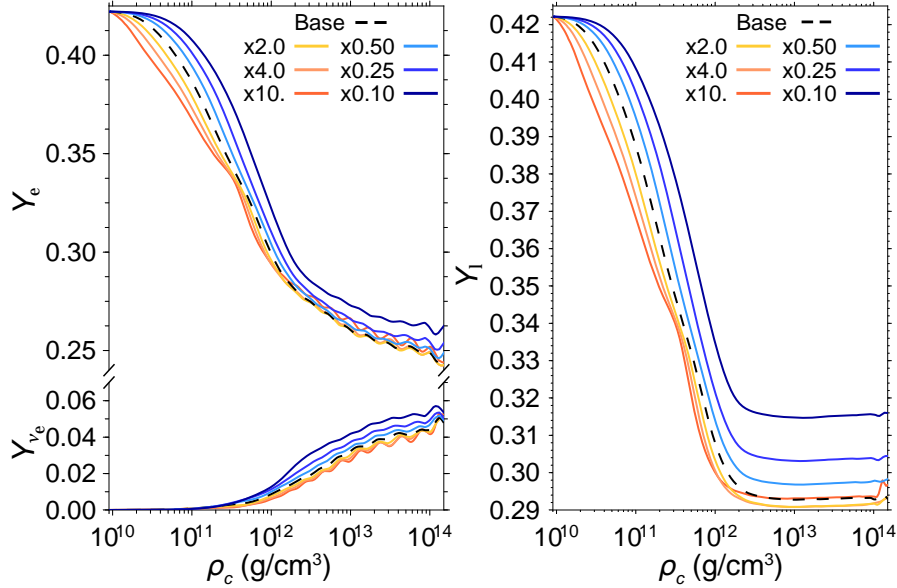


Figure 2.7: Comparison of the central electron, electron-neutrino (left) and lepton (right) fractions in which the nuclear electron-capture rate for every species has been scaled by factors shown in the legend. Warmer colors indicate a higher overall electron capture rate, and cooler colors indicate a lower rate. The dashed black line indicates the reference s15WW95+SFHo simulation.

trapped lepton-fractions so far described, see Figure 2.7. As mentioned above, variations of Y_e (and Y_l) on this level are of importance due to its direct impact on the formation of the PNS and the supernova shock. Electron fraction, entropy, density and velocity profiles are shown in Figure 2.8 for s15WW95+SFHo at -1, 0, 1, and 5 milliseconds relative to bounce. Of particular interest, the mass of the forming PNS inner-core at bounce, seen as the mass behind the steep velocity gradient in panel (b), was found to vary on the order of $\sim 0.1 M_\odot$, and up to $\sim 0.2 M_\odot$ five milliseconds after bounce. The asymmetry observed in the trapped-lepton fraction, where scaling the rates by 0.1 had a more dramatic effect than scaling by 10, translates directly to the variation of the inner-core mass at bounce (+16/-4% from the reference). The result is that the forming PNS has a lower bound on the inner-core mass at bounce over the range of electron-capture rates explored. Because the rates are already high, and therefore the absorption opacity is already almost comparable to the scattering opacity,

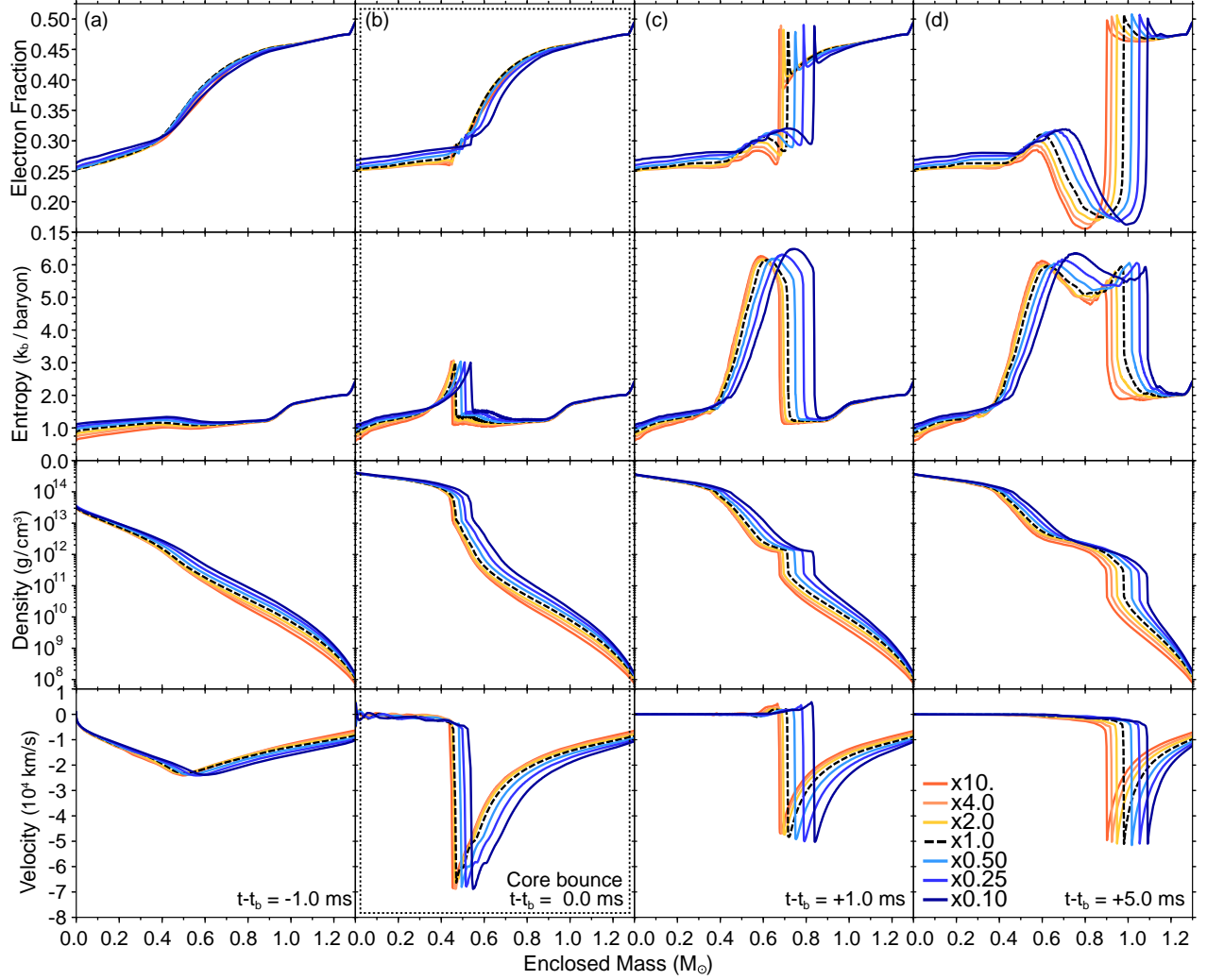


Figure 2.8: The electron fraction, entropy, density, and velocity as a function of enclosed mass at four times during a core-collapse simulation, spanning 6 ms around bounce, including the collapse phase just after the onset of neutrino trapping (a), core bounce (b), and 1 ms (c) and 5 ms (d) after bounce during which the shock has begun its outward trajectory. The reference simulation (s15WW95+SFHo) is shown in dashed black. Simulations shown in color have electron-capture rates scaled systematically for all species by factors of 10, 4, 2, 0.5, 0.25, and 0.1. Core bounce ($t - t_b = 0$) shown in panel (b) is defined as when the entropy at the shock front exceeds $3.0 k_b/\text{baryon}$.

the range of inner-core mass at bounce comes mainly from simulations with decreased rates relative to the base simulation.

Such variations in the homologous inner-core mass will translate directly to the kinetic energy of the emergent shock that eventually detonates the star. Furthermore, the one to two orders of magnitude range of density outside the shock (see Fig. 2.8) will likely play an important role during the shock propagation and explosion phases of multidimensional CCSNe simulations. Therefore, further investigations into the impact of these variations in the late stages of two and three dimensional CCSNe simulations are warranted.

In addition to the direct impact on core dynamics and structure, the neutrino emission at bounce is found to be very sensitive to these variations. Figure 2.9 shows the neutrino luminosity 500 km from the center for the different neutrino species as a function of time. Prior to bounce the ν_e -luminosity begins to rise from electron captures on bound protons in nuclei, but is quickly regulated by neutrino trapping, causing a down turn in the luminosity. During this time the core is very sensitive to the nuclear electron-capture rates as the entropy is low enough that heavy nuclei dominate the available mass. Scaling the rates for each nucleus using the same systematic factors results in a 40% variation of the ν_e -luminosity before bounce. During bounce, the electron-neutrino burst—seen as the peak luminosity in the left panel of Figure 2.9—is powered primarily by electron capture on free protons. The core-bounce and shock liberates nucleons from their bound states and the entropy rises causing a significant increase in the nucleon and light particle abundances. That said, while the electron-capture rate on free protons, λ_p^{EC} , is not adjusted in these simulations, a range of $\pm 20\%$ relative to the reference peak ν_e -luminosity is observed.

These dramatic variations of the peak electron neutrino luminosity are a result of alterations to the neutrinosphere and shock convergence-timescale. Specifically, when electron

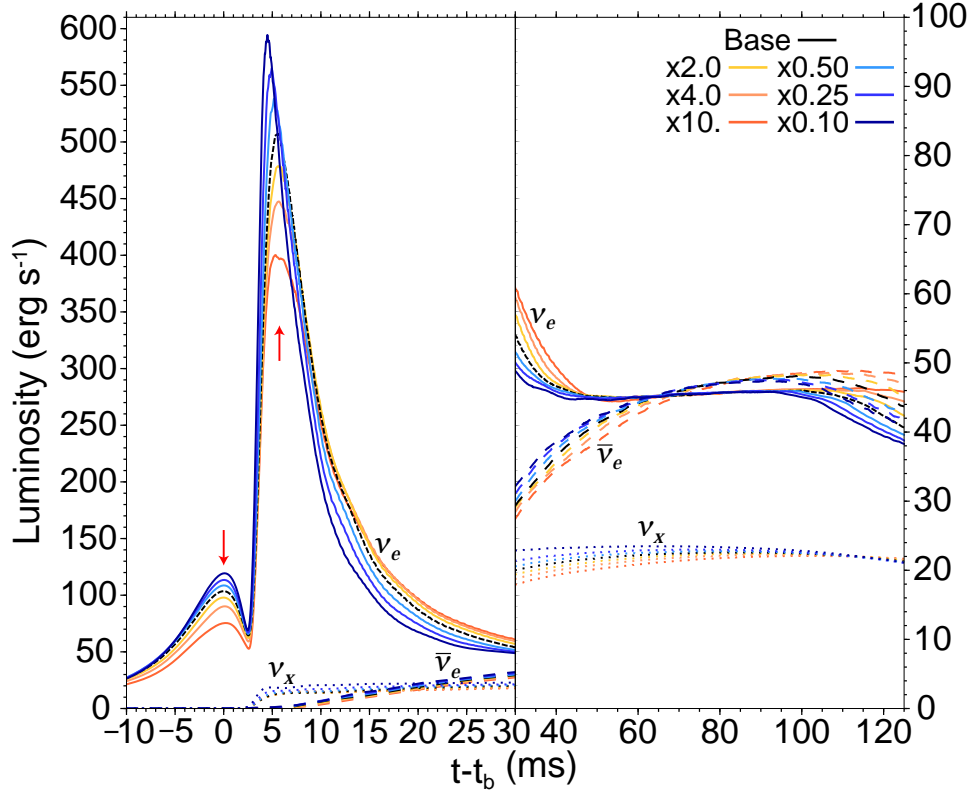


Figure 2.9: The neutrino luminosity as measured at a radius of 500 km as a function of time after bounce in the s15WW95+SFHo simulation set. Electron-capture rate scaling factors are shown in the legend, where contours with warmer colors have higher rates, and cooler colors have lower rates. While the peak electron-neutrino luminosity is considered particularly stable across core-collapse simulations, it varies significantly with variations of the electron-capture rates on medium-heavy nuclei. When the rates are at their lowest ($\times 0.1$ case), the shock reaches the neutrinosphere more quickly than in the other simulations. This results in a larger luminosity in the peak electron-neutrino burst because more ν_e s are able stream out of the core at early times. The opposite is true when the rates are higher, the neutrinosphere and shock converge much more slowly, and so the neutrinos spend more time diffusing out of the inner core, reducing the peak luminosity but distributing it out to later times.

captures on nuclei are weaker (scaling by 0.1), the inner-core mass that forms at bounce is significantly larger. This results in more kinetic energy transferred to the shock, allowing it to sweep up mass more quickly. In Figure 2.8 this can be seen by the broadening of the distribution of shock locations in mass between the different simulations in the velocity plot 5 ms after bounce (bottom-right) as compared to $t - t_b = 0$. Also, with a weaker overall rate the opacity will be lower, allowing the neutrinosphere to move in to lower radii more quickly. The combination of these effects result in the shock and neutrinosphere radii converging earlier for the simulations with lower electron-capture rates, and later for simulations with higher rates, up to a difference on the order of 3.5 ms. Thus, electron capture on protons liberated by the shock produce neutrinos that are able to reach the neutrinosphere earlier and freely stream away, contributing to a larger ν_e peak luminosity when the nuclear electron capture rate is systematically lower. On the other hand, when the nuclear electron capture rate is high, the emitted neutrinos diffuse more slowly through the core, and reach the neutrinosphere at later times, thus strongly quenching the peak luminosity but spreading out the emission to later times. Due to the high luminosity of the electron-neutrino burst near the time of bounce, it is a candidate for detection from a galactic core-collapse supernovae in Earth-based detectors sensitive to electron neutrinos, e.g. those with a detector volume composed of liquid Argon. And while such measurements are not presently of high enough precision to resolve each variation seen here, they may indicate the total amount of electron capture occurring at core bounce.

2.4.3.1 Progenitor model sensitivity

In order to evaluate the significance of the electron-capture systematic sensitivity studies, they were tested against a study of the progenitor dependence of the core-collapse phase.

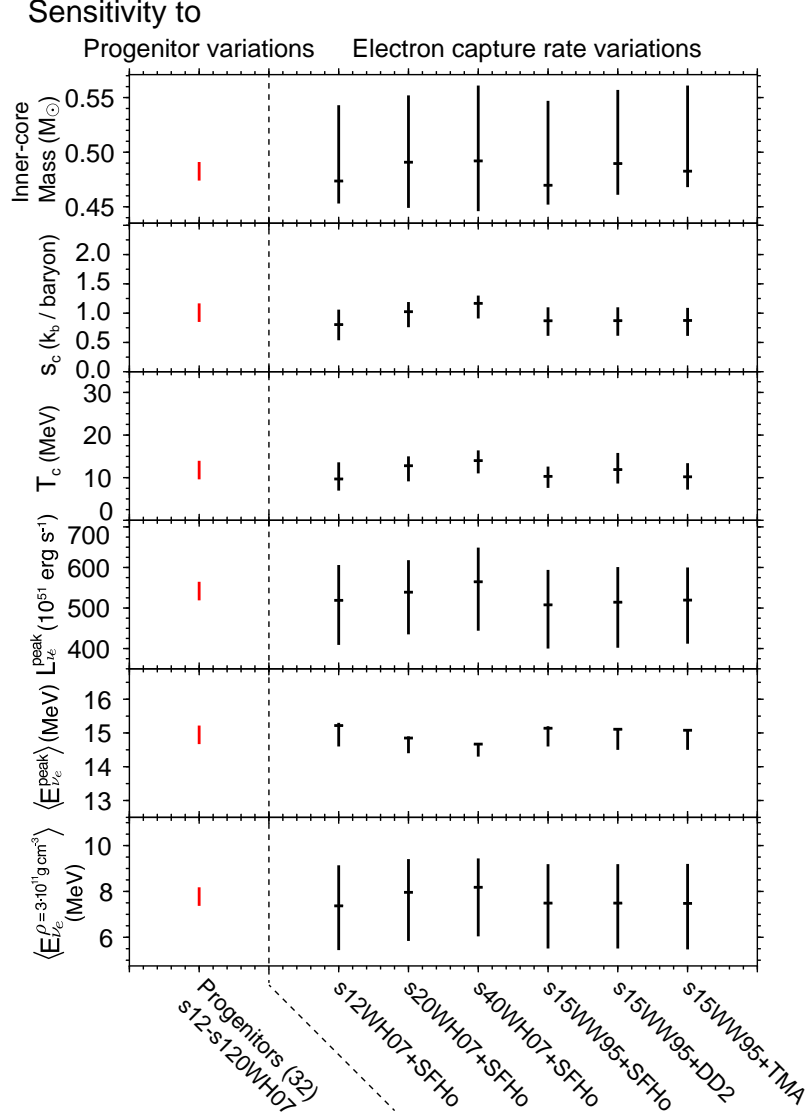


Figure 2.10: The full range of sensitivity of the PNS inner-core mass, central entropy, and central temperature at bounce as well as the peak ν_e -luminosity, the peak average ν_e energy, and the average ν_e energy prior to neutrino trapping, owing to variations of the progenitor model and electron-capture rates. Thirty two progenitors were utilized from the WH07 model set of Woosley and Heger [79] for producing the progenitor bars (red) in the figure. Each bar of the electron-capture rate variations derives from simulations where the rates have been systematically scaled by factors of 10, 4, 2, 0.5, 0.25, and 0.1. The horizontal tick represents the value of the reference simulation for the tested Progenitor + EOS combination. The window ranges are chosen so that the progenitor sensitivity bars are of equal size across each of the plotted parameters.

Drawing from the larger set of progenitors from which the reference progenitors of the electron-capture study belong, the 2007 non-rotating solar-metallicity single-star model set from the stellar evolution code KEPLER [79] was utilized. This model set contains the pre-supernova configuration of 32 stars ranging in zero-age-main-sequence (ZAMS) mass from $12 M_{\odot}$ to $120 M_{\odot}$ —s12WH07 and s120WH07 respectively. Simulations of these progenitors exhibit a $\sim 3.5\%$ range of trapped lepton-fraction (0.288 - 0.298), a $\sim 4\%$ range of inner-core mass at bounce ($0.473 - 0.491 M_{\odot}$), and a $\sim 9\%$ range of electron-neutrino peak luminosity ($5.19 - 5.65 \cdot 10^{53} \text{ erg s}^{-1}$) during the neutrino flash occurring just after core bounce.

Figure 2.10 compares the stellar progenitor model and electron-capture rate dependence of several structural and neutrino quantities during collapse. The range of inner-core mass and peak ν_e luminosity seen from employing the WH07 progenitor model set are each approximately a factor of 5 smaller than the ranges seen from varying the electron-capture rates across all progenitor+EOS references. On the other hand, the range of central entropies and temperatures at bounce are comparable between the two sensitivity studies. The ν_e average energies just prior to neutrino trapping and during the deleptonization burst are also compared in Fig. 2.10. The neutrinos emitted during the luminous burst just following core bounce are of higher energy than those emitted earlier because they arise primarily from electron capture on free protons. They also decouple from the core at a much hotter and denser neutrinosphere than prior to bounce, yielding higher energy neutrinos. In both of the sensitivity studies, variations of the electron-capture rates and of the initial stellar models, the range of average neutrino energy during peak emission is comparable ($\approx \pm 0.5 \text{ MeV}$).

While captures on free protons contribute only marginally to deleptonization in the central zone, further out in the iron core, where the densities are lower (and Y_e 's are higher), electron captures on protons contribute to the deleptonization, especially in cases where

electron captures on nuclei are suppressed. The capture of electrons on these free protons produces neutrinos of a higher average energy, commensurate with the large spread seen in the bottom panel of Fig. 2.10 (which is taken when the central density is $3 \times 10^{11} \text{ g cm}^{-3}$, but present from the onset of collapse). Another contribution to the energy spread is the systematic shift of electron captures to more neutron rich nuclei as the electron-capture rates are increased and the matter becomes more neutron rich. These neutron-rich nuclei have more negative Q-values, yielding lower energy neutrino emission. Both of these effects result in a dispersion of average neutrino energies early on that is several factors larger than what is seen in the progenitor simulations.

Finally, note that while the peak luminosity is only weakly dependent on the progenitor model, the post-bounce pre-explosion luminosity of all six neutrino species have strong progenitor dependences [83]. On the other hand, the pre-explosion luminosities investigated here are much less sensitive to the nuclear electron-capture rates comparatively—see panel (b) of Figure 2.9. The diverging of the luminosities seen at $t - t_b = 120 \text{ ms}$ is due only to the difference in collapse times between the simulations which carries over to the evolution of the mass accretion rate after bounce.

2.4.4 Monte-Carlo variations

In addition to the possibility of systematic errors in the electron-capture rates, the effect of statistically distributed variations are also explored. Such an investigation is of great importance if the effect of an approximation such as Eq. 2.1 is to be understood. The main flaw in a continuous function for rate estimation across many nuclear species is the loss of structure, which would otherwise serve to statistically distribute the rates on a reaction by reaction basis (see Fig 2.2). To study this effect, Monte-Carlo (MC) variations of the

electron-capture rates were performed. Using an analytic description of the electron-capture rate distributions, such as a Gaussian or Poisson distribution, is likely to be inaccurate. Instead, the approximate rate is adjusted via MC for each species by adding to its $\log_{10}(\lambda_{\text{EC}})$ a value randomly chosen from a distribution created from the residuals of the tabulated rates and the approximate rates, i.e.

$$\log_{10}(\lambda_{\text{EC}}^{i,\text{table}}) - \log_{10}(\lambda_{\text{EC}}^{i,\text{Eq.1}}) \quad (2.10)$$

where i is an index running over all the tabulated reactions.

In constructing this distribution, it is important also to preserve the Q-value dependence of the residuals that can be seen in Figure 2.2b. This is done by separating the residual distribution into subsets so that the reaction-rate residuals in each subset have similar Q-values. To do so a Q-value binning of 2.5 MeV was chosen, but this method was also tested with binnings of 5.0 MeV and 10.0 MeV which resolve the Q-dependence less, but have more counts per bin from which to sample. From these samples, pseudo electron-capture rates were MC generated such that they retain the Q-value dependence of Eq. 2.1, but statistically distribute the approximate rate according to the variance of the rates calculated in the shell-model. Seven simulations for each binning were performed.

As mentioned before, at low densities the electron-capture rate depends strongly on the energy levels of the initial and final nuclides because the electron chemical potential is comparable to the excitation energies of the allowed Gamow-Teller transitions. As the electron chemical potential increases, it encompasses a larger range of excitation energies which results in the electron-capture rate becoming sensitive primarily to the total strength. In the low-density case of Figure 2.2a the approximation of Eq. 2.1 while appearing to

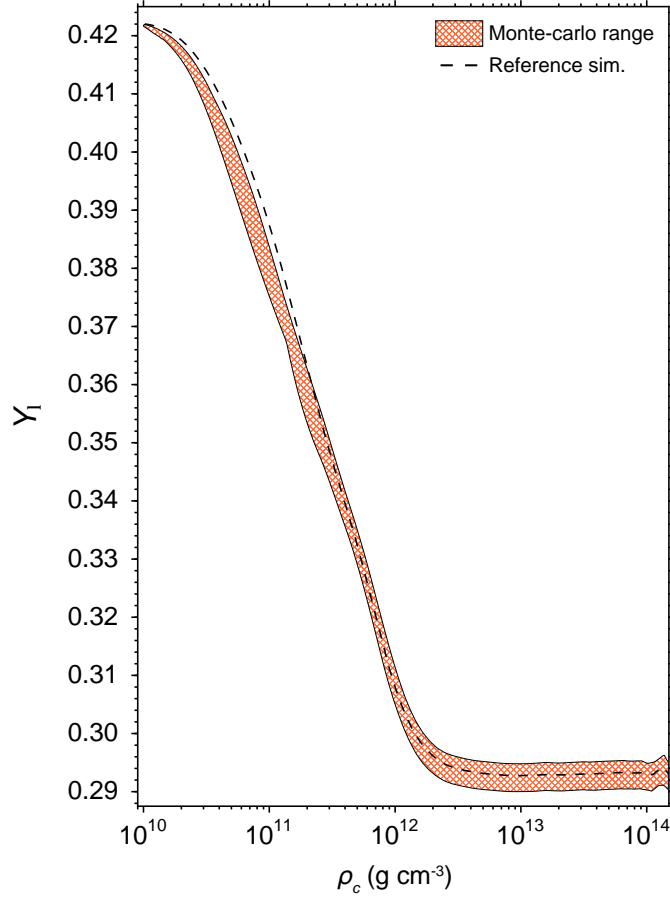


Figure 2.11: Lepton fraction band as a function of central density for the Monte Carlo (MC) described in the text. The band represents data points from seven MC simulations based on the s15WW95+SFHo reference, where the band width represents the min to max range of Y_l . The rates are varied by drawing from the Q-value dependent residual function shown in Figure 2.2 after binning it into 2.5 MeV energy bins. This binning was chosen as it best tracks the Q-value dependence of the residual distribution.

decently reproduce the mean of the shell-model rates, actually has a mean approximately a factor of two lower than the tabulated rates. As the density increases, this difference between the mean electron-capture rate estimated by the approximation and the shell-model rates decrease. Thus, the approximation better reproduces the mean rate in the high density case of Figure 2.2a. Because the MC simulations are based on residual distributions of the tabulated rates and the approximation, the average rate produced in each MC trial also has this bias.

Plotted in Figure 2.11 is the min-to-max band representing the range of lepton fraction observed from all of the MC simulations. The band drawn corresponds to a 2.5 MeV binning of the residual distributions from which the MC sampling was performed. For the reasons just described, the band has lower electron and lepton fractions than the reference at low densities, but becomes more statistically distributed around the reference at higher densities, near $5 \cdot 10^{11} \text{g cm}^{-3}$. The lepton fraction band width varies from about a half percent initially, to its largest value of $\sim 2.5\%$ just before neutrino trapping, and then decreases back to $\sim 1.5\%$ before bounce. Altogether, no significant impact on the core dynamics or the neutrino transport were observed and therefore it can be conclude that any statistically distributed scatter in the estimations of the electron-capture rates, such as those seen in Figure 2.2, will likely not impact the models.

2.5 Conclusion

Nuclear electron capture has long been understood to play an important role in the dynamics of core-collapse supernovae and large efforts have been undertaken to produce reliable estimates of electron-capture rates for astrophysical contexts. Although significant progress has

been made in benchmarking theoretical electron-capture rates by comparison with charge-exchange experiments (especially using shell-model calculations) [13], large uncertainties remain for neutron-rich nuclei and nuclei beyond $A=65$. Furthermore, sophisticated shell-model estimates for electron-capture rates exist only for a small subset of the large number of nuclei that contribute strongly. The implications of uncertainties in the electron-capture rate estimates for the core-collapse and early post-bounce phases of fully self consistent, general relativistic, core-collapse supernova simulations with comprehensive neutrino transport are explored in this work.

2.5.1 Most important nuclei

For the reference simulation, the contribution of each nucleus to core deleptonization is calculated, and a statistical resampling study is also performed. Both of these studies identify the nuclear species whose rate should be known most precisely due to their significance in the simulations. With the given set of electron capture rates—from shell-model estimates to the approximate estimates of Eqs. 2.1 and 2.2—the simulations are found to be most sensitive to neutron rich nuclei in the upper pf and pfg/sdg -shells.

Specifically, in these simulations nuclei near the $A\sim 80$, $N\sim 50$ closed neutron shell contribute the bulk of core deleptonization, and when removed from the simulations result in noticeable changes to the protoneutron star formation, with a significantly larger impact than when any other group of nuclei are removed. However, because sophisticated estimates from nuclear theory are not available for individual nuclei in this region, the electron-capture rates for these species have been accounted for in the past via simple averaging techniques and in this work via an approximation that has been fit to the LMP rate set. While this approximation reasonably reproduces the average electron capture rate for sd and pf shell

nuclei near stability, rates for heavier neutron-rich nuclides will likely diverge from what is predicted by this parameterization.

2.5.2 Impact of uncertainties

The impact such uncertainties may have are evaluated by varying the electron-capture rates for more than 6000 nuclei statistically, about the approximate prediction, and also systematically. On one hand, it is found that statistical variations of electron-capture rates effect the overall dynamics and neutrino emission only weakly, producing marginal changes to the simulations. These findings indicate that the lack of structural variation that distributes the rate estimates from one species to the next is not crucial to the simulations.

On the other hand, the average electron capture rate across a region of nuclei strongly determines the overall impact of those constituent nuclei. By systematically varying the electron-capture rates by factors between 10 and 0.1, dramatic variations in the inner-core mass (+16/-4 %) and the electron-neutrino luminosity ($\pm 20\%$) at and near bounce, respectively, are observed. Comparing with 32 simulations utilizing different progenitor models, this range of inner-core mass and peak neutrino-luminosity is found to be 5 times as large as that seen when varying the progenitor models.

In addition, the nuclear electron-capture rates are found to be already large enough in the reference simulations that increasing them beyond their base values has a considerably smaller effect than decreasing them. This has compelling implications. Rates for $A \sim 80$ nuclei near the $N=50$ shell gap, which have been shown to be the primary contributors to the overall impact of electron captures during core collapse, may be overestimated by Eq. 2.1 due to Pauli blocking at the closed neutron shell. Combined with a greater overall sensitivity to the systematic decrease in electron-capture rates, changes to the collapse and

early post-bounce phases of the simulations may be as significant as those seen in this study if the current rates of these nuclei are found to be overestimated.

2.5.3 Goals for future studies

For these reasons, it is important that experimental and theoretical efforts be aimed at nuclei which span the region on the chart of isotopes between stability and the neutron drip line in both the pf and $pf\bar{g}/sd\bar{g}$ model spaces, and further expand on the work that has been carried out for (near-)stable nuclei in the pf -shell. Since data from (n,p)-type charge-exchange experiments for nuclei in the $pf\bar{g}/sd\bar{g}$ -shell and for neutron-rich nuclei in the pf and $pf\bar{g}/sd\bar{g}$ -shell are scarce, new experiments are required to obtain a sufficient set of data to benchmark current and future theoretical estimates. To this end, presently feasible experiments on neutron-rich nuclei at and near stability with $60 < A < 120$ should add to the few cases that have been measured in this region. With the higher beam intensities that will be available at next generation rare isotope facilities, future experimental programs should focus on the neutron-rich component of the primary electron-capture channel shown in Figure 2.5. In particular, investigation of nuclei in the $A \sim 80$ and $N \sim 50$ region should take precedence, as changes to their electron-capture rates will significantly constrain the core-collapse dependence on nuclear electron-capture.

2.6 Updates

The weak-interaction rate library which was developed in this work in order to characterize the sensitivity of CCSNe to nuclear electron capture, has seen a number of updates and continues to be an active research component of the Joint Institute for Nuclear Astrophysics

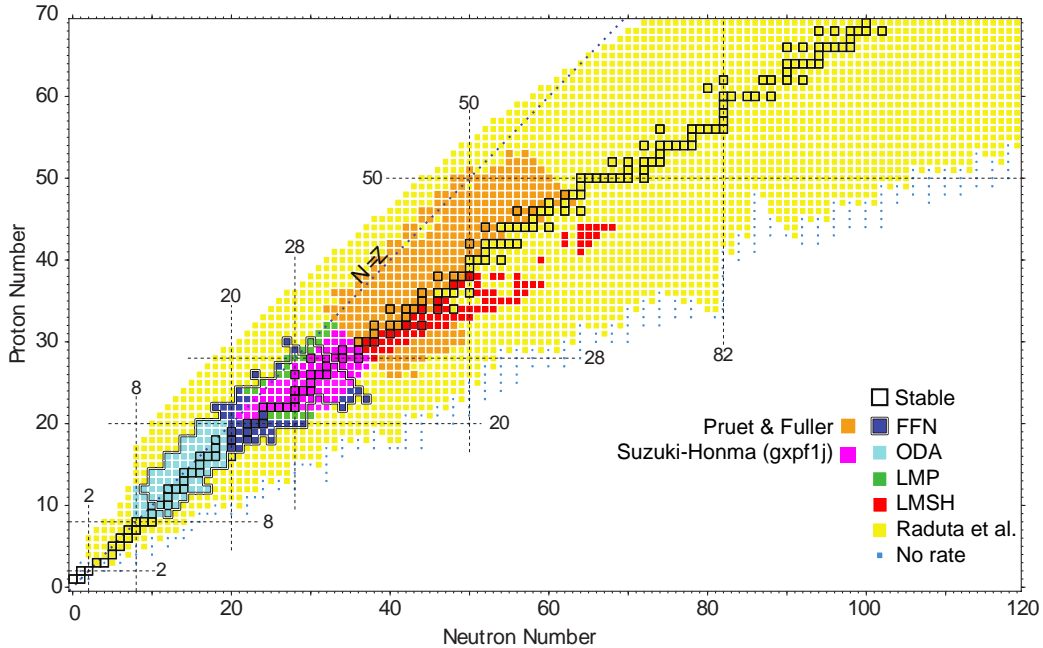


Figure 2.12: Updated version of Figure 2.1 showing the addition of the recently added rate tabulations since the libraries first implementation in [2].

– Center for the Evolution of the Elements (JINA-CEE). Recently released rate tabulations for nuclei in the *sd*- and *pf*-shells have been added to the weak rate library. The *sd*-shell tabulation includes rates calculated on nuclei with $A=17-28$ using the USDB configuration-interaction including coloumb effects [84]. The *pf*-shell tabulation was developed using the GXPF1J configuration-interaction by Honma *et al.* [85] for nuclei with masses between $A=42-65$. In addition, rates for a large number of proton-rich nuclei from the older empirically derived single-particle model calculations of Pruet and Fuller [86] have also been added to the weak rate library. The addition of these new tables can be seen in the updated library mass coverage of Figure 2.12. In addition to these rate tables, the approximate electron-capture rate parameterization described by Eq. 2.1—which is used for the majority of the electron-capture rate estimates in the sensitivity study—has been updated. Raduta *et al.* [87] extended this simple analytic parameterization to allow for temperature, electron density, isospin, and

nuclear odd-even dependencies. They found that the extra degrees of freedom introduced by the inclusion of isospin and odd-even effects considerably improved the agreement with electron-capture rate calculations from large-scale microscopic rate calculations [87]. While these advancements may improve the estimates of electron capture rates near the pf -shell, shell effects such as Pauli blocking—which as mentioned previously, can significantly suppress the rate—are not accounted for in the updated model. These methods have been incorporated and are currently maintained in the official version of the weak rate library.

In addition to the above theoretical updates that have been incorporated, a few subsequent computational and experimental investigations involving electron capture in core-collapse supernovae have been completed.

A follow up sensitivity study investigating the importance of the $N=50$ nuclei, described in section 2.4.2, was recently undertaken by Titus *et al.* [88]. In that work it was demonstrated that even though thousands of electron-capturing nuclei are included, variations in key characteristics of the evolution, such as the lepton fraction, electron fraction, entropy, stellar density, and in-fall velocity are about 50% due to uncertainties in the electron-capture rates on nuclei in the region above ^{78}Ni near $N=50$. Because of the significance of early results of this study, two of the first charge-exchange measurements in this region were performed: the $^{86}\text{Kr}(t, ^3\text{He})$ and $^{88}\text{Sr}(t, ^3\text{He})$ measurements. As ^{86}Kr and ^{88}Sr are the two most proton deficient, stable, $N=50$ nuclei, the results of these measurements will give a good indication of the allowed Gamow-Teller strength in nuclei with a full $g_{9/2}$ neutron shell and will help to constrain the electron capture rates in this region.

Concurrent with the above efforts, Richers *et al.* [3] investigated the impact various equations of state have on gravitational waves generated from axisymmetric rotating core-collapse simulations. As part of that work, various systematic variations of the electron

capture rates (comparable to what was performed in this work) were also utilized. It was found that the gravitational waves from post-bounce core oscillation had near equivalent dependence on the nuclear equations of state and the electron capture rates on heavy nuclei. Moreover, both influenced the expected gravitational wave signals that can be detected in current-generation gravitational wave detectors. If the electron capture rates were to be better constrained, detection of such gravitational waves may be able to untangle information about the nature of the nuclear matter equation of state.

As both the early post-bounce neutrino emission and gravitational-wave multi-messenger signals will be significantly constrained should improved experimental and theoretical estimates for the relevant electron capture rates become available, continued effort along this axis should be a top priority in the field of nuclear astrophysics.

2.6.1 Implementation procedure for future updates

The weak-rate library codebase is maintained on the web based `Git` version control repository hosting service `GitHub`. It is currently implemented as a `Git` submodule in the neutrino-interaction library `NuLib`. This organization allows for updates to the weak rate library to be easily propagated to `NuLib` without source code duplication. When future updates to the weak rate library are desired, the following steps should be followed,

1. The most up-to-date `GitHub` repository for the weak rate library (currently <https://github.com/csullivan/weakrates>) should be forked to a different user account.
2. Development and updates can be made using `Git` on this new `GitHub` fork of the weak rate library.
3. To propagate these changes to `NuLib`, a fork should be made of the most up-to-date

repository of NuLib (currently <https://github.com/evanoconnor/NuLib>).

4. This new GitHub fork of NuLib should then be updated so that its weak rate library submodule is pointing to the remote commit of the new weak rate library fork created above in step 2.
5. Finally, a GitHub *pull request* should be made to bring this change, of the weak rate library submodule link, into the main NuLib repository. This way NuLib users can simply update the NuLib submodules and receive the new weak rate library code.

After following these steps, the officially hosted version of the weak rate library will become the newly created fork, and NuLib will depend on it, rather than the csullivan/weakrates fork.

Chapter 3

The (${}^6\text{Li}, {}^6\text{Li}' + \gamma$) reaction

Nuclear excitations by neutral-current neutrino scattering play an important role in neutrino-nuclear astrophysics. The accurate knowledge of neutral-current neutrino-nucleus cross sections is also important for the observation of astrophysical neutrinos in earth-based neutrino detectors [89].

In a recent review of weak interactions in core-collapse supernovae (CCSNe) and nucleosynthesis, Langanke and Martnez-Pinedo [90] discuss the importance of the comparison of shell-model and RPA calculations with inelastic neutrino-nucleus scattering (INNS) cross section estimates from experimental data. Because astrophysical models rely on theoretical calculations of these kind, and because the available data for comparison is limited at present, the establishment of a new indirect technique to constrain these important theoretical estimates is of high value.

INNS has been argued to be a dissipative mechanism by which neutrinos deposit their energy in nuclear matter during CCSNe [91]. Furthermore, successful CCSNe produce a strong neutrino signal in the tens-of-MeV range which can be detected via the products of charged-current (CC) and neutral-current (NC) weak interactions with nuclei in various detector media. However, measurements relevant for supernovae neutrino detection do not exist for most nuclei, and are highly uncertain where available due to their small cross sections [89]. One method for studying neutrino-nucleus reactions is via direct measurements through neu-

trino spallation at reactor [92] and synchrotron [93] facilities. Only a few measurements have been performed so far, such as the neutrino irradiation of ^{12}C [94, 93].

An alternative approach is via indirect measurements that involve inelastic scattering of other probes, such as (p, p') [95, 96, 97] and (e, e') [98, 99]. Such measurements are much more feasible, and have been used to infer neutral-current neutrino inelastic scattering cross sections in the past [100].

This inference is possible principally because inelastic scattering cross-sections are sensitive to the probe-independent nuclear transition strength. For example, the dominant component of the INNS cross section at astrophysical energies is directly related to the Gamow-Teller (GT) transition strength. The cross section for a transition from an initial (i) and final (f) state is given by [101]

$$\sigma_{i,f}(E_\nu) = \frac{G_F^2}{\pi} (E_\nu - \Delta E_{fi})^2 B(\text{GT}_0)_{fi}, \quad (3.1)$$

where G_F is the Fermi constant, and E_ν and ΔE_{fi} are the energy of the scattered neutrino and the difference between final and initial nuclear energies, respectively. $B(\text{GT}_0)_{fi}$ is the reduced GT strength in the inelastic channel ($\Delta S = 1$, $\Delta T = 1$, and $\Delta T_z = 0$),

$$B(\text{GT}_0)_{fi} = \frac{g_A^2}{2J_i + 1} |\langle f | \hat{O}(\text{GT}_0) | i \rangle|^2, \quad (3.2)$$

where g_A is the axial vector coupling constant, J_i the spin of the initial nucleus. $\hat{O}(\text{GT}_0)$ is the corresponding GT operator,

$$\hat{O}(\text{GT}_0) = \frac{1}{2} \sum_k \hat{\sigma}(k) \hat{\tau}_0(k), \quad (3.3)$$

where $\hat{\sigma} = 2\hat{s}$ and $\hat{\tau} = 2\hat{t}$ are the spin and isospin operators, respectively, and the sum runs over all nucleons in the target. Thus, the allowed component of neutrino-induced nuclear excitations are isovector spin-transfer excitations, with no change in orbital angular momentum.

On the other hand, reactions mediated by hadronic inelastic scattering induce M1 transitions whose operator is given by

$$\hat{O}(\text{M1}) = \sqrt{\frac{3}{4\pi}} \sum_k [g_\ell(k)\hat{\ell}(k) + \frac{1}{2}g_s(k)\hat{\sigma}(k)]\mu_N, \quad (3.4)$$

where $\hat{\ell}$ is the orbital angular momentum operator, and g_ℓ (g_s) is the orbital (spin) gyromagnetic factor. Thus, both isovector and isoscalar transitions contribute, as well as non-spin-transfer transitions (transitions that involve only change in orbital angular momentum).

The isovector (IV) component of the M1 operator can be rewritten as

$$\hat{O}(\text{M1})_{\text{IV}} = \sum_k \sqrt{\frac{3}{4\pi}} \left(g_\ell^{\text{IV}} \hat{\ell}(k) \hat{\tau}_0(k) + \frac{1}{2} g_s^{\text{IV}} \hat{\sigma}(k) \hat{\tau}_0(k) \right) \mu_N, \quad (3.5)$$

with the IV gyromagnetic factors $g_\alpha^{\text{IV}} = (g_\alpha^n - g_\alpha^p)/2$ ($\alpha = \ell$ or s). The spin part of the above isovector M1 operator (Eq. (3.5)) is the same as that of the GT_0 operator (Eq. (3.3)) except for a constant factor. This indicates that the GT_0 strength, which is needed to infer the inelastic neutrino-nucleus cross-sections, can be extracted from hadronic probes such as (p, p') under certain circumstances. Specifically, because the (p, p') probe constitutes a transition of $J_i^\pi = 1/2^+ \rightarrow J_f^\pi = 1/2^+$, and $T_i = 1/2 \rightarrow T_f = 1/2$, it can induce isovector transitions ($\Delta T = 1$) as well as isoscalar transitions ($\Delta T = 0$), both with various contributions of total spin transfer. Therefore, (p, p') is capable of extracting GT_0 strength

where the orbital and isoscalar contributions are negligible [100]. These assumptions are valid primarily for spherically symmetric nuclei with weak or separable isoscalar responses. In general, it would be ideal to have a probe which is capable of extracting the GT_0 strength from inelastic excitations, without consideration of these properties. In this work, a different reaction probe is tested in which isovector spin-transfer excitations can be directly isolated.

The (${}^6\text{Li}, {}^6\text{Li}'[T = 1, T_z = 0, J^\pi = 0^+, 3.56 \text{ MeV}]$) reaction, first suggested by Austin *et al.* [102], provides direct access to the GT_0 response of nuclei in an unambiguous manner, as the quantum numbers of the initial and final states guarantee the induced transition of $\Delta S = 1$, $\Delta T = 1$, and $\Delta T_z = 0$. This selectivity is a distinct feature of the (${}^6\text{Li}, {}^6\text{Li}'$) probe. A simplified level diagram of ${}^6\text{Li}$ is shown in Fig. 3.1, which is drawn based on Ref. [103]. This reaction channel can be identified by tagging the de-excitation γ ray with $E_\gamma = 3.56 \text{ MeV}$. Although the α threshold is located below this state ($Q_\alpha = -1.47 \text{ MeV}$), the α decay from the 3.56 MeV state is forbidden, unlike for other excited states, as it violates parity invariance [103]. Instead, this state decays directly to the ground state via γ emission. Since it has $J^\pi = 0^+$, the branching ratio to the 3^+ state at 2.19 MeV, as well as feeding from other higher excited states is negligible [103]. Therefore, the coincidence measurement with 3.56-MeV γ rays provides clean identification of the reaction.

In order to establish (${}^6\text{Li}, {}^6\text{Li}'$) as a viable indirect probe of INNS cross sections, direct measurements are a necessary benchmark. For this purpose, the ${}^{12}\text{C}({}^6\text{Li}, {}^6\text{Li}')$ measurement was performed as long-baseline direct neutrino measurement data exists [93]. Furthermore, measurements on ${}^{24}\text{Mg}$ and ${}^{93}\text{Nb}$ were also performed. For these latter measurements the 3.56 MeV de-excitation γ -rays were not resolvable. As the tagging of this gamma is the basis for the proposed technique, the gamma background due to the decay of the isoscalar giant resonances must not dominate. In this work it is demonstrated that for heavier nuclei, this

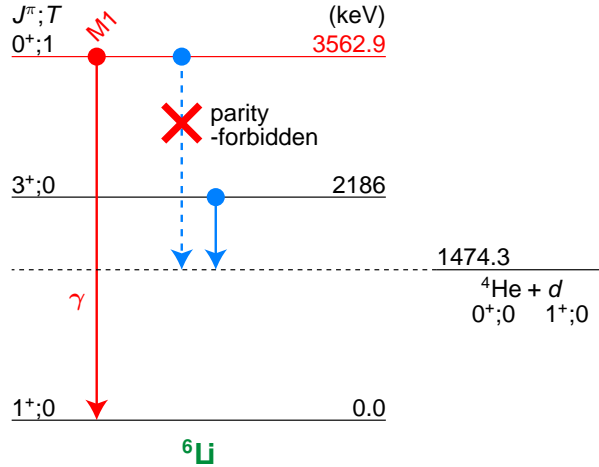


Figure 3.1: A simplified level diagram of ${}^6\text{Li}$ based on Ref. [103]. The α decay of the $J^\pi = 0^+$, $T = 1$ state at $E_x = 3.56$ MeV is parity-forbidden, and thus this state mainly decays to the ground state via γ emission.

background is much stronger than the isovector signal. Thus, the proposed method is likely only applicable for light nuclei due to the proportionally significant contribution of gamma emission from the isoscalar giant resonances in heavier systems.

3.1 Experiment

The ${}^{12}\text{C}({}^6\text{Li}, {}^6\text{Li}')$ measurement was carried out at the Research Center For Nuclear Physics, Osaka University, Japan. A layout of the RCNP facility is shown in Fig. 3.2. A 100-MeV/ u ${}^6\text{Li}$ beam was accelerated via the coupled operation of the azimuthally varying field (AVF) and ring cyclotrons with a measured resolution of ~ 1.75 MeV in FWHM. The beam energy of 100-MeV/ u is well suited for the present study of the spin-isospin response because at this energy the reaction mechanism is simple with small momentum transfer at 0° scattering angle [104].

The ${}^6\text{Li}$ beam was transported achromatically to the WS experimental hall (see Fig. 3.2)

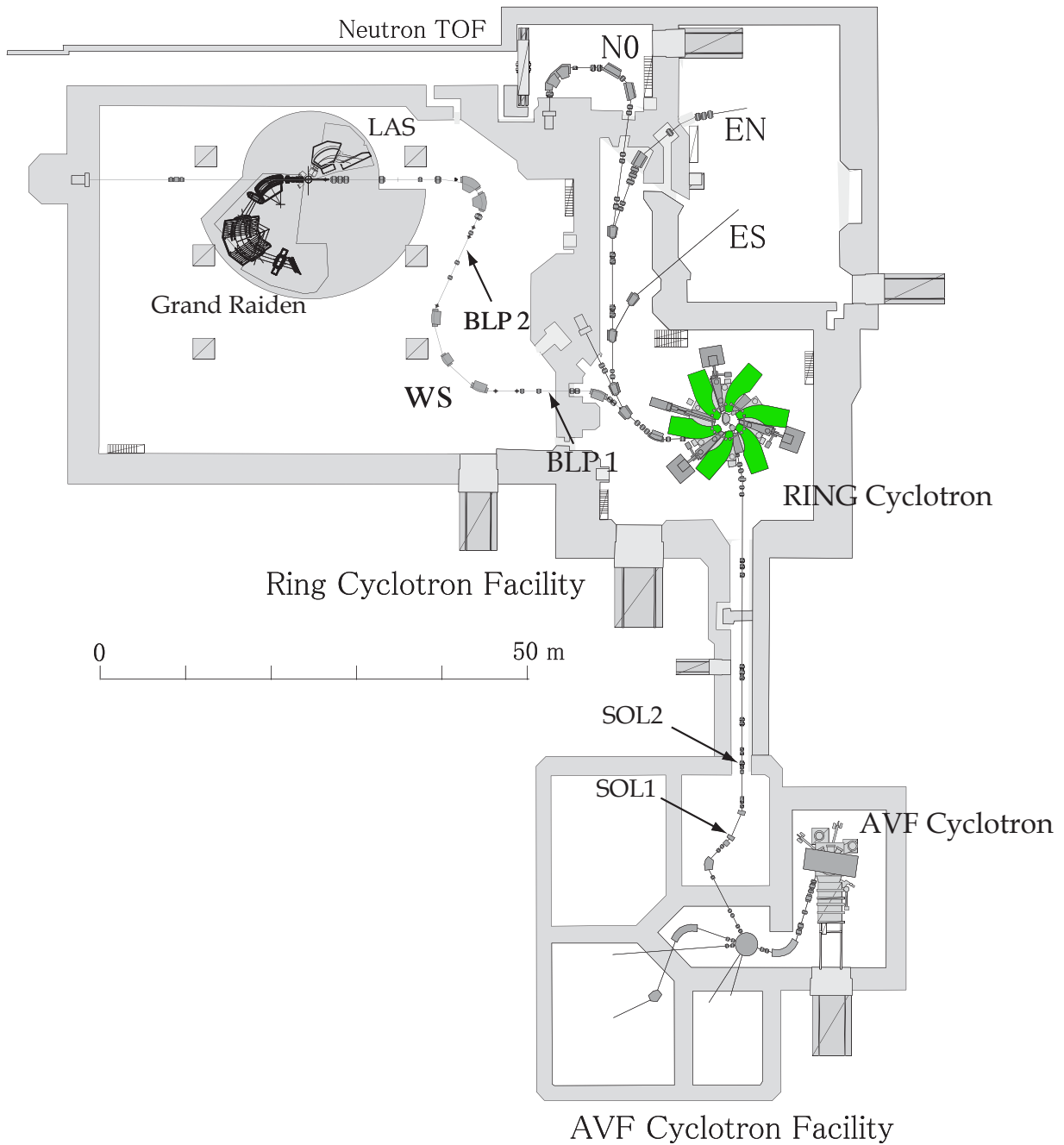


Figure 3.2: The primary facility beam line layout for the Research Center for Nuclear Physics (RCNP) located at Osaka University, Japan. In this experiment, the ${}^6\text{Li}$ beam was transported from the ring cyclotron (shown in green) into the WS hall. It was then transported achromatically to the Grand Raiden target position. See text for details.

where it was impinged upon a $15.21 \text{ mg/cm}^2 \text{ natC}$ target oriented at 22.5° relative to the horizontal plane (yielding an effective thickness of 16.46 mg/cm^2). The beam intensity was measured to be $\sim 1 \text{ pA}$.

3.1.1 The CAGRA+Grand Raiden Coincidence Setup

3.1.1.1 Grand Raiden Spectrometer

The ${}^6\text{Li}$ ejectiles were momentum-analyzed and detected at the focal plane of the Grand Raiden spectrometer [105] in the 0° setting. Figure 3.3 illustrates the layout of the Grand Raiden spectrometer and the end station focal plane detectors. The Grand Raiden focal plane consisted of two Multi-Wire Drift Chambers (MWDCs) and three plastic scintillators of thickness 3 mm, 10 mm, and 10 mm, respectively. Positioned between the two 10-mm plastic scintillators was a 12-mm aluminum plate (shown in red in the bottom panel of Fig. 3.3), which was used to stop the residual ${}^6\text{Li}$ nuclei so that the final scintillator could serve as a veto on the d and ${}^4\text{He}$ products from ${}^6\text{Li}$ breakup. Each MWDC featured two anode wire planes so that positions in both the horizontal and vertical directions could be determined, while the horizontal and vertical angles were inferred using the positions from both MWDCs together. The entire set of focal plane detectors were oriented at a 45° angle relative to the beam axis.

The unreacted beam was dumped through the holes of the MWDCs into the 0-degree Faraday cup located at $\sim 12 \text{ m}$ downstream of the focal plane and was shielded to reduce background for the γ -ray measurement at the target position. The distance between the center of the hole and the edge of the active area of the MWDC was $\sim 20 \text{ cm}$. This distance corresponds to a momentum range which could not be measured with respect to the unre-

acted beam at 0 degree and was $\sim 1\%$, corresponding to ~ 10 MeV for 100 MeV/ u ${}^6\text{Li}$. The resulting excitation-energy spectrum was studied up to 40 MeV.

The plastic scintillators were used for energy-loss measurements and served as a time-of-flight (TOF) start signal, with the cyclotron RF as the stop. Together, the energy loss in the scintillators and the TOF provided the particle identification with which the d , ${}^4\text{He}$, and ${}^6\text{Li}$ could be separated.

As the horizontal scattering angle at the target is determined primarily from the horizontal incident angle at the focal plane, a slight under-focus mode was employed, in which the ion-optical focus of Grand Raiden was placed upstream of the focal-plane MWDCs. In focused mode, the small vertical angular magnification in Grand Raiden results in poor resolution of the reconstructed vertical scattering angle. However, by slightly under-focusing the ion optics the vertical scattering angle at the target becomes strongly dependent on the vertical position in the MWDCs. As the under-focusing is increased, the vertical position range in the focal-plane detectors will span a smaller range of scattering angles at the target and thereby improve the angular resolution [95]. Further details regarding the nominal acceptance, magnification, and resolution of the Grand Raiden spectrometer can be found in reference [106].

3.1.1.2 CAGRA

The target was placed in a scattering chamber which was surrounded by 11 high-purity Germanium (HPGe) clover detectors in the “Clover Array Gamma-ray spectrometer at RCNP for Advanced research”, CAGRA. The CAGRA array of HPGe detectors were of critical importance for the success of the measurement, as they detected the 3.56 MeV γ -ray from ${}^6\text{Li}$ which is emitted when an inelastically induced GT_0 transitions occur in the target. The

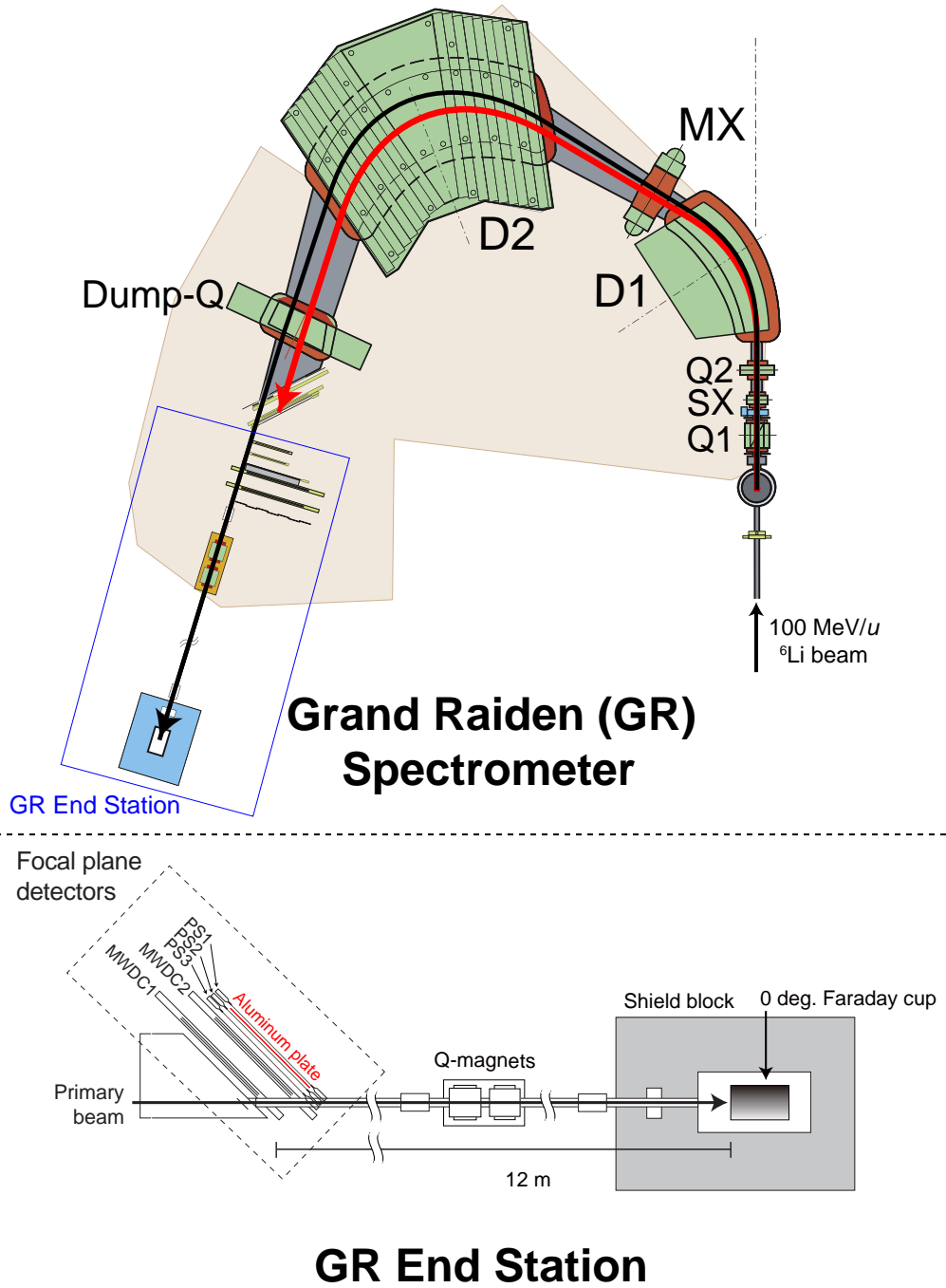


Figure 3.3: Top panel: Layout of the Grand Raiden Spectrometer which was used to momentum analyze the inelastically scattered ${}^6\text{Li}$ nuclei. The spectrometer was configured with seven magnets in the QSQDMDD configuration (where Q, D, S, and M are Quadrupole, Dipole, Sextupole, and Multipole magnets, respectively). Bottom panel: configuration of the spectrometer end station and focal-plane detectors. Figure adapted from [106, 95]. See text for details.

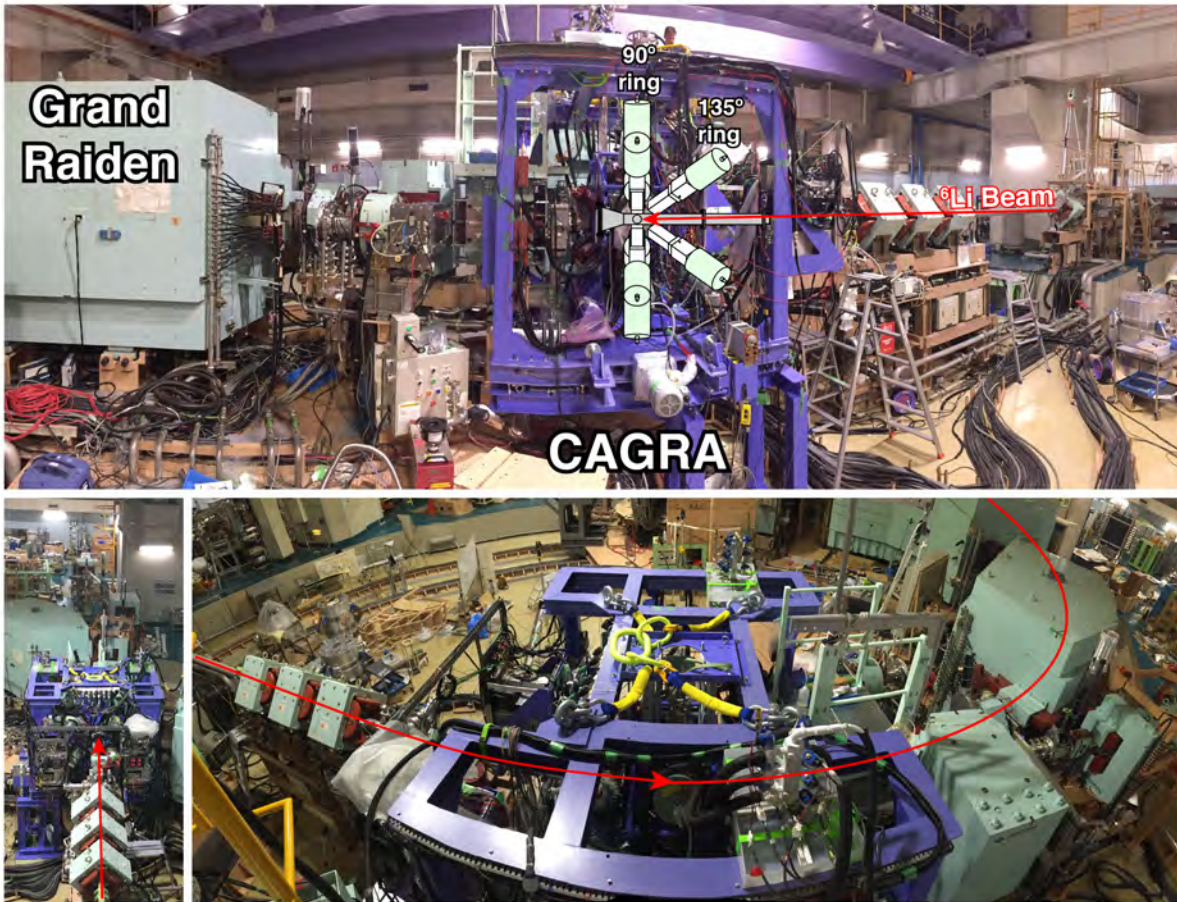


Figure 3.4: The CAGRA array of HPGe clover detectors. CAGRA consisted of two rings of clover detectors with 8 detector slots at 90 degrees and 4 at 135 degrees. There were also 4 forward slots for LaBr₃ detectors at 45 degrees, but they were not used in this work due to their large angular coverage which made Doppler reconstruction challenging.

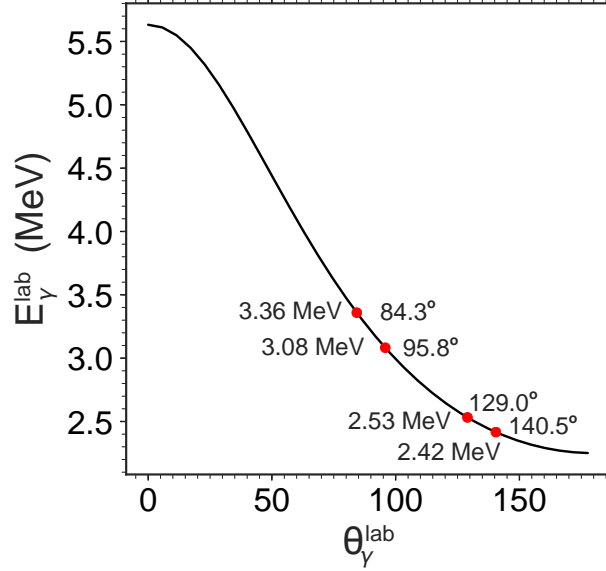


Figure 3.5: The range of energies the 3.56 MeV γ -ray from ${}^6\text{Li}$ in the laboratory frame. The γ -ray emitted from the de-excitation of the ${}^6\text{Li}[0+; T = 1; 3.56\text{MeV}]$ state is 3.56 MeV in the rest frame of ${}^6\text{Li}$. In the laboratory frame this gamma is Doppler boosted due to the momentum of the ${}^6\text{Li}$ ($\beta \sim 0.43$), according to its emission angle in the lab-frame. Shown in red are the clover crystal positions in the CAGRA array. Each clover has crystals at two distinct azimuthal angles. Thus, the two rings of clover detectors span for separate angular ranges. For the purpose of Doppler reconstruction, the centroid of the clover crystal is used as the gamma interaction point.

HPGe clover detectors were configured in the CAGRA array with a ring of 8 detector slots at 90° and 4 at 135° , as shown in Figure 3.4 . Only seven of the eight 90° slots were utilized in this measurement.

Because the ${}^6\text{Li}$ ejectile was moving at a velocity of $\beta \sim 0.43$, the energy of the γ -ray, which is 3.56 MeV in the rest frame, varied from 2.25 MeV to 5.63 MeV in the laboratory frame as shown in Fig. 3.5. Each ring of clovers had two forward crystals and two backward crystals. Thus, the entire array spanned four scattering-angle ranges, the centroids of each (coinciding with the HPGe crystal center) were used as the gamma-ray interaction point for the purpose of Doppler-reconstruction, and are shown as red points in Fig. 3.5. The angular coverage of each clover crystal in the CAGRA array was $\sim 12^\circ$, and the distance between

the target and a germanium crystal was ~ 20.8 cm.

3.2 Methods & Analysis

3.2.1 Data acquisition and analysis framework

In this measurement, Grand Raiden and CAGRA were instrumented with separate data acquisition (DAQ) systems. The Grand Raiden DAQ was run as the master trigger, and thus all singles data were saved, while the CAGRA DAQ was run as a slave, only validating when a trigger in both CAGRA and Grand Raiden were present.

The Grand Raiden DAQ is an analog system that was developed and maintained by Tamii *et al.* [107]. Signals from the left and right photomultiplier tubes (PMTs), attached to either side of the focal plane plastic scintillators, were divided into two signals in order to determine the pulse height (for energy loss information), as well as time discrimination via a CFD (constant fraction discriminator). The output of the CFD was then split and used for time-of-flight information, as well as for a coincidence trigger with the other PMT associated with the same plastic scintillator. The measured live-time ratio for the Grand Raiden DAQ during the $^{12}\text{C}(^6\text{Li}, ^6\text{Li}')$ measurement was ~ 0.82 .

The CAGRA DAQ was newly formed for the campaign of measurements, in which the ^6Li experiment was a part, the details of which will be described in a forthcoming publication. The CAGRA DAQ was instrumented with the same 14bit, 100MHz flash ADCs (analog-to-digital) utilized by the GRETINA tracking-detectors [108] developed at Lawrence Berkeley National Laboratory (LBNL). However, in this campaign, these digitizers were instrumented with customized firmware by Argonne National Laboratory's (ANL) Gammasphere team [109]. This firmware was designed to be highly customizable in order to interface

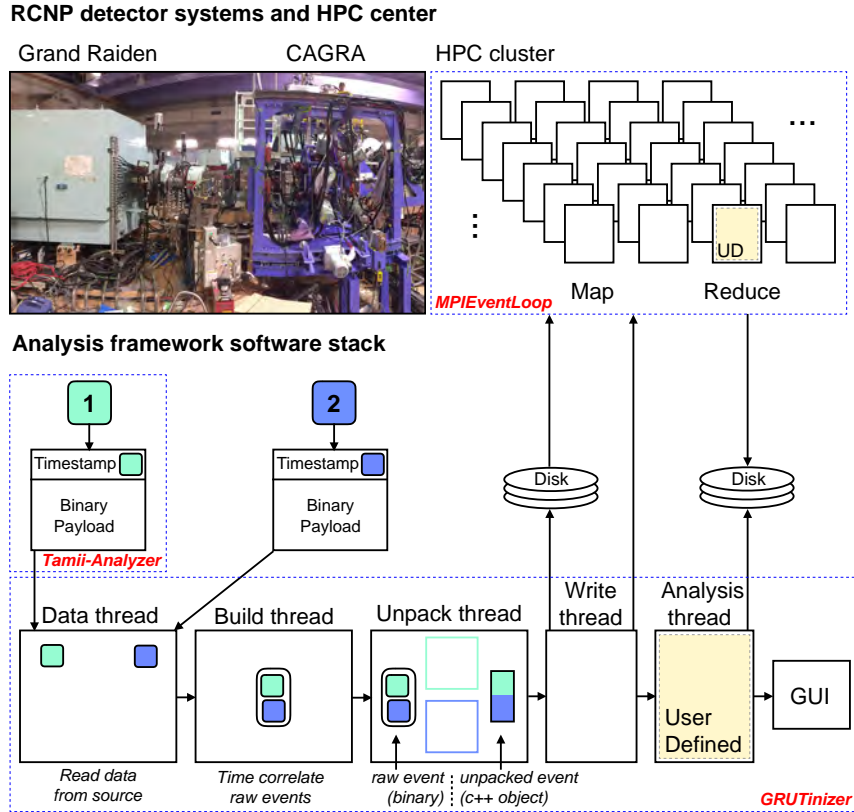


Figure 3.6: The analysis software stack that was used in the RCNP CAGRA+Grand Raiden campaign. Dashed blue lines show application and library boundaries. Solid arrows that cross these boundaries represent communication by local memory, shared memory or disk I/O. See text for details.

with a variety of different detector systems, and to be able to handle very high count rates. The total deadtime of the CAGRA DAQ was measured to be $\sim 4.5\mu s$.

The separate DAQs were synchronized using a MyRIAD module developed at ANL, which was inserted into the Grand Raiden DAQ. The MyRIAD (Multipurpose γ -ray Interface to Auxiliary Detectors) module provided a general purpose interface and clock that could be used in concert with the digital DAQ system utilized by CAGRA. After synchronizing the MyRIAD clock in the Grand Raiden DAQ with the clock in the CAGRA digitizers, timestamps from the separate data streams could be correlated with a sampling resolution of ten nanoseconds.

Since the data streams from each system were written to disk separately, a modular data analysis framework that could accommodate raw data events from a variety of sources was developed. The block-diagram software stack used in this work is shown in Fig. 3.6. The core components were,

- **Tamii-analyzer**: A Grand-Raiden raw event processing and analysis framework [110]
- **GRUTinizer**: Online and offline framework for time-sorting, unpacking, and analyzing events from generic sources [111, 112]
- **MPIEventLoop**: An MPI *mapreduce* implementation for distributed data processing.

The **GRUTinizer** analysis framework, which was originally developed for online and offline analysis at the National Superconducting Cyclotron Laboratory (NSCL), was used for the primary event correlation and unpacking of data from both CAGRA and Grand Raiden. First, raw events were extracted directly from CAGRA and indirectly from Grand Raiden (via the **Tamii-analyzer**) and were time ordered by the data thread of **GRUTinizer**. These heterogeneous event types were then stored in a thread-safe queue from which the next thread, the building loop, could access. The building thread then time-correlated events according to a user-defined time window. Then, these time-correlated events were passed to the unpacking thread (via a threadsafe queue) which was responsible for transforming the binary time-correlated data into user-defined C++ objects. These unpacked events were then written to disk via an I/O thread, and then processed by an analysis thread. The results of which could be displayed via a graphical user interface in real time.

Alternatively, the I/O thread could be used to distribute the processing of the unpacked events to the high performance computing (HPC) center at RCNP. In this mode of operation, the events were mapped to an allocation of CPU nodes which each maintained its own

analysis thread that reduced the events according to a user-defined analysis library. This *map-reduce* functionality was achieved using the Message Passing Interface (MPI) and was built into a generic library for distributed event processing, known as `MPIEventLoop`. In addition to this analysis framework, `MPIEventLoop` has also been implemented into the `ATTPCROOTv2` analysis framework for distributed processing of events from the active target time projections chamber (ATTPC) at NSCL.

Utilizing the above described DAQ and analysis framework, the following sections describe the analysis techniques and transformations used to extract physical quantities from raw experimental observables.

3.2.2 Grand Raiden calibrations

3.2.2.1 Sieve-slit scattering angle reconstruction

In order to infer trajectories of the ^{12}C recoil and ^6Li ejectile at the target position, the scattering angles at the interaction point must be reconstructed from the image in the Grand Raiden focal-plane detectors. Because no calculable ion-optical inverse map from the position and angles in the focal plane exists for Grand Raiden, a calibration measurement with a sieve slit was performed. A perforated block (known as a sieve slit) with regularly placed holes was inserted 60 cm downstream from the target position. This ensured that scattered ^6Li nuclei of only very specific scattering angles would be transported to the focal plane detectors. Because the holes in the sieve slit are known, the scattering angles at the target can then be reconstructed from their image in the focal plane.

The horizontal (dispersive) and vertical (non-dispersive) scattering angles at the target, θ_x and θ_y , were determined via a multivariate fit that depended on the horizontal and vertical

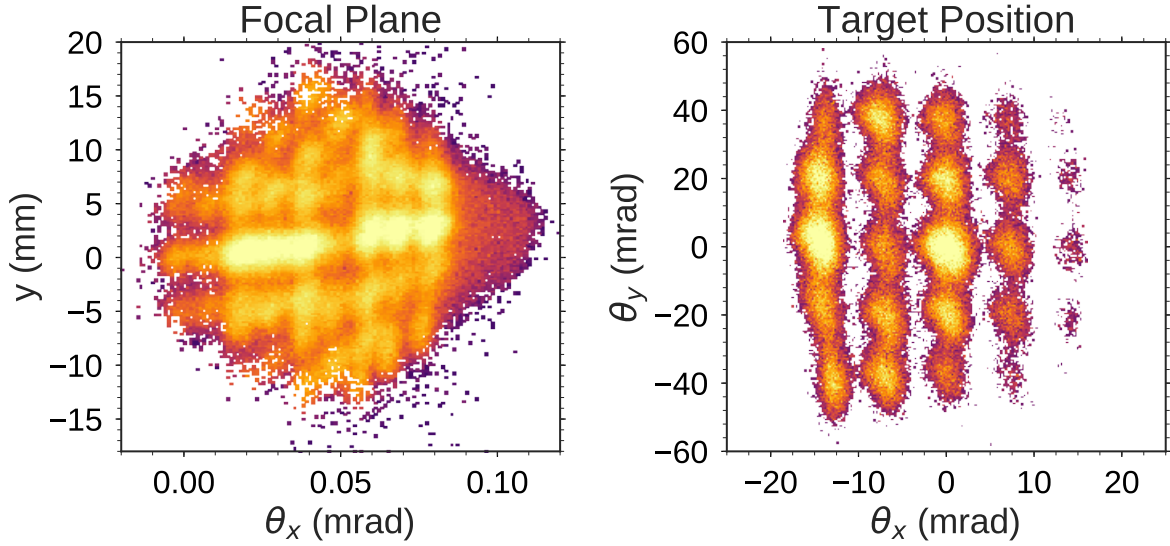


Figure 3.7: The image of the sieve slit in the focal plane for 3 separate magnetic rigidity settings (left) and the reconstructed scattering angles at the target using a least squares fit to Eqs. 3.6 & 3.7 (right).

positions $(x_{\text{fp}}, y_{\text{fp}})$ and angles $(\theta_{\text{fp}}, \phi_{\text{fp}})$ in the focal plane as,

$$\theta_x = c_0 + c_1 x_{\text{fp}} + c_2 \theta_{\text{fp}} \quad (3.6)$$

$$\theta_y = \sum_{i=0}^3 \sum_{j=0}^1 \sum_{k=0}^1 \sum_{l=0}^1 b_{ijkl} x_{\text{fp}}^i y_{\text{fp}}^j \theta_{\text{fp}}^k \phi_{\text{fp}}^l \quad (3.7)$$

where coefficients c_i and b_{ijkl} are the adjusted fit parameters.

Measurements of the sieve-slit image in the focal plane of Grand Raiden were done at several magnetic rigidities, so that the central ray of the elastically scattered ${}^6\text{Li}$ would be incident on different horizontal positions (x_{fp}) in the focal plane. The left panel of Figure 3.7 is an illustration of the sieve-slit image at various horizontal positions in the focal plane. Using the hole centroids of the horizontal and vertical positions and scattering angles in the focal plane, a global least-squares fit was performed using Eqs. 3.6 & 3.7. The coefficients of the best fit were then used in these equations and the result was applied on an event-by-

event basis to the primary measurement data in order to deduce the scattering angles at the target. An image of the reconstructed horizontal and vertical angles at the target for the sieve-slit measurements is shown in the right panel of Figure 3.7. From these, the scattering angles θ and ϕ at the target can be deduced from,

$$\theta = \tan^{-1} \left(\sqrt{\tan(\theta_x)^2 + \tan(\theta_y)^2} \right) \approx \sqrt{\theta_x^2 + \theta_y^2} \quad (3.8)$$

$$\phi = \tan^{-1} \left(\frac{\tan(\theta_y)}{\tan(\theta_x)} \right) \approx \frac{\theta_y}{\theta_x} \quad (3.9)$$

where the small-angle approximation is used for the RHS of Eqs. 3.8 & 3.9.

With the scattering angles calibrated, the angular resolutions for the horizontal and vertical scattering angles at the target were found to be 2.8 mrad and 10.3 mrad, respectively. This yielded a resolution of ~ 10.6 mrad in the scattering angle θ , suggesting that half-degree bins are a reasonable choice for the angular distributions discussed in later sections.

3.2.2.2 Energy calibration

The slope of the momentum calibration for the dispersive (horizontal) position in the focal plane was performed by measuring the elastic scattering peak from the $^{93}\text{Nb}(^6\text{Li}, ^6\text{Li})$ reaction at several magnetic rigidities. The offset was then calibrated using known states in ^{12}C .

In addition, it was found that the energy calibration of Grand Raiden varied as a function of time as can be seen in Figure 3.8. The centroid of the isovector $^{12}\text{C}[2^-; T=1; 19.4 \text{ MeV}]$ state was analyzed in 15 minute intervals and it was found that it varied by 500 keV (on average) over the course of the measurement, as shown in the top panel of Figure 3.8. This time-varying offset in the energy calibration was corrected as shown in the bottom panel.

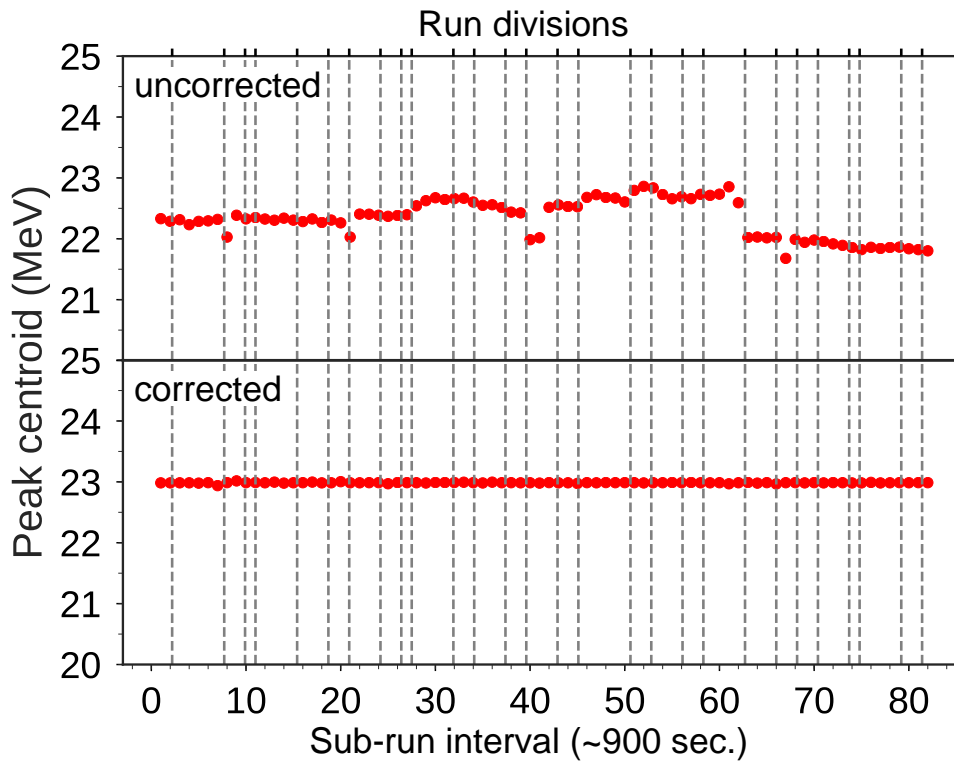


Figure 3.8: The time-dependence of the Grand Raiden energy calibration for the centroid of the $^{12}\text{C}[2^-; T=1; 19.4 \text{ MeV}]$ state in the $^{12}\text{C}(^6\text{Li}, ^6\text{Li}')$ excitation energy spectrum. Due to the coincident excitation of the ^6Li ejectile to its 3.56 MeV state, this isovector state in ^{12}C appears at $\sim 23 \text{ MeV}$ ($=19.4 \text{ MeV} + 3.56 \text{ MeV}$).

3.2.3 CAGRA calibrations

3.2.3.1 Energy calibration

When instrumented with the ANL firmware, the CAGRA digitizers perform minimal analysis, instead choosing to offload processing such as pole-zero and asymptotic baseline corrections to software. The primary energy information saved for each digitizer firing are the pre and post-rise integration windows. In the case of high rates, the gamma-ray energy is calculated as,

$$E_{\gamma} = \text{slope} * \frac{(\Sigma_{\text{post}} - \Sigma_{\text{pre}} \cdot pz)}{M} + \text{offset}(rate), \quad (3.10)$$

where slope and offset are the energy calibration fit parameters, the Σ 's are the pre and post-rise ADC integration sums, pz is the constant pole-zero correction to the pre-rise energy integration, and M is the shaping time or the width of the integration regions ($3.5\mu\text{s}$ in this measurement). The energy calibration slope, offset, and pole-zero corrections were initially determined with standard calibration sources such as (^{60}Co , ^{152}Eu and ^{56}Co).

However, it was found that during production runs with beam, the offset in the energy calibration of Eq. 3.10 varied linearly with the count rate in each crystal. This rate dependence of a specific HPGe crystal signal is demonstrated in Figure 3.9. Panel (a) shows an example count rate as a function of time for the CAGRA array. The centroid of the 511 keV γ -ray was tracked for various count rates and plotted as a function rate in panel (b). Panels (c) and (d) show the response of a specific crystal in the array to variations in the rate. A least squares fit of a linear trend for the gamma energy calibration offset as a function of rate was performed for each HPGe crystal in the array, and then applied on a second-by-second basis to determine the correct gamma-ray energy calibration offset during the production runs. With this method, the rate dependence was corrected as shown in panel (d), and the

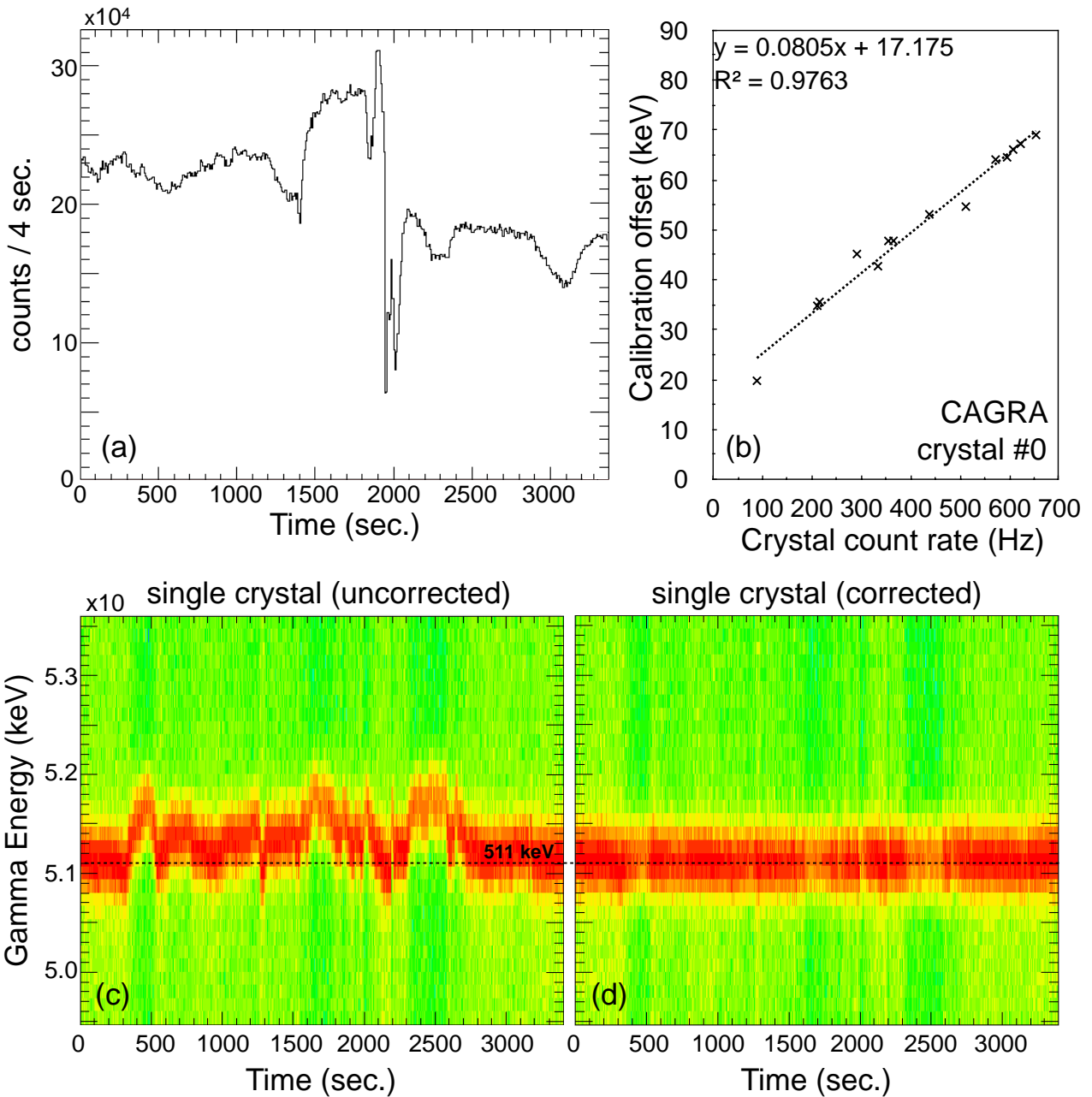


Figure 3.9: Rate dependence of the CAGRA clover crystals. Panel (a) shows an example count rate spectrum as a function of time for the CAGRA array. Panel (b) details the rate dependence of the energy calibration offset for a specific HPGe crystal in the array. This trend was established for each crystal and then used to correct the energy calibration on a second-by-second basis. Panels (c) and (d) show the rate dependent gamma-ray energy and (corrected) rate independent gamma-ray energy for the 511 keV line, respectively.

energy resolution was greatly improved. After having applied this technique, staff at ANL suggested an alternative corrective method that applied the rate dependence to the post- and pre-rise sums individually [113]. This method was applied and was found to provide results comparable to the method described in this work.

3.2.4 Invariant missing mass reconstruction

The reconstruction of the ^{12}C excitation energies for isovector requires two steps: an invariant-mass reconstruction, and a missing-mass reconstruction. Figure 3.10 illustrates the full kinematics for the system, as well as the two intermediate steps. Physically, this occurs because after inducing an isovector transition in the ^{12}C target nucleus, the ^6Li will itself be excited into the $0^+; T=1$ excited state at 3.56 MeV. This intermediate particle, known as the *invariant* will decay via gamma emission into the ^6Li ground state, which will receive a momentum-kick from the de-excitation γ -ray. Thus, the first step in the reconstruction is to combine the measurements of ^6Li ejectile and its de-excitation γ -ray to infer the momentum four-vector of the $^6\text{Li}'$ invariant as,

$$P_{\mu}^{^6\text{Li}'(\text{inv.})} = P_{\mu}^{^6\text{Li}} + P_{\mu}^{\gamma}, \quad (3.11)$$

where each of the four-vectors are in the laboratory reference frame. By inferring the $^6\text{Li}'$ invariant in this way, it can then be combined with knowledge of the ^6Li incident beam to perform a missing-mass reconstruction of the excited ^{12}C recoil. The missing mass of the $^{12}\text{C}'$ is found from the missing energy and missing momentum as,

$$m_{\text{missing}} = \sqrt{E_{\text{missing}}^2 - p_{\text{missing}}^2}. \quad (3.12)$$

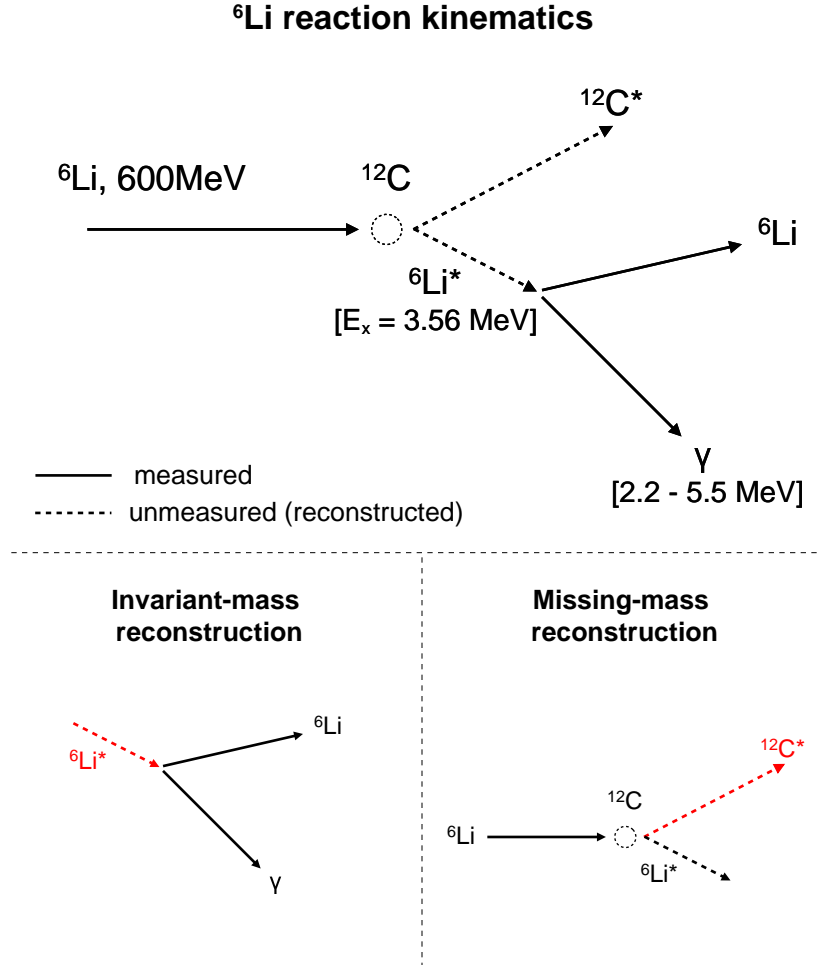


Figure 3.10: The kinematics of the ${}^6\text{Li}$ reaction.

The excitation energy of the recoil is then derived as,

$$E_x({}^{12}\text{C}) = m_{\text{missing}} - m({}^{12}\text{C}). \quad (3.13)$$

The missing momentum and missing energy are calculated from the ${}^6\text{Li}$ invariant of Eq. 3.11 and the incident beam four-vector via standard conservation laws,

$$P_\mu^{6\text{Li}(\text{beam})} + P_\mu^{12\text{C}(\text{target})} = P_\mu^{12\text{C}'(\text{missing})} + P_\mu^{6\text{Li}'(\text{inv.})}. \quad (3.14)$$

However, as the incident beam is not monitored on an event by event basis, uncertainty in the energy and the incident angles of the ${}^6\text{Li}$ primary beam contribute to the resolution of the reconstructed missing-mass excitation energy and scattering angle. From Eq. 3.14 the missing energy and momentum are apparent,

$$E_{\text{missing}} = E_{\text{beam}} + m_{\text{target}} - E_{\text{inv.}} \quad (3.15)$$

and,

$$\mathbf{P}_{\text{missing}} = \mathbf{P}_{\text{projectile}} - \mathbf{P}_{\text{inv.}} \quad (3.16)$$

As the invariant ${}^6\text{Li}'$ is inferred via the measurement of the ${}^6\text{Li}$ ejectile and the de-excitation γ -ray, the missing excitation energy of the ${}^{12}\text{C}$ is fully determined.

It should be noted that in the ${}^{12}\text{C}({}^6\text{Li}, {}^6\text{Li}'){}^{12}\text{C}'$ measurement, only transition in ${}^{12}\text{C}$ which are isovector in nature will cause ${}^6\text{Li}$ to emit the characteristic 3.56 MeV γ -ray. Therefore, the above mentioned invariant-mass + missing-mass spectroscopy only applies to isovector transitions. For the case of isoscalar transitions, the excitation energy in ${}^{12}\text{C}$ can be deduced via a standard missing-mass technique without consideration of any intermediate invariant. (Because isovector transitions in the target necessitate that the 3.56MeV state in ${}^6\text{Li}$ was also populated, energies of the isovector states will be shifted in energy relative to the isoscalar transitions by 3.56 MeV.)

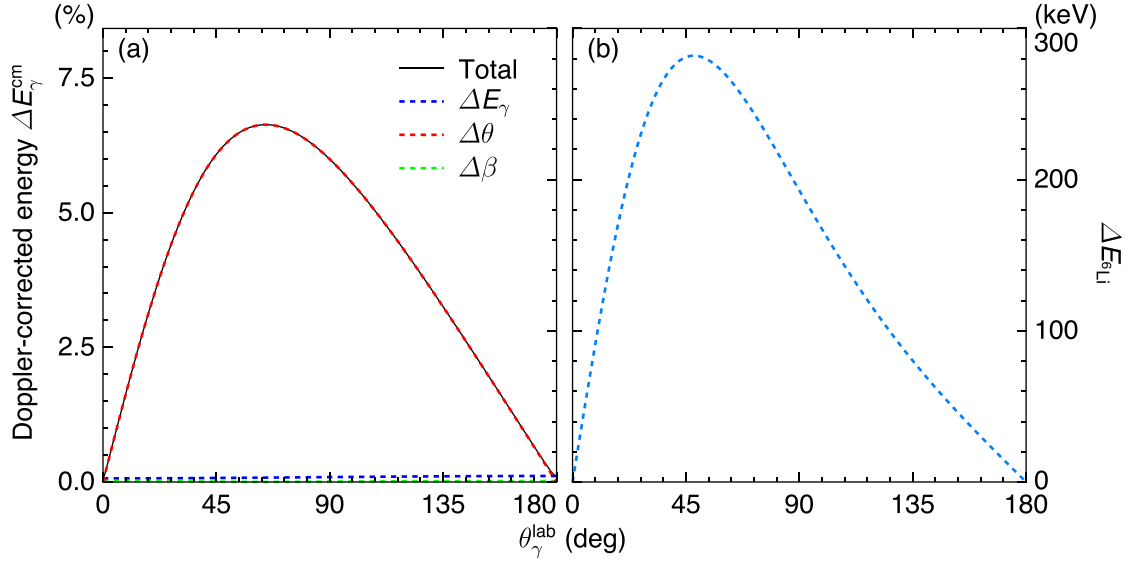


Figure 3.11: (a) A comparison of the contribution of the intrinsic energy resolution, opening angle uncertainty, and velocity spread of the ejectile, to the overall uncertainty in the Doppler reconstructed gamma-ray energy for the detection of the 3.56 MeV de-excitation gamma from ${}^6\text{Li}$ in CAGRA. The uncertainty in the emission angle of the γ -ray is the dominant component of the overall resolution. (b) The resulting estimated resolution of the reconstructed invariant ${}^6\text{Li}$ ejectile given the resolution of the measured de-excitation gamma.

3.2.5 Doppler reconstruction

The Doppler-reconstructed γ -ray energy in the rest frame (cm) of the incident particle, E_γ^{cm} , was obtained from that in the laboratory frame (lab), E_γ^{lab} , as

$$E_\gamma^{\text{cm}} = \gamma(1 - \beta \cos \theta_\gamma^{\text{lab}})E_\gamma^{\text{lab}}, \quad (3.17)$$

where β is the velocity of the projectile, and $\theta_\gamma^{\text{lab}}$ is the γ -ray emission angle in the laboratory frame. This reconstructed γ -ray energy peak is broadened compared with the intrinsic energy

resolution of the detector as,

$$\left(\frac{\Delta E_\gamma^{\text{cm}}}{E_\gamma^{\text{cm}}}\right)^2 = \left(\frac{\Delta E_\gamma^{\text{lab}}}{E_\gamma^{\text{lab}}}\right)^2 + \left(\frac{\beta \sin \theta_\gamma^{\text{lab}}}{1 - \beta \cos \theta_\gamma^{\text{lab}}}\right)^2 (\Delta \theta_\gamma^{\text{lab}})^2 + \left(\frac{\beta \gamma^2 (\beta - \cos \theta_\gamma^{\text{lab}})}{1 - \beta \cos \theta_\gamma^{\text{lab}}}\right)^2 \left(\frac{\Delta \beta}{\beta}\right)^2. \quad (3.18)$$

The first term in Eq. 3.18 corresponds to the intrinsic energy resolution of the HPGe clover detectors and the third term corresponds to the velocity spread of the ejectile, which arises from the unknown reaction point in the target thickness, and is $\Delta\beta/\beta \approx 0.03\%$. Both of these contributions to the uncertainty are marginal compared to the uncertainty of the detection angle due to the finite size (corresponding to an angular coverage of $\Delta\theta_\gamma^{\text{lab}}$) of a single crystal in the CAGRA clover detectors. Figure 3.11a compares the estimated contributions of each component of Eq. 3.18 to the total resolution. Panel (b) of the same figure shows the net effect on the energy resolution of the reconstructed ${}^6\text{Li}$ invariant.

The effect this resolution has on the signal-to-noise of the Doppler-reconstructed de-excitation gamma is significant. As will be described in later sections, the resolvability of this transition above a significant high-energy background due to statistical γ -ray emission from the isoscalar excitations (in particular, the isoscalar giant monopole/dipole resonances (ISGMR/ISGDR)) necessitates high precision angular resolution for the gamma detectors. The large angular coverage of each clover crystal in the CAGRA array ($\sim 12^\circ$), significantly limited the achievable signal-to-noise in this measurement.

3.2.6 Excitation energy resolution

As the energy of this de-excitation gamma is a component in the reconstruction of the invariant (as described by Eq. 3.11), it thereby also contributes to the resolution of the reconstructed excitation energy in ${}^{12}\text{C}$. If one ignores the momentum-kick imparted to the

${}^6\text{Li}'$ ejectile during its decay, the best resolution that can be achieved is analogous to the full width of the Doppler reconstructed gamma energy, $\Delta E=5.5-2.2=3.3$ MeV.¹ This was confirmed via a monte-carlo `Geant4` simulation, which included,

- Realistic beam profile and inelastic scattering reaction mechanism
- Nuclear inelastic excitation of the target/recoil ${}^{12}\text{C}$ and projectile/ejectile ${}^6\text{Li}$ systems
- The decay of the ${}^6\text{Li}'[3.56$ MeV] invariant inflight to the ${}^6\text{Li}[0.0$ MeV] ground state and the emission of the $\gamma[3.56$ MeV].

By analyzing the simulated reaction data and ignoring the decay of the invariant (the momentum-kick of the de-excitation gamma, as mentioned above) the purple line in the left panel of Figure 3.12 represents the simulated best-case reconstruction of the ${}^{12}\text{C}[15.1$ MeV] excited state. The square shape is a direct result of uniform emission of the de-excitation γ -ray's according to $\cos(\theta_{\gamma}^{\text{lab}})$.

However, when compared with the shape of the missing-mass reconstructed excitation energy in the ${}^{12}\text{C}({}^6\text{Li}, {}^6\text{Li}')$ measurement (right panel of Fig. 3.12), the data was found to have a much broader shape. To reproduce this shape, a gaussian beam energy resolution of 1.75 MeV in FWHM was required to smear out the simulated shape (shown as the black crosses in the left panel of Fig. 3.12). This width was determined by fitting simulations with different beam energy resolutions to the data. The red line in the left and right panels of the same figure produced the best fit to the data and corresponds to an intrinsic beam energy resolution of 1.75 MeV. Prior to the measurement, the beam energy resolution was expected to be on the order of a few hundred keV, but due to problems with the cyclotrons and difficulty tuning the ${}^6\text{Li}$ beam, the resolution was much worse.

¹The square purple line shape in Fig. 3.12 has exactly this width.

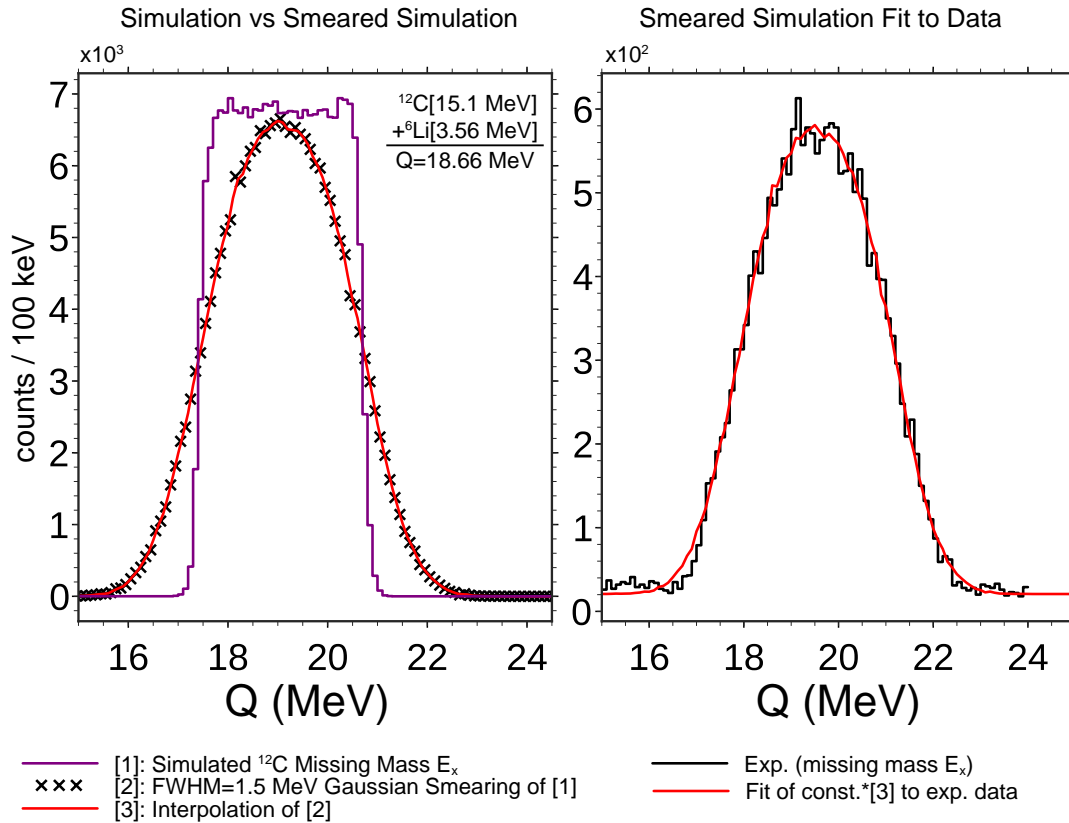


Figure 3.12: Comparison of the simulated reconstruction of the $^{12}\text{C}[1+;T=1;15.1 \text{ MeV}]$ excited state with the measured result. In the left panel, the purple line represents the (simulated) best-case scenario for the missing mass reconstruction of the 15.1 MeV peak, if the invariant $^6\text{Li}[0+;T=1;3.56 \text{ MeV}]$ is ignored. By comparing this with the data in the right panel, it is apparent that the data follows a much broader distribution. In order to reproduce the data, the simulated missing mass reconstruction of this state in ^{12}C (purple) had to be smeared with a gaussian of a variety of widths. The shape of the smeared state was interpolated and fit to the data using a normalization factor. The best fit was found with a gaussian smearing of FWHM=1.75 MeV (shown by the black scatter crosses and red line in the left and right panels, respectively). The smearing that was required suggests that the intrinsic beam energy resolution was 1.75 MeV.

3.2.7 Cross-section calculations

The final step in the data analysis procedure was to evaluate the excitation-energy and center-of-mass scattering-angle dependent differential cross sections for states populated in ^{12}C . The differential cross section for the $^{12}\text{C}(^6\text{Li},^6\text{Li}')$ singles and coincidence data was calculated as,

$$\frac{d\sigma}{d\Omega} = \frac{Y}{N_b N_t \mathcal{L} \eta d\Omega \epsilon_\gamma}, \quad (3.19)$$

where Y is the yield (integrated number of counts over a given energy and angular range), $N_{b,t}$ are the number of incident ^6Li beam particles and ^{12}C nuclei in the target, \mathcal{L} is the average live-time of the DAQ (82%), η is the efficiency of the MWDCs, $d\Omega$ is the solid-angle corrected for the angular acceptance of Grand Raiden, and ϵ_γ is the efficiency of the CAGRA array at detecting the $E_\gamma = 3.56$ MeV γ -ray in the laboratory frame (note that the CAGRA efficiency was only used in the the calculation of the coincident $^{12}\text{C}(^6\text{Li},^6\text{Li}'+\gamma)$ cross-section). The evaluation of each component in Eq. 3.19 is detailed in the following list,

- Y : The yield was measured by integrating the number of counts in each energy and angular bin after applying the ^6Li gamma-coincidence of the prompt events (prompt-random ratio of 3.3 ± 0.3) and background subtraction. The background subtraction is described in section 3.3.1.
- N_t : The number of ^{12}C nuclei in the $15.21 \text{ mg/cm}^2 \text{ natC}$ target, positioned at an angle of 22.5 degrees, was calculated as,

$$N_t = \frac{15.21 \text{ mg/cm}^2}{\cos(22.5^\circ)} \frac{98.9\% (^{12}\text{C}/^{\text{nat}}\text{C})}{1.9926 \cdot 10^{-20} \text{ mg}/^{12}\text{C}} = 8.17 \cdot 10^{20} \text{ cm}^{-2} \quad (3.20)$$

- N_b : The normalization of the number of incident ^6Li beam particles was the leading

order uncertainty in this measurement and is described in section 3.2.7.1.

- $d\Omega$: The acceptance corrected opening angle for each angular bin was calculated as,

$$d\Omega = 2\pi \mathcal{C} \cdot \int_{\theta_i}^{\theta_f} \sin\theta \cdot d\theta \quad (3.21)$$

where $\theta_{i,f}$ are the boundaries of the center-of-mass angular bin. \mathcal{C} is the angle dependent acceptance correction factor for the Grand Raiden spectrometer. The nominal acceptance of Grand Raiden in the horizontal and vertical angles is ± 20 mrad and ± 70 mrad, respectively. Therefore, in order to extract angular distributions beyond 20 mrad in laboratory scattering angle, an acceptance correction to $d\Omega$ is required. Because the angular distributions are azimuthally invariant (constant with respect to ϕ), and because the acceptance in the vertical (non-dispersive) angle was much greater than the horizontal angle, the full acceptance angular distribution along $\theta = \theta_y$ (where $\theta_x \approx 0$) was used to determine the shape of the angular distribution. From this shape, the required acceptance correction could be determined for horizontal and vertical scattering angles where the acceptance was cut.

- \mathcal{L} : The average live-time ratio of the Grand Raiden DAQ determined from the readout; the live-time ratio was 82% for the ^{12}C measurement.
- η : The voltage of the four anode wire planes in the MWDCs was optimized for peak efficiency using a pilot ^6Li beam at the beginning of the experiment. The total efficiency η was then estimated as $\eta = \eta_1\eta_2\eta_3\eta_4 = 0.74$ where η_i was between 91-93% for the approximate efficiency of each anode plane.
- ϵ_γ : The efficiency of the CAGRA HPGe clover array to the ^6Li 3.56 MeV de-excitation

γ -ray, which is Doppler boosted to the energies shown in Fig. 3.5 for the four distinct crystal positions in the CAGRA array. The energy dependency of the efficiencies for each clover were determined via a `Geant4` simulation and were then fit to absolute efficiency measurements made with the CAGRA array using calibrated sources. The measured intensity was corrected for the deadtime of the clover crystal readout ($4.5\mu\text{s}$), which was only a $\sim 1.5\%$ effect given a rate of 3.4 kHz. The non-uniform angular distribution of the gamma-emission from the moving frame was also accounted for on a per crystal basis using `Geant4`. Altogether, the uncertainty in the estimated gamma efficiency calibrations were much smaller than that of the incident beam normalization. The aggregated efficiency of the CAGRA array to the 3.56 MeV gamma was found to be $\sim(0.44\pm 0.03)\%$.

3.2.7.1 Normalization of the number of incident particles

Following the primary measurement, absolute normalization measurements were made in which the incident beam intensity was measured with a Faraday cup at the entrance of the WS experimental hall. The differential cross section for the singles data in this normalization run was then used to normalized the summed spectra of all the $^{12}\text{C}(^6\text{Li},^6\text{Li}')$ data. This method was chosen because it was believed that the transmission to the faraday cup at 0° was not constant over the course of measurement, nor during the normalization runs, and thus a run-by-run, or instantaneous normalization using the scalar data would not have been reliable.

The uncertainty in the normalization produced in this way was dominated by the uncertainty in the ^6Li beam intensity during the normalization runs. The primary component of this uncertainty came from the relatively low rate which was near the tolerance of the beam

monitor, and which appeared to fluctuate on the $\sim 20\%$ level between normalization runs.

The uncertainty in the incident particle normalization, as well as the time-dependent energy variation discussed in the previous section, together lend evidence that variations in the ${}^6\text{Li}$ beam integrity may have been present throughout the experiment.

3.2.7.2 Multipole Decomposition Analysis

Various multipole contributions to the cross sections were extracted via a multipole decomposition analysis (MDA) [114]. In the MDA, a linear combination of theoretical angular distributions, each with different units of angular momentum transfer, were fit to the measured differential cross section,

$$\left[\frac{d\sigma}{d\Omega}\right]_{\text{Total}} = c_1 \cdot \left[\frac{d\sigma}{d\Omega}\right]_{\Delta L=0} + c_2 \cdot \left[\frac{d\sigma}{d\Omega}\right]_{\Delta L=1} + c_3 \cdot \left[\frac{d\sigma}{d\Omega}\right]_{\Delta L=2}. \quad (3.22)$$

The theoretical differential cross sections for the (${}^6\text{Li}, {}^6\text{Li}'$) reactions that are utilized in the MDA have been estimated by means of Distorted Wave Born Approximation (DWBA) calculations. The theoretical angular distributions chosen for the MDA were the combination of $\Delta L = 0, 1$ and 2 components that provided the best overall fit. The microscopic DWBA code `fold/dwhi` [115] was used to estimate differential cross-sections by double-folding a nucleon-nucleon (NN) interaction, in the form of a t -matrix, over transition densities of the projectile-ejectile and target-residual systems. This calculation requires five principle components,

1. An effective nucleon-nucleon (NN) interaction which describes the coupling of the projectile (${}^6\text{Li}$) and target (${}^{12}\text{C}$) nuclei.
2. One-body transition densities (OBTDs), which describe the overlap of the initial and

final nuclear many-body states in the projectile/ejectile (${}^6\text{Li}$ - ${}^6\text{Li}$) and target/recoil (${}^{12}\text{C}$ - ${}^{12}\text{C}$) systems.²

3. Single particle radial wave functions of the participant nucleons in the presence of a many-body core.
4. Optical model potentials which describe the distortion of the incoming and outgoing nuclear wave functions by the target/recoil system.
5. Kinematics and spin variables describing the incident projectile energy, the reaction Q-value, as well as the spin, isospin, and parity quantum numbers of the projectile and target systems.

By the virtue of performing the inelastic scattering measurement at 100 MeV/ u , many of the complicated reaction mechanisms known to obscure the nucleon-nucleus interaction are circumvented via the impulse approximation [104]. The requirement of calculation inputs

1. – 5. above can be seen in a straightforward derivation of the NN t -matrix.

For elastic scattering, the exact t -matrix can be written as,

$$T = \langle \chi^+ | V | \psi^- \rangle \quad (3.23)$$

where ψ^- is the full incoming wave function, χ^+ is an outgoing distorted plane-wave, and V is the interaction potential (+ and – indicate outgoing and incoming, respectively). In first order DWBA, the full incoming wave function is approximated by an incoming plane-wave

²One-body transition densities weight the contribution of one-particle one-hole (1p-1h) transitions between single-particle orbits, and thus provide a way to connect the single-particle wave functions (and nucleon operators) to the many-body system.

that is distorted by an optical model potential (**4.** from above),

$$T = \langle \chi^+ | V | \chi^- \rangle. \quad (3.24)$$

However, for inelastic scattering and charge-exchange reactions in which isospin transfer occurs, the elastic scattering potential V must be replaced by a form factor that contains information about the structure of the participant nuclei (OBTDs, **2.** from above) and the nature of the NN -interaction (**1.** from above). The t -matrix is then,

$$T = \langle \chi^+ | F[R] | \chi^- \rangle \quad (3.25)$$

$$F[R] = \langle B, b | \mathcal{V} | A, a \rangle \quad (3.26)$$

where $F[R]$ is the form-factor, and \mathcal{V} is a many-body potential acting on the many-body states of the projectile (a), target (A), ejectile (b) and recoil (B). In general, many-body operators, such as \mathcal{V} , can be expanded in second-quantized form to make its action on each nucleon in the composite many-body state explicit,

$$\mathcal{V} = \sum_{pq} \langle \phi_p | V_{\text{eff}} | \phi_q \rangle \hat{a}_p^\dagger \hat{a}_q. \quad (3.27)$$

Here, V_{eff} is the effective NN interaction, the ϕ 's are the single particle wave functions of the nucleons in the reaction system (**3.** from above), $\hat{a}_q/\hat{a}_p^\dagger$ are 1p-1h creation and annihilation operators, and the sum runs over all 1p-1h excitations.

By applying second quantization as in Eq. 3.27 for the two-body operator which acts on the target/recoil and projectile/ejectile systems, the form-factor in Eq. 3.26 can be written

as,

$$F[R] = \langle B, b | \sum_{pqrs} \langle \phi_p^B \phi_q^b | V_{\text{eff}} | \phi_r^A \phi_s^a \rangle \hat{a}_p^\dagger \hat{a}_q^\dagger \hat{a}_r \hat{a}_s | A, a \rangle, \quad (3.28)$$

where the sum over indices p, q, r , and s refers to 1p-1h excitations in the recoil, ejectile, target and ejectile systems, respectively. This second quantized expression for the form-factor can then be factored into densities, which represent the overlap of the initial and final many-body states (the one-body transition densities, OBTDs),

$$F[R] = \sum_{pqrs} \langle B | [\hat{a}_p^\dagger \hat{a}_r] | A \rangle \langle b | [\hat{a}_q^\dagger \hat{a}_s] | a \rangle \langle \phi_p^B \phi_q^b | V_{\text{eff}} | \phi_r^A \phi_s^a \rangle \quad (3.29)$$

$$= \sum_{pqrs} \text{OBTD}(A_q B_p) \text{OBTD}(a_s b_r) \langle \phi_p^B \phi_q^b | V_{\text{eff}} | \phi_r^A \phi_s^a \rangle, \quad (3.30)$$

where the $\text{OBTD}(A_q B_p)$ and $\text{OBTD}(a_s b_r)$ are the one-body transition densities for the target/recoil and projectile/ejectile systems, respectively. Letting $\rho_{pq} = \text{OBTD}(p, q) \phi_p \phi_q$ it's then readily apparent that this form-factor is simply double folding the target-recoil and projectile-ejectile densities over the nucleon-nucleon effective interaction,

$$F[R] = \sum_{pqrs} \langle \rho_{AB} | V_{\text{eff}} | \rho_{ab} \rangle \quad (3.31)$$

$$= \sum_{pqrs} \int \int d\xi_{AB} \cdot d\xi_{ab} \cdot \rho_{AB}(\xi_{AB}) V_{\text{eff}} \rho_{ab}(\xi_{ab}), \quad (3.32)$$

where ξ_{ab} (ξ_{AB}) are the relative spatial coordinates between the projectile and the ejectile (target and recoil).

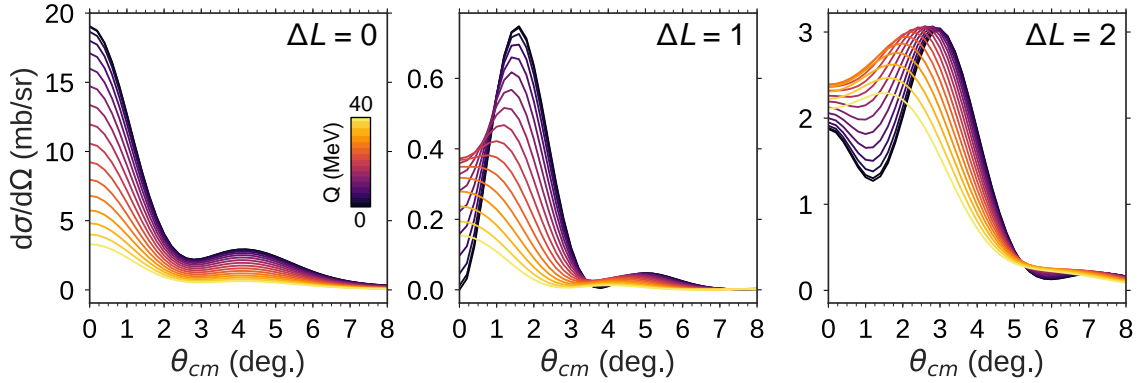


Figure 3.13: Calculated angular distributions for isovector spin-transfer excitations of different orbital angular momentum transfer for the $^{12}\text{C}(^6\text{Li}, ^6\text{Li}')$ inelastic scattering measurement. Each panel is the angular distribution for a particular angular momentum multipole, and the different color lines are the excitation energy (Q -value) dependence of the angular distribution.

Finally, the optical-model potentials are used to calculate the incoming and outgoing distorted waves χ , and are then used with the double-folded effective NN t -matrix as,

$$T_{fi} = \left\langle \chi_f^+(\vec{k}_f, \vec{R}) \left| F[R] \right| \chi_i^-(\vec{k}_i, \vec{R}) \right\rangle, \quad (3.33)$$

where $k_{i,f}$ is the initial and final momentum vector for the distorted wave (5. from above).

The angular distributions are calculated via the standard t -matrix formalism as,

$$\frac{d\sigma}{d\Omega} = \left(\frac{\mu}{2\pi\hbar^2} \right)^2 \frac{k_f}{k_i} |T_{fi}|^2,$$

where μ is the reduced mass of the outgoing particle.

Thus, items 1. – 4. in the above list are necessary and sufficient for DWBA estimates that can be used to extract the multipole components of the $^{12}\text{C}(^6\text{Li}, ^6\text{Li}')$ differential cross section. For this particular analysis, these items were chosen as follows,

- **NN-interaction:** The effective interaction used in the t -matrix parameterization was

the effective NN interaction by Franey and Love at 140 MeV [104], which has been very successfully applied to heavy-ion induced charge-exchange and inelastic scattering reactions in the past [116, 117, 118].

- **OBTDs:** The one-body transition densities for the ${}^6\text{Li}$ and ${}^{12}\text{C}$ systems were calculated with the configuration-interaction shell-model code `oxbash` [119]. The Cohen-Kurath (6-16)CKI interaction [120] was used in the p -shell model space to calculate the transition densities for ${}^6\text{Li}$, and the WBP interaction [121] was used in the $spsdpf$ -shell model space to calculate the transition densities for the ${}^{12}\text{C}$ system.
- **Single-particle wave functions:** The single-particle radial wave functions were calculated with the program `WSAW` [115] by matching the binding energy of a single-particle wave-function outside a closed-core, to the single-particle binding energies calculated in `oxbash` with the subprogram `dens`. These calculations employed the SkX skyrme interaction [122].
- **Optical Model Potential:** The optical model potential (OMP) used to compute the ${}^6\text{Li}-{}^{12}\text{C}$ entrance and exit channels were fit from ${}^{12}\text{C}({}^6\text{Li}, {}^6\text{Li})$ elastic scattering data taken at 600 MeV [123]. The OMP parameters were fit utilizing the `ecis` [124] code and the resulting best fit parameters were -60.94 MeV, 1.3725 fm, and 0.9142 fm for the depth (V), radius (r_v), and diffuseness (a_r) of the real Wood-Saxon potential and -22.529 MeV, 1.610 fm, and 0.693 fm for the depth (W), radius (r_w), and diffuseness (a_w) of the imaginary Wood-Saxon potential.
- **Kinematics & quantum numbers** The reaction calculations were performed using an incident total kinetic energy of 600 MeV/ u for the ${}^6\text{Li}$ projectile. Furthermore, the projectile-ejectile system underwent the transition from $J^\pi = 1^+(T = 0) \rightarrow 0^+(T =$

1), while the target-recoil system underwent the $J^\pi = 0^+(T = 0) \rightarrow 1^+(T = 1)$ transition. Since parity (π) is unchanging in these transitions, the change in total angular momentum J is due purely to spin-transfer reactions $\Delta S = 1$. The quantum numbers for J^π and T for each system were the final component necessary for the reaction calculations described in this section.

Angular distributions for isovector spin-transfer excitations of different orbital angular momentum transfer for the $^{12}\text{C}(^6\text{Li}, ^6\text{Li}')$ inelastic scattering reaction are shown in Figure 3.13. Angular distributions for separate angular momentum multipoles are shown, and the calculations are performed over a range of excitation energies, corresponding to the excitation energy range measured in the experiment. The multipole decomposition of the measured cross-section with these angular distributions is discussed in the following section.

3.3 Results

3.3.1 The $^{12}\text{C}(^6\text{Li}, ^6\text{Li}' + \gamma)$ measurement

The coincident particle–gamma-ray spectroscopy measurement achieved via the use of the Grand Raiden spectrometer and the CAGRA clover array is illustrated in Figure 3.14 in which the coincident gamma-rays are shown as a function of excitation energy in ^{12}C . Both the laboratory and center-of-mass frame gamma-ray energies are shown (top and bottom panels, respectively), from which a comparison of the 15.1 MeV state in ^{12}C reveals the Compton edge and photopeak of the 3.56 MeV gamma-ray emitted in-flight from ^6Li . Without performing the doppler reconstruction, gammas from this state are spread out in the lab frame as can be seen in the top panel of Fig. 3.14.

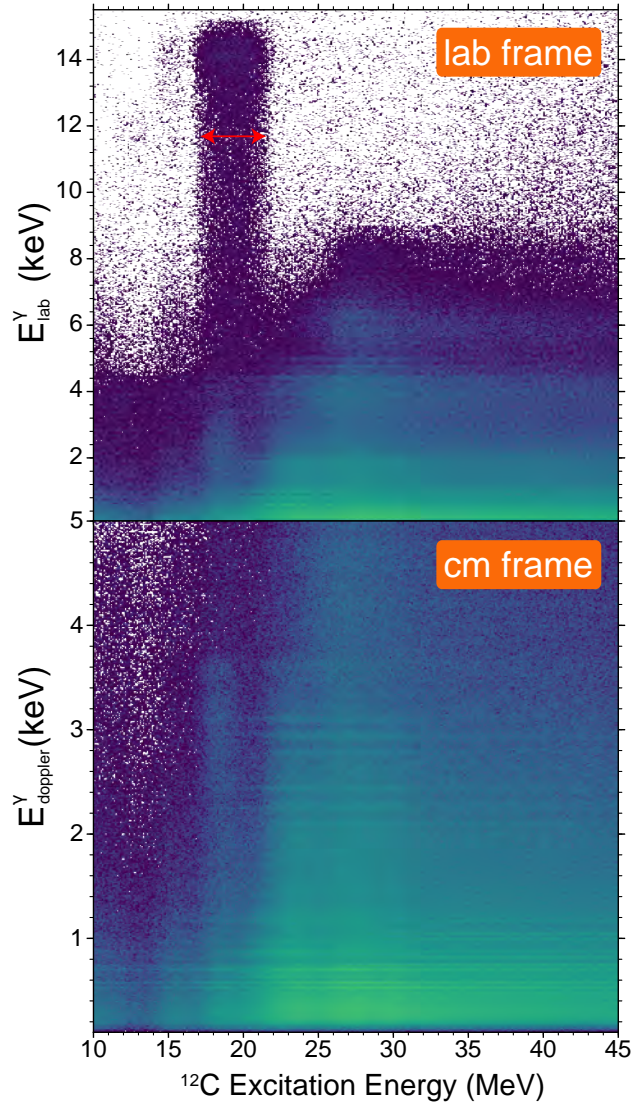


Figure 3.14: The gamma-ray energy and target excitation energy matrix for the $^{12}\text{C}(^6\text{Li}, ^6\text{Li}' + \gamma)$ reaction. In the top panel, the gamma energies shown are those measured in the detectors, without any transformation applied and in the bottom panel, the gamma energies have been Doppler reconstructed according to the clover crystal angular positions. Both panels are drawn as a function of the excitation energy in ^{12}C which is calculated via the missing mass formalism. The red arrow in the top panel indicates the width of the $^{12}\text{C}(15.1 \text{ MeV})$ state owing to the momentum kick that is imparted to the ^6Li and which is not accounted for in the missing-mass-only reconstruction. This width is analogous to the FWHM of the excitation energy spectrum shown in Figure 3.12. By comparing the two panels, the effect of the doppler reconstruction can be seen, where the photopeak and Compton edge owing to the 3.56 MeV gamma from ^6Li is more prominent in the bottom panel after reconstruction. In addition, gamma decay from the strong isoscalar resonance (occurring above 20 MeV in excitation energy) is clearly evident.

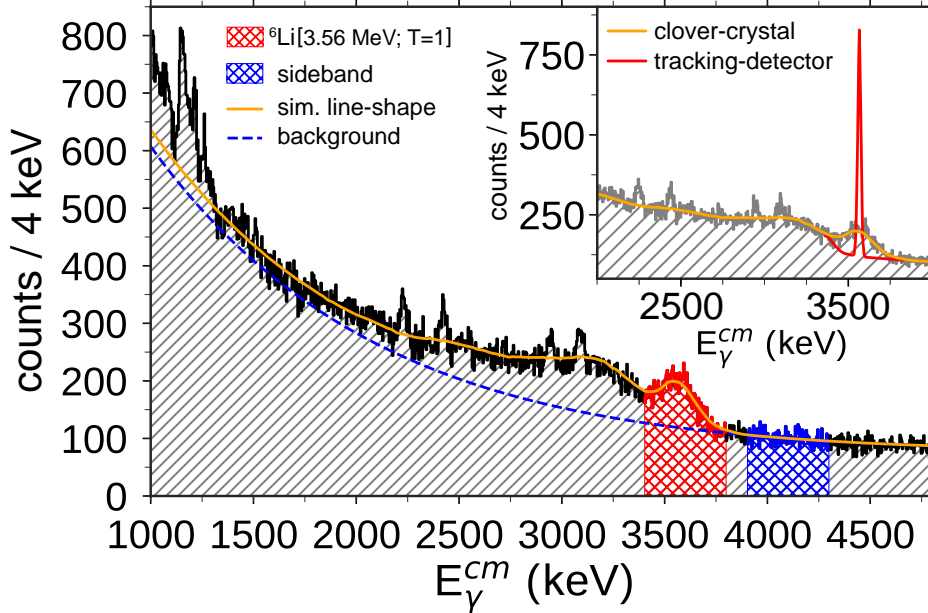


Figure 3.15: The Doppler-corrected γ -ray energy gated on the $^{12}\text{C}[15.1 \text{ MeV}; T=1]$ state for emphasis. The 3.56 MeV γ -line from the $^6\text{Li}[0+; T=1]$ excited state is clearly evident. The resolvability of this γ -ray is crucial for tagging isovector spin-transfer reactions in the target nucleus. The inset plot compares the signal to noise achieved with the clover detectors to what is expected were a gamma-ray tracking detector was utilized. See text for details.

The Doppler reconstructed γ -ray energy spectra in coincidence with the population of the $^{12}\text{C}[15.1 \text{ MeV}; T=1]$ state is shown in Figure 3.15. The yellow line shape shown in the spectrum is the simulated response of the CAGRA array to the 3.56 MeV Doppler reconstructed gamma, fit to the measured data. The blue line is the double exponential background component of the fit. Shown in the red cross-hatched region is the 3.56 MeV photopeak. Just below this region in energy, a convolution of the Compton distribution and escape peaks for the 3.56 MeV gamma can be clearly seen. The four distinct peaks in the region below the photopeak are from a single gamma transition at rest, in the target, that has been distributed in energy according to the four angular ranges covered by the CAGRA array.

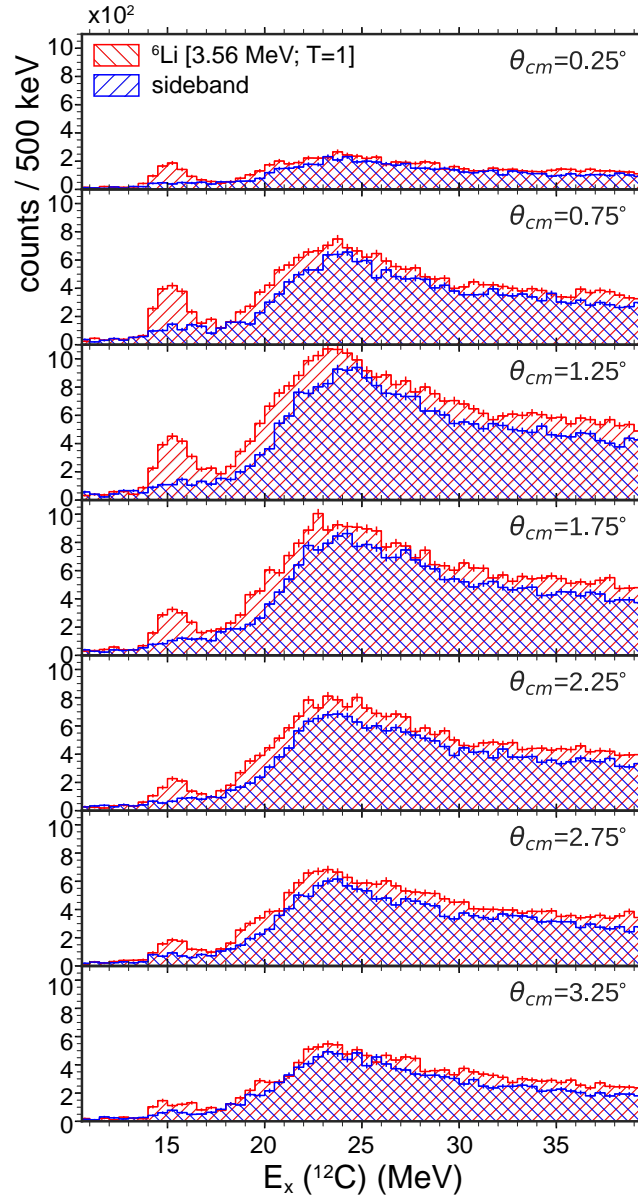


Figure 3.16: The reconstructed excitation energy spectrum of ^{12}C , for different angular bins, when applying the two gates shown in the Doppler-reconstructed gamma energy spectrum (Fig. 3.15). The red spectrum corresponds to the 3.56 MeV photopeak gate, and the blue spectrum corresponds to the sideband, representative of the gamma background in the photopeak gate. The $^{12}\text{C}[1+; T=1; 15.1 \text{ MeV}]$ state, which is populated via an isovector spin-transfer reaction, is clearly seen in the photopeak gated spectra, but not in the sideband data.

By gating on the region shown in red ($E_{cm}^\gamma = 3.4 \text{ MeV} - 3.8 \text{ MeV}$) and subtracting a scaled sideband representative of the background contribution (shown in blue; $E_{cm}^\gamma = 3.9 \text{ MeV} - 4.3 \text{ MeV}$)³, the coincident invariant missing-mass excitation energy for pure isovector ($\Delta T = 1$) spin-transfer ($\Delta S = 1$) transitions in ^{12}C can be extracted. The excitation energy spectrum for each of these gamma gates is shown in Fig. 3.16. Even without performing the sideband subtraction, the Gamow-Teller transition to the (1+;T=1;15.1 MeV) state and the isovector spin-dipole transition to the (2-; T=1; 19.4 MeV) can be easily seen as excess counts in the $^6\text{Li}[0+;T=1;3.56 \text{ MeV}]$ gated spectra (red) over the sideband (blue).

Figure 3.17 compares inelastic scattering for the $^{12}\text{C}(^6\text{Li}, ^6\text{Li}')$ singles cross section to the $^{12}\text{C}(^6\text{Li}, ^6\text{Li}' + \gamma)$ coincident cross section (the subtraction of the red and blue spectra in Fig. 3.16). The singles data is dominated by the isoscalar resonances in ^{12}C , shown in grey. Making the coincidence measurement with the $\Delta S = \Delta T = 1$ transition in ^6Li by gating on the corresponding de-excitation gamma, the isovector spin-transfer excitations in ^{12}C are identified (black).⁴

The novelty of the ^6Li probe is its ability to separate the proportionally weak isovector spin-transfer excitations from the strong isoscalar excitations. Figure 3.17 displays this selectivity. Whereas the $^{12}\text{C}'[1+; T = 1; 15.1 \text{ MeV}]$ is located in the shoulder of the isoscalar resonances in the singles data, this state is easily resolved using the gamma-coincidence tag

³A wide sideband of $\sim 400 \text{ keV}$, as shown in Fig. 3.15, was often not practical due to contamination from other gamma lines in this region. In practice, a narrower sideband from 3.8 - 3.9 MeV was used. Furthermore, the counts from the sideband must be scaled to match the expected background in the region of the 3.56 MeV photopeak. This was done by using the ratio of the integral of the double exponential background fit, an example of which can be seen as the blue dashed line in Fig. 3.15. As this ratio changes with the amount of background gamma contamination (which is a function of excitation energy of ^{12}C), an excitation energy dependent sideband scaling factor was utilized.

⁴The difference in energy scales shown in Fig. 3.17 is an offset of 3.56 MeV, where the reaction Q-value for isovector spin-flip transitions includes the the excitation energy of the target nucleus *and* the commensurate excitation of the ^6Li nucleus. Therefore, in order to recover the excitation energy spectrum for the $^{12}\text{C}(^6\text{Li}, ^6\text{Li}' + \gamma)$ coincident measurement, the $^6\text{Li}'[0+; T = 1; 3.56 \text{ MeV}]$ invariant must be reconstructed prior to the missing mass reconstruction (see section 3.2.4).

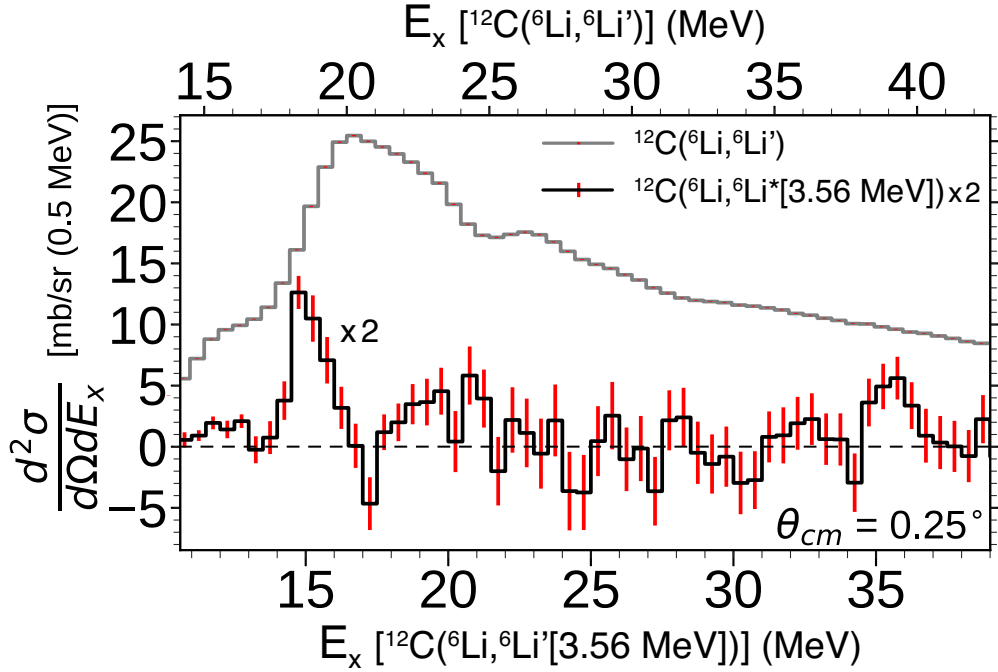


Figure 3.17: Comparison of the ^{12}C inelastic scattering singles and coincidence excitation energy dependent double differential cross section for the $^{12}\text{C}(^6\text{Li}, ^6\text{Li}')$ and the $^{12}\text{C}(^6\text{Li}, ^6\text{Li}' + \gamma)$ reactions, respectively. The coincidence spectrum shown is the result of the subtraction of the differential cross section resulting from a gate on the photopeak of the 3.56 MeV γ -ray and a sideband in the region directly above this gamma (shown as the red and blue cross-hatched regions in Fig 3.15, respectively). The coincidence spectrum corresponds to the isovector spin-transfer excitations in ^{12}C , whereas the singles spectrum contains all types of transitions but is primarily dominated by isoscalar excitations. See text for details.

proposed in this work.

With the methods described in section 3.2.7.2, theoretical cross sections for the ${}^6\text{Li}$ - ${}^{12}\text{C}$ system were calculated for excitations of isovector, spin-transfer reactions ($\Delta T = 1, \Delta S = 1$) with multipoles of $\Delta L = 0, 1$, and 2. The calculated angular distributions with distinct orbital angular momentum transfer are shown in Fig. 3.13. To decompose the entire excitation energy spectrum of ${}^{12}\text{C}$, angular distributions for each of these multipole components were calculated in a range from 0-40 MeV (indicated by the colored lines in Fig. 3.13). These energy dependent theoretical cross-sections were then fit to the angular distributions for each excitation energy bin of the data, according to equation 3.22.

The multipole-decomposed double differential cross section for the ${}^{12}\text{C}({}^6\text{Li}, {}^6\text{Li}' + \gamma)$ reaction as a function of excitation energy in ${}^{12}\text{C}$ and center-of-mass scattering angle, is shown in Fig. 3.18. The differential cross sections were corrected for the acceptance of Grand Raiden, the detector live-time ratios, as well as the efficiency of the CAGRA array for the 3.56 MeV γ detection (see section 3.2.7). The angular distributions for the 15.1 MeV Gamow-Teller transition and the 19.4 MeV spin-dipole transition are shown in the right panel of Fig. 3.18. With the aide of the multipole decomposition analysis described above, the different multipole components of the ${}^{12}\text{C}$ excitation energy are extracted.

Shown in red in left panel of Fig. 3.18 are the ($\Delta T = 1, \Delta S = 1, \Delta L = 0$) components of the ${}^{12}\text{C}$ spectra at different scattering angles. As expected, the strong transition to the ${}^{12}\text{C}[15.1 \text{ MeV}; T=1]$ state can be clearly identified and is dominated by $\Delta L = 0$. This is also clearly seen in the top right panel of Fig. 3.18 which illustrates that the angular distribution for this state is primarily $\Delta L = 0$. Thus, the ${}^6\text{Li}$ probe's unique selectivity together with a multipole decomposition can uniquely identify states populated via GT_0 transitions ($\Delta T = 1, \Delta S = 1, \Delta L = 0$). The extracted angular distribution for this state

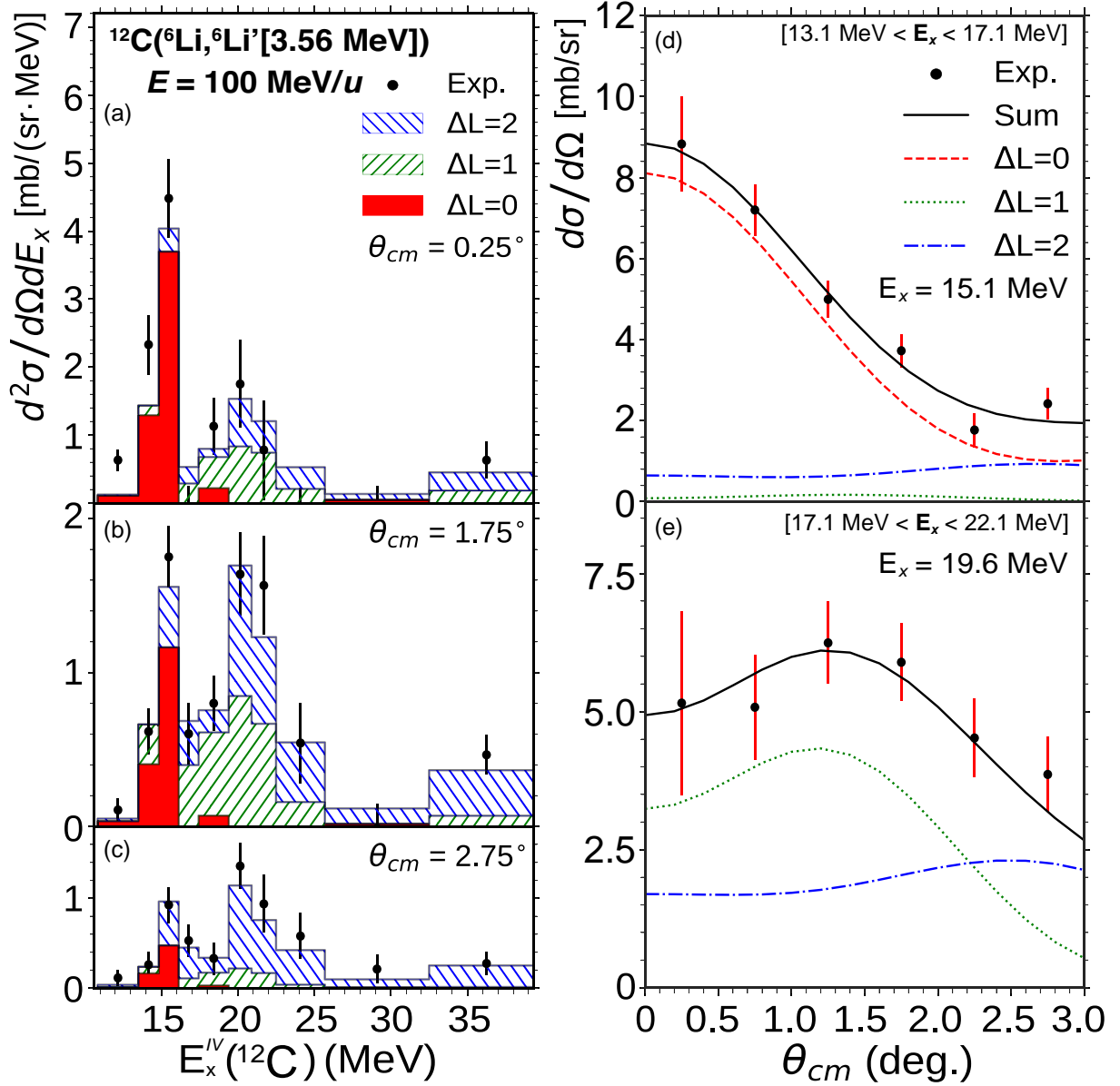


Figure 3.18: Double differential cross section for the $^{12}\text{C}(^6\text{Li}, ^6\text{Li}' + \gamma)$ reaction as a function of excitation energy and center of mass scattering angle, in which the 3.56 MeV state was measured in coincidence. Due to conservation of spin and isospin, this coincidence measurement extracts the isovector spin-transfer response of ^{12}C . In addition, a multipole decomposition analysis (MDA) has been performed utilizing DWBA angular distributions to extract the components of orbital angular momentum transfer. Shown in the right panel are the angular distributions for states in ^{12}C dominated by Gamow-Teller transitions (top panel) and spin-dipole transitions (bottom panel). The absolute scale has a systematic uncertainty of $\pm 20\%$ due to uncertainty in the beam normalization which is not depicted in the statistical error bars.

is shown in the upper right panel of Fig. 3.18 in which the three components of the MDA fit, and their sum, are shown. This state is almost purely $\Delta L = 0$, with a small $\Delta L = 2$ component at larger scattering angles.

This result compares well to the analogous angular distribution excited through charge-exchange reactions on ^{12}C into ^{12}B populated via the $^{12}\text{C}(t, ^3\text{He})$ reaction [125]. For the case of $N=Z$ nuclei such as ^{12}C , charge-exchange provides equivalent selectivity. In general, however, it is difficult to select the analogous inelastic isovector spin-transfer excitations via charge-exchange for $N \neq Z$ nuclei. This is because the analog states in the charged-exchange channel ($\Delta T_z = \pm 1$) are suppressed due to the large Clebsch-Gordan coefficients that occur when the ground state isospin (which scales roughly with the isospin projection $T \approx T_z = \frac{1}{2}(N - Z)$) is non-zero.

From the results for ^{12}C shown in Fig. 3.18, it is clear the $(^6\text{Li}, ^6\text{Li}^*[3.56\text{MeV}])$ reaction is suitable for isolating the isovector-spin excitation energy spectrum in the inelastic channel which establishes this probe as the inelastic analog to spin-transfer charge-exchange reactions. Furthermore, with comparison to the direct $^{12}\text{C}(\nu, \nu')$ neutrino measurement of Ref. [126], we see that the $(^6\text{Li}, ^6\text{Li}^*[3.56\text{MeV}])$ reaction populates the same states thereby confirming this probe's utility as an indirect technique for constraining INNS cross sections.

3.3.2 The $(^6\text{Li}, ^6\text{Li}^*)$ unit cross-section

The proportionality between Gamow-Teller transition strength and reaction cross sections at scattering angle $\theta = 0^\circ$, has been well established in the context charge-exchange reactions [127, 125]. In a similar way, the inelastic Gamow-Teller (GT_0) matrix elements can be deduced from the measured differential cross sections by applying the empirically established unit cross-sections from charge-exchange under the assumption of isospin symmetry [128].

For charge-exchange, this proportionality relation has been written as,

$$\frac{d\sigma}{d\Omega}(0^\circ) = \hat{\sigma}_{\text{GT}} F(q, \omega) B(\text{GT}), \quad (3.34)$$

where σ_{GT} is the unit cross section, $F(q, \omega)$ is a kinematical factor correcting for non-zero momentum and energy transfer, and $B(\text{GT})$ is the reduced GT transition strength. This relationship was originally established for $(p, n)/(n, p)$ reactions [129] and subsequently applied to many inelastic and charge-exchange reactions at medium energy [130]. Analogously, the corresponding relation for the present (${}^6\text{Li}, {}^6\text{Li}'$) reaction is,

$$\frac{d\sigma({}^6\text{Li}, {}^6\text{Li}')}{d\Omega}(0^\circ) = \hat{\sigma}_{\text{GT}_0}({}^6\text{Li}, {}^6\text{Li}') F(q, \omega) B(\text{GT}_0), \quad (3.35)$$

with $\hat{\sigma}_{\text{GT}_0}({}^6\text{Li}, {}^6\text{Li}')$ the Gamow-Teller unit cross section (UCS) for this reaction and $B(\text{GT}_0)$ is the $\Delta T_z = 0$ (inelastic) Gamow-Teller transition strength.

From the β -decay data of ${}^{12}\text{B}$ and ${}^{12}\text{N}$, the GT transition strengths for the transitions from the ${}^{12}\text{C}$ ground state to the ground states of ${}^{12}\text{B}$ and ${}^{12}\text{N}$, which are both analogs of the transitions from ${}^{12}\text{C}$ ground state to the 15.1 MeV state in ${}^{12}\text{C}$, are determined to be 0.99 and 0.88, respectively. For the determination of the unit cross section $\hat{\sigma}_{\text{GT}_0}({}^6\text{Li}, {}^6\text{Li}')$, the average of these measurements was adopted. The Gamow-Teller strength for the transition to the 15.1 MeV analog state of the ${}^{12}\text{B}$ ground state was also calculated via OXBASH [119] using the Cohen-Kurath (8-16)POT interaction in the p -shell-model space [120], and found to be 0.921, which agrees well with the average strength of the beta-decay measurements. Utilizing Eq. 3.35, the ${}^{12}\text{C}({}^6\text{Li}, {}^6\text{Li}'[3.56\text{MeV}])$ unit cross section was found to be 11.3 ± 2.7 mb/sr. The unit cross section was also determined from the DWBA calculation and found

to be in agreement (11.325 mb/sr) with the data. Finally, the unit cross section was also determined from the analog transition in the $^{12}\text{C}(^6\text{Li},^6\text{He})$ data [?] with a value of ~ 10 mb/sr. Although it was not possible to determine an error from the data presented in Ref. [?], this value is also in good agreement with the present results.

Following the established mass dependence of the unit-cross section for $(t,^3\text{He})$ and $(^3\text{He},t)$ reactions [125], it is postulated here that the ^6Li Gamow-Teller unit cross section decreases with target mass as

$$\hat{\sigma}_{\text{GT}0}^{(^6\text{Li},^6\text{Li}')} (A) = N \exp(-xA^{1/3}). \quad (3.36)$$

where N , and x are fit parameters. The original intention of this work was to use the ^{24}Mg and ^{93}Nb measurements to constrain the above fit parameters with data, thereby determining the mass dependence of the UCS fully. However, it was found that the signal-to-noise (S/N) for the ^6Li 3.56 MeV γ -ray was low enough to be unresolvable for the ^{24}Mg and ^{93}Nb measurements (see section 3.3.3). Thus, to infer the mass dependences of the Gamow-Teller UCS, the experimentally determined UCS for ^{12}C was supplemented with theoretical DWBA calculations.

Theoretical DWBA estimates for ^{12}C and ^{26}Mg , as well as four heavier doubly-closed nuclei, ^{48}Ca , ^{78}Ni , ^{132}Sn , and ^{208}Pb were made, as well as calculations for their Gamow-Teller transition strengths. One-body transition densities (OBTDs) for ^{12}C were calculated using the same interaction as described previously and were calculated for ^{26}Mg using the USDA interaction in the sd -shell-model space [131]. The OBTDs for the heavier nuclei were obtained via normal-mode calculations with the code NORMOD [132]. Optical-model potentials (OMP) for the DWBA calculations were taken from Refs. [133, 134].

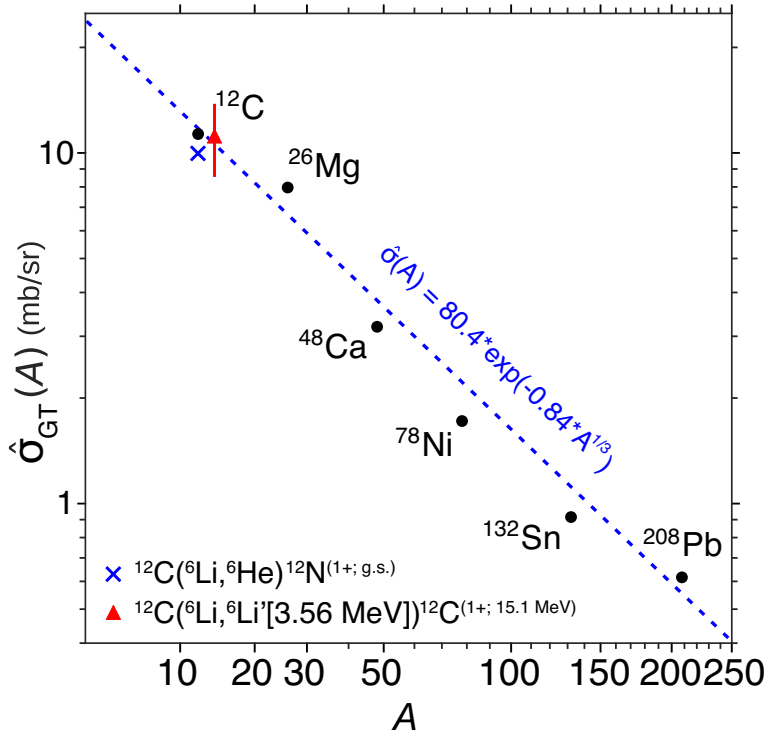


Figure 3.19: The mass dependence of the Gamow-Teller unit cross-section for ${}^6\text{Li}$ calculated from theoretical estimates of the inelastic GT strength and DWBA estimates for the cross section of several nuclei (black). Filled circles indicate that the underlying GT strengths were estimated via shell-model or normal-modes calculations. A postulated unit cross section mass-dependence for heavy-ion reactions (Eq. 3.36) is fit to these theoretical unit cross-sections and is shown in the plot (dashed black line). In addition, the experimentally derived Gamow-Teller UCS for the inelastic (${}^6\text{Li}, {}^6\text{Li}'$) reaction established in this work is shown alongside an estimated unit cross section from data available for the (${}^6\text{Li}, {}^6\text{He}$) charge-exchange reaction [135]. The error bar shown for the inelastic UCS includes systematic and statistical uncertainties, while no error on the charge-exchange data was available.

The theoretical estimates for the ${}^6\text{Li}$ UCS are shown in Figure 3.19. Performing a least squares fit of equation 3.36 to these calculations, the fit parameters N and x are found to be 80.4 mb/sr and 0.840, respectively, and the fit result is shown as the dashed blue line in the figure. The theoretical DWBA estimates follow the postulated mass dependence very well. Furthermore, for ${}^{12}\text{C}$, the theoretical Gamow-Teller unit cross-section (11.3 mb/sr) agrees well with the measured unit cross-section for the $({}^6\text{Li}, {}^6\text{Li}')$ probe as can be seen in Fig. 3.19.

In addition, Laurent *et al.* [135] investigated the ${}^{12}\text{C}({}^6\text{Li}, {}^6\text{He}){}^{12}\text{N}$ charge-exchange reaction where they found a cross section of ~ 7.2 mb/sr for the population of the ${}^{12}\text{N}$ ground state at 100 AMeV and $(\theta = 0 \pm 1.3)^\circ$. Under the assumption of isospin symmetry, the charge-exchange transition to the ${}^{12}\text{N}$ ground state is analogous to the inelastic population of the 15.1 MeV state in ${}^{12}\text{C}$ that is discussed above.⁵ Indeed, comparing the charge-exchange differential cross section of [135] with the $({}^6\text{Li}, {}^6\text{Li}' + \gamma)$ inelastic differential cross section for this state at zero-degrees (8.84 mb/sr), we see that the measurements agree within the systematic uncertainty of the present study. A rough estimate of the unit cross section for the $({}^6\text{Li}, {}^6\text{He})$ reaction is made assuming pure (L=0) and is shown in Fig. 3.19. Given this agreement, and the good agreement of both measurements with the calculations, the inelastic Gamow-Teller unit cross section for the $({}^6\text{Li}, {}^6\text{Li}' + \gamma)$ reaction is reasonably well constrained.

Finally, it should be further noted that the conclusion of equation 3.36 and the above described measurements and calculations, is that the isovector spin-transfer cross-sections will decay exponentially with the nuclear mass number. This fact, and the discussion in the next section, illustrate why the ${}^6\text{Li}$ de-excitation gamma was ultimately not resolvable in

⁵The Clebsch-Gordan coefficients are also the same for the ${}^{12}\text{C}({}^6\text{Li}, {}^6\text{Li}')$ and ${}^{12}\text{C}({}^6\text{Li}, {}^6\text{He})$ measurements.

the heavier systems that were investigated.

3.3.3 Competition with isoscalar resonances

The utility of the ${}^6\text{Li}$ probe relies on the resolvability of the 3.56 MeV γ -ray from the de-excitation of its $0^+; T=1$ excited state. As this γ -ray is Doppler boosted from the decay in flight, significant improvement in the signal-to-noise (S/N) could be achieved by using a γ -ray tracking detector such as GRETINA where the nominal interaction position in the HPGe crystals can be deduced to within 2-mm [136, 137, 138]. Assuming equivalent efficiency, shown in the inset plot of Fig. 3.15, the yellow and red line-shapes compare the simulated response of the CAGRA clover detectors and a tracking detector with 2 mm resolution, respectively. As illustrated in Eq. 3.18, the resolution of the reconstructed center of mass gamma energy is directly proportional to the angular resolution of the detector. For this reason, the resolution of the tracking-detector is estimated to be an order of magnitude better than what was achievable using the clover-type HPGe detectors in CAGRA, due primarily to the large angular coverage of the clover crystals. While the S/N in the ${}^{12}\text{C}$ measurement was sufficient to resolve the 3.56 MeV γ -ray of interest, for the measurements of ${}^{24}\text{Mg}$ and ${}^{93}\text{Nb}$ the signal could not be resolved.

The number of resolved counts in the 3.56 MeV peak for the ${}^{12}\text{C}$ measurement (~ 19250) can be used to estimate the S/N that would be observed in heavier systems. Assuming a $B(\text{GT}_0) \sim 1$, as is the case for the transition to the ${}^{12}\text{C}[1^+; T = 1; 15.1 \text{ MeV}]$ state, over a similar excitation energy range (5 MeV), only ~ 3700 counts are estimated to be measured in ${}^{24}\text{Mg}$, and only ~ 300 in ${}^{93}\text{Nb}$ for comparable run times and target thicknesses. Figure 3.20 compares the expected signal-to-noise for the 3.56 MeV gamma in the ${}^{24}\text{Mg}$ and ${}^{93}\text{Nb}$ measurements, given the measured unit cross-section for ${}^{12}\text{C}$. The purple line in the

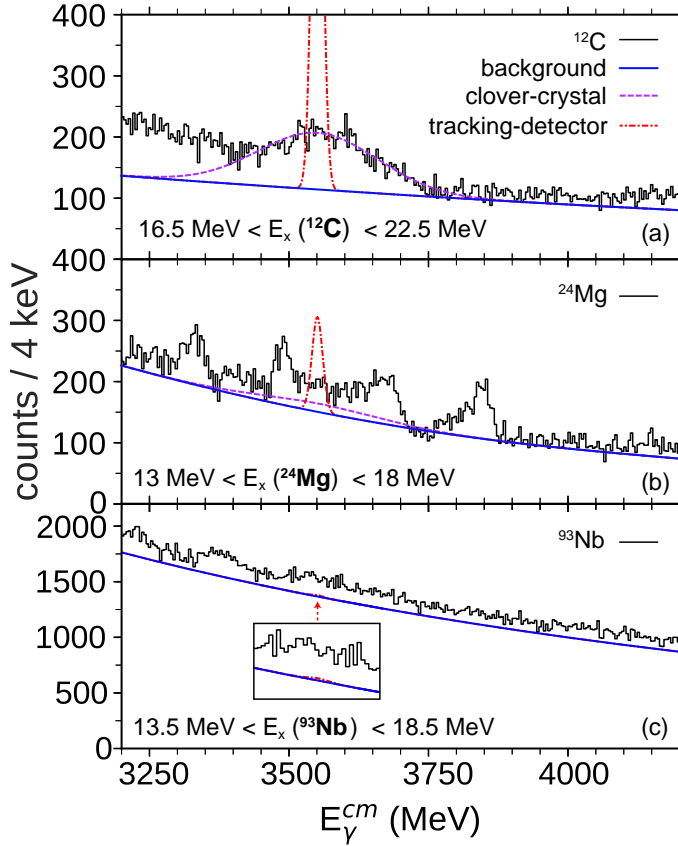


Figure 3.20: Comparison of the achievable signal-to-noise for the 3.56 MeV γ -ray emitted from inelastic scattering of ${}^6\text{Li}$ on ${}^{12}\text{C}$ (top panel), ${}^{24}\text{Mg}$ (middle panel), and ${}^{93}\text{Nb}$ (bottom panel). The Doppler reconstructed gamma is resolvable in the ${}^{12}\text{C}$ measurement but not in the ${}^{24}\text{Mg}$ other measurements. The purple and red line-shapes are the simulated response of the clover and tracking detectors, respectively. In the ${}^{12}\text{C}$ case, the purple line shape is fit to the data, and used to estimate the number of counts in the 3.56 MeV peak. The excitation energy was gated on the 15.1 MeV state in ${}^{12}\text{C}$ which has a $B(\text{GT}) \sim 1$. Assuming a comparable $B(\text{GT})$ in ${}^{24}\text{Mg}$ and ${}^{93}\text{Nb}$, over an equal-width range in excitation energy, and accounting for the change in the unit cross-section with mass, the purple and red line-shapes have been scaled to reproduce the expected number of isovector counts in the other two measurements. This clearly illustrates that resolving the ${}^6\text{Li}$ 3.56 MeV gamma becomes increasingly difficult in heavier systems where the isoscalar giant resonances remain strong. Decay from these resonances contribute a significant background in the region of the 3.56 MeV γ -ray from ${}^6\text{Li}$, and this background increases in magnitude with increasing nuclear mass.

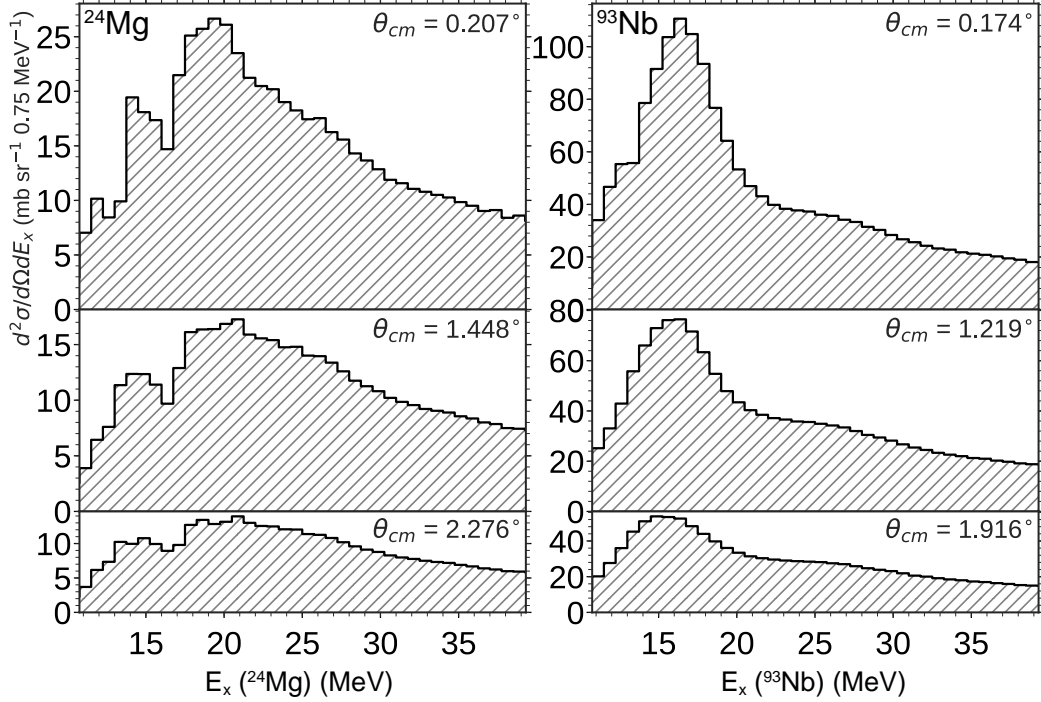


Figure 3.21: The differential cross sections for the $^{24}\text{Mg}(^6\text{Li}, ^6\text{Li}')$ and the $^{93}\text{Nb}(^6\text{Li}, ^6\text{Li}')$ singles measurements. The cross sections in both cases are dominated by isoscalar giant resonances which become larger with heavier mass systems.

middle panel shows the expected signal (of ~ 3700 counts) for the ^{24}Mg measurement using CAGRA. The isovector signal decreases significantly due to the exponential decrease of the GT unit cross-section as a function of mass. Unfortunately, at the same time the theoretical estimates of the 0° cross-section for 100% exhaustion of the isoscalar giant resonance energy-weighted sum-rule increases monotonically with nuclear mass as can be seen in Figure 3.22. These estimates are in line with what was observed in the ^{24}Mg and ^{93}Nb measurement. In Figure 3.21, the singles differential cross section for ^{24}Mg and ^{93}Nb are shown to both be larger than that seen for the ^{12}C measurement (Fig. 3.17). A larger overall cross-section due to the increase of the isoscalar strength with nuclear mass implies that a proportionally larger number of de-excitation gamma-rays from the decay of the isoscalar resonances will be observed. This is clearly the case for ^{93}Nb , where the background in the region of

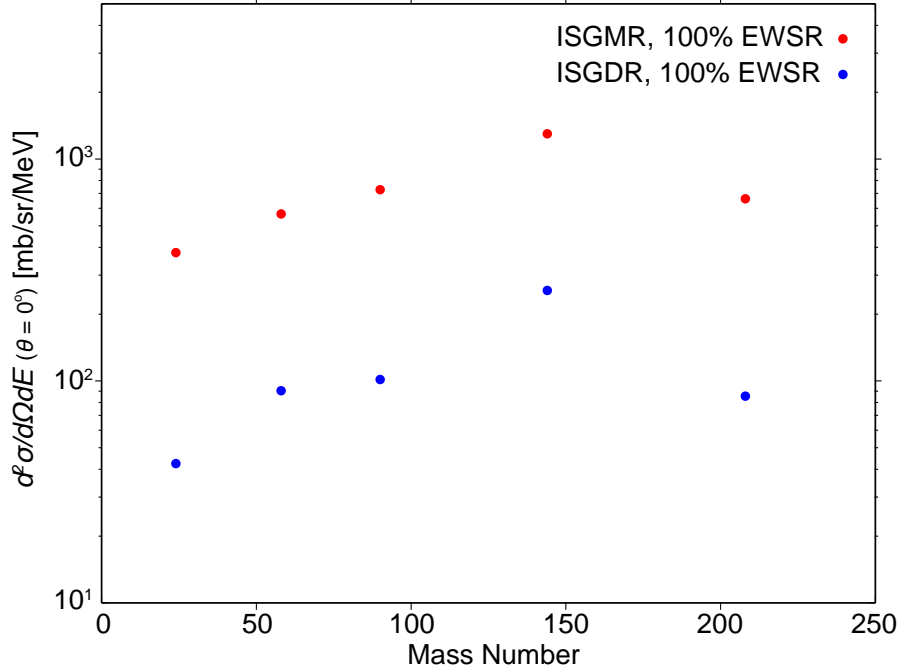


Figure 3.22: Mass dependence of the calculated zero-degree differential cross section for the isoscalar giant monopole and dipole resonances (IVGMR and IVGDR, respectively) corresponding to 100% exhaustion of the energy weighted sum-rule. These calculations illustrate the increase in the isoscalar cross-section as a function of nuclear mass number and were provided at the courtesy of Umesh Garg [139].

the 3.56 MeV gamma increased considerably relative to the gamma-background in ^{12}C ; see Figure 3.20, bottom panel. At the same time, the estimated Gamow-Teller unit cross-section for these nuclei decreases exponentially with mass, implying that the gamma-ray signal from ^6Li should become proportionally weaker with mass.

Unfortunately, this effect can only be partially mitigated by improved detector resolution. Using the above estimates for ^{24}Mg and ^{93}Nb with the available angular resolution of advanced HPGe tracking detectors, the red line in the bottom two panels of Figure 3.20 demonstrates that the achievable S/N would be barely sufficient for detection for ^{24}Mg and

impossible for ^{93}Nb . The background is simply too strong in the latter case.⁶ Therefore, unless there is a strong localization of isovector strength—in many discrete states—this large systematic background in the gamma spectrum makes identifying the increasingly weak isovector signal from the ^6Li 3.56 MeV γ -ray very challenging.

3.4 Conclusion

In this work, the ($^6\text{Li}, ^6\text{Li}'[T = 1, T_z = 0, J^\pi = 0^+, 3.56 \text{ MeV}]$) reaction probe has been shown to be capable of directly selecting the isovector spin-transfer transitions in ^{12}C via inelastic excitation. In this way the ^6Li reaction probe is the neutral-current analog to spin transfer charge-exchange reactions. The mass-dependent Gamow-Teller unit cross-section for ^6Li has been inferred from the data and configuration-interaction shell-model calculations. Hence, Gamow-Teller transition strength in the inelastic channel can now be extracted with this probe, and used to indirectly infer inelastic neutrino-nucleus scattering cross-sections.

However, it was found that in addition to providing an isovector spin-transfer tag in the form of the de-excitation 3.56 MeV γ -ray, ^6Li strongly excites the isoscalar giant resonances. Specifically, while the isovector cross-section decreases exponentially with mass number, no commensurate decrease in the isoscalar cross-section was observed. Thus, the resolvability of the isovector de-excitation γ -ray from ^6Li is extremely challenging for all but light nuclei due to a large high-energy γ -ray background from the decay of the isoscalar resonances. If the isoscalar and isovector responses were near-equivalent in cross section as a function of nuclear

⁶An additional effect introduced via the use of a tracking detector is that instead of discrete angular positions (e.g. the four angular positions covered by the clover detectors in this measurement, see Fig. 3.5), an approximately continuous coverage of emission angles is achieved. This has the result of smoothing out the background from gamma-rays emitted at rest (from the target). This would make a difference for the lighter nuclei, such as ^{24}Mg where the background in the sideband and photopeak regions are not smooth (see the middle panel of Fig. 3.20).

mass, this challenge would be overcome by utilizing modern HPGe tracking detectors which could provide a significant increase in the resolvability of the Doppler-boosted de-excitation gamma. As this is not the case for the (${}^6\text{Li}$, ${}^6\text{Li}'[T = 1, T_z = 0, J^\pi = 0^+, 3.56 \text{ MeV}]$) reaction, it remains a viable isovector spin-transfer probe only for light nuclei.

Chapter 4

Many-core algorithms for topologically divergent neural networks

Early research into artificial neural networks was inspired by the kinds of computational processing found in nature [140]. It was motivated by the computational paradox presented by the human brain: while comparatively inadequate in speed of serial calculations, the brain is capable of performing highly complex cognitive tasks with trivial effort compared to that of a modern computer [141]. It was suggested that the primary difference in the mode of processing performed by the brain is its distributed nature. Consisting of $\sim 10^{11}$ neurons, with a connectivity across $\sim 10^{14}$ synapses [141], the computational power of the brain appears to come from its massively parallel organization and execution.

Every neuron can be connected to many other neurons, can undergo activation, and can induce activations in neurons to which it is connected. These fundamental components comprise the core structure and operations within biological neural systems, as well as artificial neural networks (ANNs). Shown in Figure 4.1 are the typical components of an artificial neural network. The basic components of a neural network are inbound and outbound connections, a node, and its corresponding activation function.

Artificial neural-network components

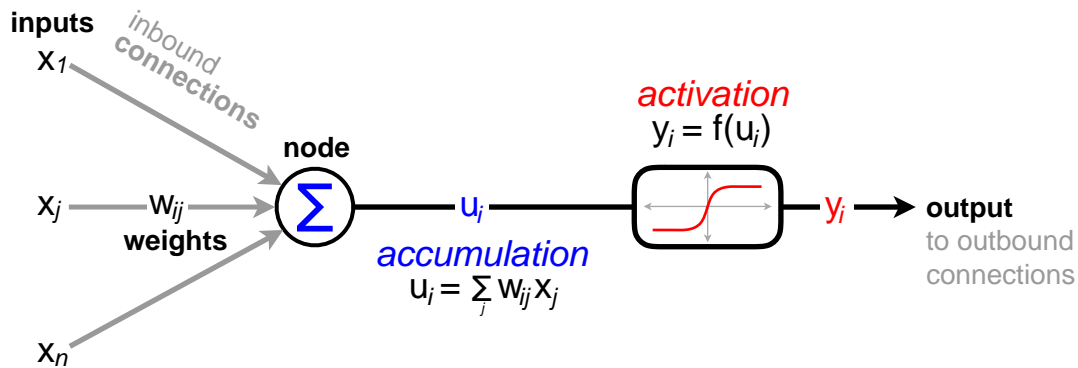


Figure 4.1: The basic components an artificial neural network. Each node (shown as the circle in the figure) accumulates inputs modulated by the weights of its inbound connections. After all of the inbound connections have been accumulated into the node, a non-linear activation function, such as a logistic sigmoid, transforms the nodes value. The transformed node value is then used as an output along outbound connections to other nodes in the network.

Input values (x_j) are fed forward via *inbound connections*, shown as grey arrows on the left of Fig. 4.1, which modulate the inbound signal by connection weight factors (w_{ij}). These connection weights represent the strength of each connection and are the principle degrees of freedom in a neural network. By adjusting these weights, a neural network can be trained to yield the desired response given the inputs.

The product of the inputs and the weights are accumulated into a floating point number known as the *node*. When all of the inbound connections have been fed into the node, a non-linear function is applied to the node's value, and it then can be used as the source for any *outbound connections*, see the right side of Fig. 4.1. This non-linear transformation is a unique characteristic of the ANN neuron and is analogous to the activation potential in biological systems: the capability of a neuron to fire (or not) given its accumulated input signal. In neural networks, this function is referred to as the *activation function* and is often chosen as a smoothly varying function that can represent both final states of the node (active or inactive)—for example, a logistic sigmoid [142]. Finally, the activated node value (y_i in

the figure) is then output via the outbound connections which feed into other nodes.

Together, the above described neural-network components form a structure resembling a biological neuron. Neural networks are formed by combining many such neurons together into a larger network. Panels (a) and (b) of Figure 4.2 detail two simple neural networks, where each circle is a network node, and each arrow between nodes is a network connection. Nodes with no inbound connections are known as input nodes (left most set of nodes in Fig. 4.2), and they are loaded with the user input data, and output nodes are nodes with no outbound connections. The output of a neural network are the values of its output nodes. The network shown in (a) is representative of the kinds of neural networks found in modern shallow and deep learning applications, and is known as a hidden-layer neural network or a multi-layer perceptron.

It has been shown [143] that a neural network with a single hidden layer (similar to network (a) in Fig. 4.2) can approximate any function given arbitrarily many nodes in the hidden layer. It is because of this capability that neural networks have been applied so successfully to diverse applications. Furthermore, the use of additional hidden layers, as in *deep neural networks*, increases the non-linearity and can capture higher-level abstractions of the data more easily [144]. However, while these points have been known for the past decades, it wasn't until the advent of modern computational capabilities and enormous datasets, known as "big data", that it would become possible to train neural networks with such large numbers of degrees of freedom. As more hidden nodes and hidden layers are added, more free parameters in the form of connection weights are introduced.

Neuroevolution, on the other hand, is an approach that has developed in parallel to complex layered neural networks, and has instead drawn on biological inspiration to describe the complexification process of neural networks [26]. In addition to modeling artificial neural

network behavior from the way in which complex systems of neurons operate, neuroevolution seeks to model how these systems are formed. It does so by applying evolutionary algorithms (EAs) to large populations of neural networks in order to search for the optimal network structure and hyperparameters [26]. Similar to biological evolution, these networks compete for limited resources and in each generation, only the best performing neural networks survive. The concept of limited resources in neuroevolution arises from the limited compute cycles available and is often represented by penalizing networks which evolve large structures that do not benefit the overall performance of the network. In this way, populations of neural networks with minimally complex structure, evolve new nodes and connectivity only if the structural changes represent innovations that improve overall performance. This concept strictly contrasts that of complex layered neural networks. With hidden-layer neural networks, few *a priori* constraints are placed on the network size. Even though the number of connection weights (degrees of freedom) in these models are large, enormous datasets are often available which can be used to train these weights, albeit at large computational cost.

Unfortunately, in many scientific domains, data sizes are not comparable to what is collected in industrial big data applications, and so the utility of arbitrary network complexification is limited. The method of evolving neural networks through augmenting topologies [145] on the other hand, seeks to find the best performing neural network by minimizing the search space and only increasing the network complexity when doing so improves the neural network. For this reason, neuroevolution is able to generate neural networks with complexities that scale with the size of the training data, making it generally applicable to scientific applications, regardless of data size.

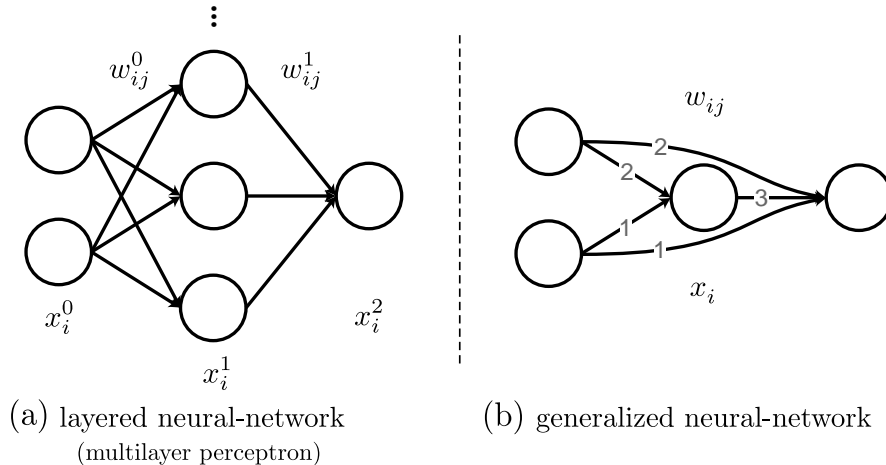


Figure 4.2: (a) A common feedforward neural-network structure with a single hidden layer. x_i^0 , x_i^1 , and x_i^2 correspond to the input, hidden and output layers respectively, while $w_{ij}^0, 1$ refer to the connection weight matrices between two layers. (b) An unstructured neural network in which the connections are not constrained to specific layers. Such network structure is common in neuroevolution populations. Each connection in (b) is labeled with an integer indicating the lock-free set in which it can be evaluated. See section 4.3.1 for details.

4.1 Applications in physics

While neural networks have been employed in a variety of physics domains for the past few decades [146], their utility has been increasingly significant in experimental high-energy [147] and neutrino [148] physics. In these physics applications, neural networks have almost exclusively been employed as classification tools as a means to separate signal and background events. The most commonly employed classification techniques in these fields are neural networks with a single hidden layer (shallow ANNs), boosted decision trees, and as of the past few years, deep neural networks. Until the work of [147], physicists reluctantly accepted the limitations of shallow neural networks, and guided the networks by hand toward better event selection by manually constructing nonlinear input feature combinations that helped the training processes. However, with the availability of large datasets in high energy physics, Baldi *et al.* [147] showed that recent advances in deep neural networks lift these

limitations by automatically discovering nonlinear feature combinations that provide better event discrimination than shallow neural networks even with manually constructed input combinations.

The ability of deep neural networks to circumvent the need for manual data preprocessing comes from the large number of hidden layers, and the correspondingly large available datasets. Without sufficient data, however, the feasibility of deep learning is limited. On the other hand, as discussed previously, neuroevolution generates neural networks with complexities that scale with the size of the training data, making it more generally applicable. In this way, complicated data preprocessing can be evolved according to the constraints of the data, regardless of data size. Indeed, neuroevolution has been previously used in this way to provide high precision selection of dilepton events for the measurement of the top-quark mass at CDF [149].

Recently, researchers involved with the NEXT neutrino physics experiments, which employ high pressure xenon time projection chambers (TPCs), have shown that deep convolutional neural networks, presently the state-of-the-art deep machine learning technique for the analysis of image data, can be 60% more efficient at the selection of neutrinoless double beta decay events as compared to traditional techniques [150]. Because TPCs produce volumetric images of particle tracks within the detector, convolutional neural networks are effective at event selection based on the difference in tracks for signal and background events. However, as neural networks become increasingly complex, as is the case for convolutional networks, they are endowed with additional hyperparameters that increase the burden of tuning that must occur prior to training [151].

Very recently neuroevolution techniques have been employed to evolve minimally complex convolutional neural networks [24]. Similarly, Fernando *et al.* [25] have shown that by

using neuroevolution to evolve network topologies, the resulting network had two orders of magnitude fewer free parameters and was able to achieve the same accuracy as a comparable fully connected convolutional network. With far fewer connections, the evolved convolutional networks have fewer free parameters to be learned, and are therefore able to be trained with significantly smaller datasets as compared to their fully connected counterparts. Therefore, neuroevolution extends the utility of deep-learning methods to application domains in which the datasets are smaller in magnitude than what is required for traditional deep neural networks.

For this reason, the experimental nuclear astrophysics program discussed in chapters 2 and 3 may significantly benefit from neuroevolution since the available training datasets are likely to be of intermediate size. In chapter 5, a new experimental technique in which a TPC is utilized to image recoil particle tracks after they undergo β^+ charge-exchange reactions will be discussed. Similar to the NEXT experiment previously described, convolutional neural networks may be capable of efficient event selection for TPC-based charge-exchange experiments in inverse kinematics. By utilizing neuroevolution and the methods described in this work, even though the available training data will be smaller than in experimental high energy physics applications, the evolved networks will be tuned in structure to the available data and are therefore likely to have comparable performance.¹

¹It should also be noted that in experimental physics, a viable option for the application of deep learning techniques is to utilize physics simulations to generate the required training data. In this case, the performance of networks trained on simulated data will depend significantly on the accuracy of the simulated data.

4.2 Network Structures & Evaluation

One hallmark of neuroevolution is its ability to develop populations of structurally diverse neural networks, which do not necessarily have strict layer boundaries. For example Fig. 4.2b demonstrates a neural network that could evolve, wherein the concept of a hidden-layer no longer applies due to the connections from the two input nodes directly to the output node. That said, this functionality can be reproduced in a hidden-layer neural network (such as panel (a) in the same figure) if the connection weights are tuned correctly. While networks (a) and (b) in Fig. 4.2 are capable of producing the same network output, given the larger number of nodes and connections involved, the hidden-layer network (a) would be more computationally expensive to evaluate. This is easily seen when considering the feedforward evaluation pattern for hidden-layer neural networks which can be written as [152],

$$\mathbf{x}^{(1)} = \sigma \left(W^{(0)} \mathbf{x}^{(0)} + \mathbf{b}^{(0)} \right), \quad (4.1)$$

$$\mathbf{x}^{(2)} = \sigma \left(W^{(1)} \mathbf{x}^{(1)} + \mathbf{b}^{(1)} \right). \quad (4.2)$$

Here, evaluation is performed by feeding forward the network inputs, $\mathbf{x}^{(0)}$ into consecutive layers by multiplication of the connection weight matrix, $W^{(0)}$, to this input vector, the addition of a bias vector, $\mathbf{b}^{(0)}$, and the activation of the result. σ is the activation function and is often chosen to be a smooth function that is bounded between two values, one of which represents a neuron firing (activated) and the other which represents quiescence (not active). The result of Eq. 4.1 are the values of the nodes in the next layer, $\mathbf{x}^{(1)}$, which then become the input vector for the next feedforward iteration, shown in Eq. 4.2. This process is repeated until the inputs have been fed through to the final output layer. Thus, feedforward

evaluation of layered neural networks is simply the repeated application of matrix-vector multiplication, and so it is evident that the more nodes and connections a network has, the more floating point operations (FLOPs) will be required.

While network (a) in Figure 4.2 requires more total FLOPs than network (b), the method of evaluation described by Eq. 4.1 is highly parallelizable as it is simply repeated matrix operations [153]. Neural networks which do not conform to the layered description, on the other hand, cannot be described by matrix multiplication. Principally, this is because the calculation of the neural-network output is no longer divisible into a series of linear computations. Instead, as for network (b), the evaluation must follow a graph traversal in which connections are applied consecutively, and node activations occur for each node once all inputs to the node have been computed.

As mentioned in the beginning of this section, the novelty of neuroevolution is its capability to produce highly topologically diverse neural network structures, which can reproduce inherent symmetries in the underlying datasets [154]. However, such diversity in the neural network population implies that the computational graphs of each neural network can be extremely divergent. At the same time, because the search capability of the evolutionary algorithm scales with the population size, using as many networks as computationally feasible is ideal. If population sizes are in the tens to hundreds of thousands, the evaluation complexity warrants the use of modern multi- and many-core compute architectures. However, the divergence that arises in evaluating neural networks of diverse structure, has so far prevented the development of generalized many-core algorithms for neuroevolution which scale well with the population size. This is because many-core architectures, such as general purpose graphics processing units (GPGPUs), employ single-instruction-multiple-data (SIMD) vector processors. These kinds of processors perform optimally when execution branching is

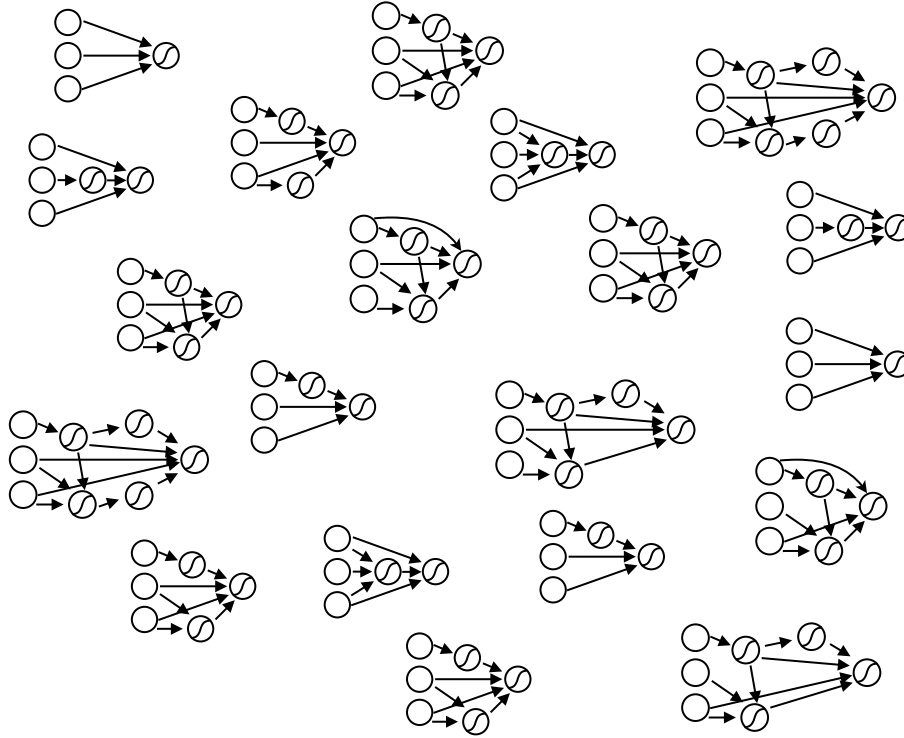


Figure 4.3: An illustration of the structural divergence than can exist in populations of neural networks evolved via neuroevolution. In this case, each network has a fixed number of input and output nodes (3 and 1, respectively).

minimal. Unfortunately, the parallel evaluation of neural networks with differing structures has the opposite effect, execution branching is enhanced.

Presented in this work is a novel many-core algorithm for the concurrent evaluation of entire populations of topologically-divergent neural networks. These algorithms represent the first general-purpose mapping of large numbers (100k+) of heterogeneous neural networks to many-core architectures.² By harnessing modern many-core processors, this work aims to enable neuroevolution to be a more competitive player in the modern machine learning ecosystem.

²An open source implementation of the described methods are freely available online at <http://www.github.com/csullivan/Entendre>.

4.3 Directed acyclic graph concurrency

An example of the structural diversity within populations of neural networks is shown in Figure 4.3, where each network has exactly 3 input nodes and 1 output node. The hidden node structure of the networks is then evolved during many generations of neuroevolution. While all of the networks in the figure have standard connections which feed forward, neuroevolution can also evolve recurrent connections.³ This is worth noting as the algorithm proposed in this section performs equally well with recurrent neural networks.

The naive feedforward evaluation of a network population, such as that shown in the figure, would be to distribute each network to a different processor or thread. For multi-core processors this is not a necessarily bad approach, particularly if the networks involved are large in size and can take advantage of the heterogeneous cache-memory layouts of modern multi-core processors. However, if the population size is much larger than the number of available processors, or the networks themselves are relatively small, cache-coherence is likely unattainable. This is because a population of neural networks is essentially an array-of-structures (AoS) organization of data, and so consecutive neural networks are loaded from RAM neglecting any benefits of hierarchical memory.

For many-core SIMD coprocessors, distributing neural networks across threads has far worse performance. There are three principal considerations to be made in SIMD parallelism by distributing neural networks across threads:

1. Branch divergence from differing neural network topologies (a result of neuroevolution as previously discussed).

³Recurrent connections in a neural network are connections which form a directed cycle in the network. However, instead of actually producing a cycle, they function by acting as *external* inputs into the network, which pass the value of a node from the previous feedforward evaluation into the destination node of the recurrent connection in the current evaluation. In this way, recurrent connections act as a kind of neural network memory.

2. Lack of memory access coalescing requiring each network to be loaded from device RAM (DRAM).⁴
3. The input data and output node values must be communicated from the Host (CPU) to the Device (GPU) for each neural network separately.

The three items above can be summarized as a lack of optimization in instruction execution, memory access, and communication, respectively.

Instead of seeking to parallelize over individual neural networks, this work establishes a sorting algorithm that organizes the evaluation of many neural networks into a problem of parallelism over the directed acyclic dependency graphs of each neural network. By reformulating the problem in this way, optimizations for items 1–3 are naturally attained: instruction branching is removed, memory accesses are coalesced, and the communication between the host and device is minimized.

4.3.1 Topological connection sort

In order to avoid hierarchical data structures, which typically rely on many heap-allocated blocks of memory and thereby reduce the utility of memory caching, the network structure is stored as flat arrays of the connection components⁵. Here, each connection consists of the index of the origin node, the destination node, and the weight of the connection. Using an array of floating point numbers to store the values of the nodes, or their partially computed intermediate values, each connection then represents a single uniform action to be applied

⁴Memory access coalescing, or the lack thereof, is similar to cache-coherence on a CPU. Whereas during a memory load for a CPU, a block of memory (ABC) is brought from RAM and stored into the CPU cache, for a GPU, a memory request from DRAM coalesces a cycle of memory to each thread, so that threads 1, 2, & 3 receive floats A, B & C. A lack of memory coalescing indicates that data utilized by threads in the GPU are not spatially colocated, and so each thread must make individual memory loads [155].

⁵A structure of arrays (SoA) memory layout as opposed to an AoS layout

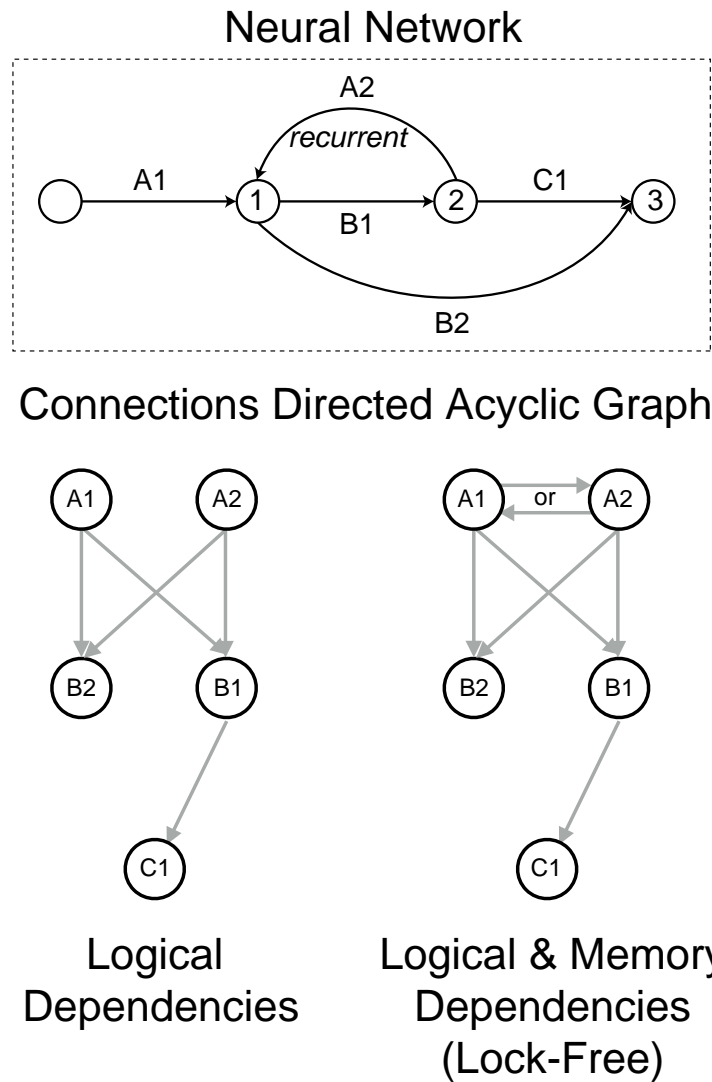


Figure 4.4: An example neural network and two directed acyclic dependency graphs for the evaluation of the neural network's connections. The left dependency graph includes only *logical* dependencies whereas the graph on the right includes both *logical & memory* dependencies. Each circle in the dependency graphs represent connections in the top neural network figure. The arrows in the two dependency graphs indicate the dependency relationship between the connections. For example, the arrow between A1 and B1 indicates that connection A1 must be evaluated prior to B1. By inspecting the neural network, this relationship is evident as connection B1 relies on node 1, which in turn relies on connection A1 (as well as other connections).

on the array of nodes. In this way, the neural network is organized by its connections instead of via its nodes.

The key algorithmic insight in the proposed method is the sorting of neural network connections into evaluable sets based on their dependencies. The directed acyclic graph (DAG) for an example neural network's connections is shown in Figure 4.4. Every circle in the DAG represents a connection in the neural network, and every arrow in the DAG implies a dependency relationship. For example $J \rightarrow K$ implies that K depends on J , and so if these represent connections it implies that connection J must be evaluated first in the neural network. These relationships arise from the fact that connections in a neural network have direct and transitive dependencies—connections earlier in the neural network must be evaluated before those that come later. For example, $A1$ must be evaluated before $B1$ in the example neural network shown on the top of panel Figure 4.4. Dependencies of this type can be referred to as *logical dependencies*. *Memory dependencies* can also exist if the employed algorithm is to be lock-free.⁶ These type of dependencies occur when two connections which are not logically dependent, affect the same destination node.

The algorithm described in this work topologically sorts connections into ordered sets that respect both of these dependencies. That is, within each set, all constituent connections have different destination nodes (lock-free) and are logically independent. If the algorithm need not be lock-free, the adherence to connection memory dependencies can be relaxed. The two graphs in Figure 4.4 illustrate the relationships between connections in an example neural network when only logical dependencies are considered (left) as well as when logical-and-memory dependencies are considered (right). Determining the order of connection evaluation

⁶Lock-free in this context implies that no memory synchronization or exclusions are required, such that no two threads will attempt to write to the same memory space simultaneously.

```

1 for(i=0; i<num_connections; i++) {
2   for(j=i+1; j<num_connections; j++) {
3     a = connections[i];
4     b = connections[j];
5     switch(compare_connections(a,b)) {
6       case a > b:
7         a.num_dependencies++;
8         break;
9
10      case a < b:
11        b.num_dependencies++;
12        break;
13
14      // (a,b) not adjacent
15      case Unknown:
16        break;
17    }
18  }
19 }
20
21 topological_sort(connections);

```

Figure 4.5: Prototype of sorting connections into concurrent lock-free sets. For n connections, scales as $\mathcal{O}(n^2)$.

of the neural network is then straightforward from these dependency graphs, and concurrency is immediately evident. Consider the left graph in Fig. 4.4. Any connection (circle in the DAGs) which has no inbound dependencies (shown as the grey arrows), can be evaluated immediately. Thus, one can see that connections A1 and A2 can be evaluated in parallel at the first step. The next step is to remove A1 and A2 from the dependency graph, and to again search for connections which now have no inbound dependencies. After A1 and A2 are evaluated, we see from the DAG that connections B1 and B2 have no dependencies, and so are able to be evaluated next and in parallel. Finally connection C1 can be evaluated. This sorting technique is known as a topological sort of a directed acyclic graph and is often used in determining the order of tasks [156].

Algorithmically, the dependencies each connection has is determined using the comparator scheme shown in Table 4.1. With this comparison, if two connections are adjacent and

Table 4.1: Neural network connection dependency comparator

Type	Condition	Dependency
Connection pair (a,b) with differing output nodes		
a recurrent	a.origin = b.destination	a < b
b recurrent	b.origin = a.destination	a > b
a normal	a.destination = b.origin	a < b
b normal	b.destination = a.origin	a > b
Connection pair (a,b) with the same output node		
a self-recurrent	a.origin = a.destination	a < b
b self-recurrent	b.origin = b.destination	a > b
arbitrary choice	a.origin < b.origin	a < b
arbitrary choice	b.origin < a.origin	a > b
a & b not adjacent	-	unknown

The neural network connection dependency comparator. There are three subsections in the above, when connections a and b (1) are adjacent and have different output nodes, (2) are adjacent and have the same output nodes, and (3) are not adjacent. If the algorithm need not be lock-free (does not respect memory dependencies) then the second subsection (connections with the same output node) can be dropped and the rules of the first subsection are used exclusively for adjacent connections. Each connection has an origin and destination node, which are what is referred to in the Condition column. The less-than and greater-than symbols in the Dependency column imply the ordering of the two connections; if $b > a$, then the evaluation of connection a must come prior to b . In the case of an unknown relationship between non-adjacent connections, transitive relationships will enforce an ordering if one exists. This comparator handles both normal and recurrent connections.

one connection depends on the other, the dependent connection's number of dependencies is incremented. This comparator can then be applied to any neural network regardless of its structure and a topological sort, as described previously, can determine the sets of concurrently evaluatable connections. An example implementation of this is shown in Figure 4.5.

4.3.2 Neural network operations

The ordering of connections into concurrently evaluatable sets, as described in the previous section, provides the scaffolding off which the rest of the neural network operations are built. Fundamentally, three operations are required in the feedforward evaluation of an arbitrary neural network,

1. **Apply connection:** The application of a connection A1 from node 1 to node 2: $x_2 = x_2 + w_{A1} \cdot x_1$, where x_i is the floating point value of node i , and w_{A1} is the weight of the connection A1.
2. **Zero/Reset node:** Setting the memory address of a node's floating point value to zero, $x_i = 0$.
3. **Activate node:** Applying the activation function to a node's value, $x_i = \sigma(x_i)$.

In the previous section, connections within a neural network were grouped into ordered sets, such that the application of the connections within each set could be performed simultaneously. In this way, parallelism over the directed acyclic dependency graph of a neural network boils down to the bulk synchronous evaluation of operations 1–3 above on different connections and nodes within the network. Using the ordered sets of connections, the zeroing and activation of nodes can be deduced from the following observation: given the

above neural network operations, a strict order-of-operations can be defined such that the neural network's full directed acyclic dependency graph can be established. Specifically this operation order is,

Activate origin nodes < Zero destination nodes < Apply connections.

Therefore, given a set of connections which are to be applied, any origin node that has not been previously fed forward must be activated, any destination node which has not yet been fed into must be zeroed/reset, and then all connections in the set can be applied.

By building the dependency graph from the connections DAG previously discussed, and by employing the above order of operations, this algorithm guarantees that at every step, the performed operations will be homogeneous. That is, many nodes will be activated concurrently, then many nodes will be zeroed concurrently, and finally many connections will be applied concurrently. In this way the evaluation of a neural network is factored into steps that can be easily mapped to SIMD processors. This will be discussed in detail in section 4.3.3.

4.3.2.1 Neural network node lifecycle

While the order of operations proposed captures the general method requirements of the feed forward evaluation of arbitrary neural networks, it misses a few subtleties that are apparent when considering the lifecycle of a node in a neural network.

Thus, let us consider the lifecycle of a single node in a network. At the start of neural network evaluation, a node holds its activated value as determined in the previous evaluation of that network. The first step that must be taken is that all recurrent connections must be applied which use this node's value as an origin. This is because a recurrent connection

is meant to act as a type of memory, feeding information from previous network evaluation into the current evaluation.

Next, the node must be zeroed out. Following this, there is a phase when the node is used as a destination, with its value being the weighted cumulative sum of all incoming connections that have been applied. Once all connections inbound to this node have been applied, the activation function transforms the node's value. Then, the node can be used as an origin for normal connections, and finally, the output value is left untouched, so that it can be used for any recurrent connections in the next evaluation.

These steps are fundamentally what impose the ordering conditions described in the previous section,

- The zero/reset must occur after the last use of the node as an origin of a recurrent connection, and before the first use of the node as a destination.
- The activation function must be applied after the last use of the node as a destination, and before the first use of the node as an origin of a normal connection.

Thus, these actions are performed between the evaluation of each set of connections.

Together with the connection ordering described in section 4.3.1, we arrive at a general distribution of tasks which follow the basic life cycle of a node and which are constrained by the parallelism of the evaluatable connection sets.

4.3.3 Generalized concurrent neural network evaluation

By applying the topological sort of network connections and enforcing the order of operations described above, the full neural network evaluation graph can be built. Figure 4.6 shows the directed acyclic dependency graphs for two neural networks with different structures.

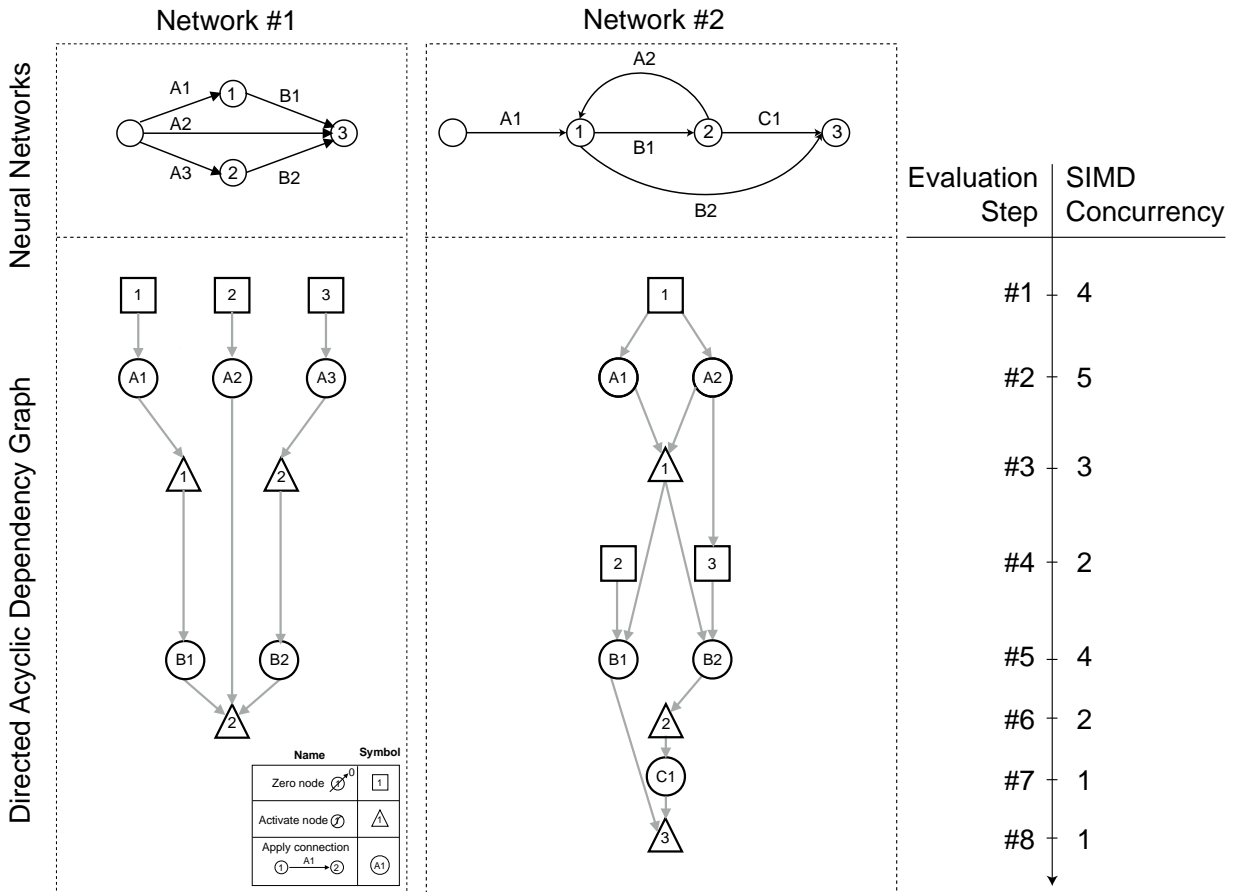


Figure 4.6: The full directed acyclic dependency graphs for two structurally different neural networks. The different symbols in the graph, squares, circles, and triangles, represent the three neural network operations: zero-node, apply-connection, and activate-node, respectively. Even though the two networks have very different structure, the algorithm proposed in this work organizes the network evaluation graphs into evaluations steps that are component-wise parallel. On the right of the figure, each evaluation step is shown with the number of SIMD operations that can be performed simultaneously.

The neural network label network 2 in the figure is the same network shown in Fig. 4.4. However, instead of just showing the DAG for the application of connections, it includes the other operations as well: squares represent the zero-node operation, circles represent the apply-connection operation, and triangles represent the activate-node operation; see the key in Fig. 4.6 for more details.

Factoring the neural network evaluation into these component operations, the individual structure of different neural networks is no longer a consideration. Each network has some number of nodes which must be zeroed and activated, as well as some number of connections that must be applied. Starting at the top of the DAGs shown in Figure 4.6, the first step in evaluating both networks 1 and 2 is to zero out four nodes (see the axis to the right of both networks). Therefore, in this first step, an operation concurrency of four is achieved. In the second step of evaluation, five connections must be applied across the two separate networks. This process continues until all evaluation steps in the shown DAGs have been performed, at which point the inputs have been fully fed through both networks, and evaluation is complete.

Thus, the algorithms presented here are completely agnostic to the macroscopic structure of the constituent neural networks. At the same time, these algorithms order the tasks to be performed into homogeneous sets of operations which map very well to SIMD processors. This effectively resolves the instruction branching problem described in section 4.3. Furthermore, as can be seen in Fig. 4.6, this algorithm will scale with the neural network population size. Since instruction branching is removed, the more networks that are utilized, the greater the concurrency at each evaluation step. This indicates that the performance gain should

scale at least linearly with the number of neural networks.⁷

4.4 Composite population evaluation

While the DAG based algorithms described in the previous section solves the problem of evaluating structurally diverse neural networks on SIMD-based processors, it doesn't alleviate the lack of optimization in memory access and Host-Device communication described in section 4.3. In this section, both of these latter issues are resolved via a simple reordering of the memory layout for the neural network population.

Instead of storing each network individually, a refactoring of a population of N networks into a single composite network, consisting internally of all the nodes and connections of the sub-networks, is employed. In this way, the resulting neural network will have at minimum N connections per evaluation step that can be processed concurrently using the evaluation algorithm described in section 4.3.3. An example of two such refactorizations are demonstrated in Figure 4.7.

The construction of the composite net is straightforward. First, all network input nodes are added, then all output nodes, and finally all hidden nodes. Following this, each connection of each sub-network is reindexed according to the position of its nodes in the larger set of nodes of all networks in the population. After all connections are added, the connection sort described in section 4.3.1 and detailed in Figure 4.5 is applied to each subset of connections in the composite neural network. As these populations can grow quite large, it is computationally most efficient to sort based on these unconnected sub-structures (the

⁷The performance scaling with the neural-network population size can be less than linear if the population contains a subset of outlier networks which have much larger network topologies than the majority of the population. In this case, the majority of networks will finish their final step of evaluation while the evaluation of the subset will only be partially completed. Thus, in the remaining steps of evaluation for the outlier networks, the concurrency will be dramatically reduced.

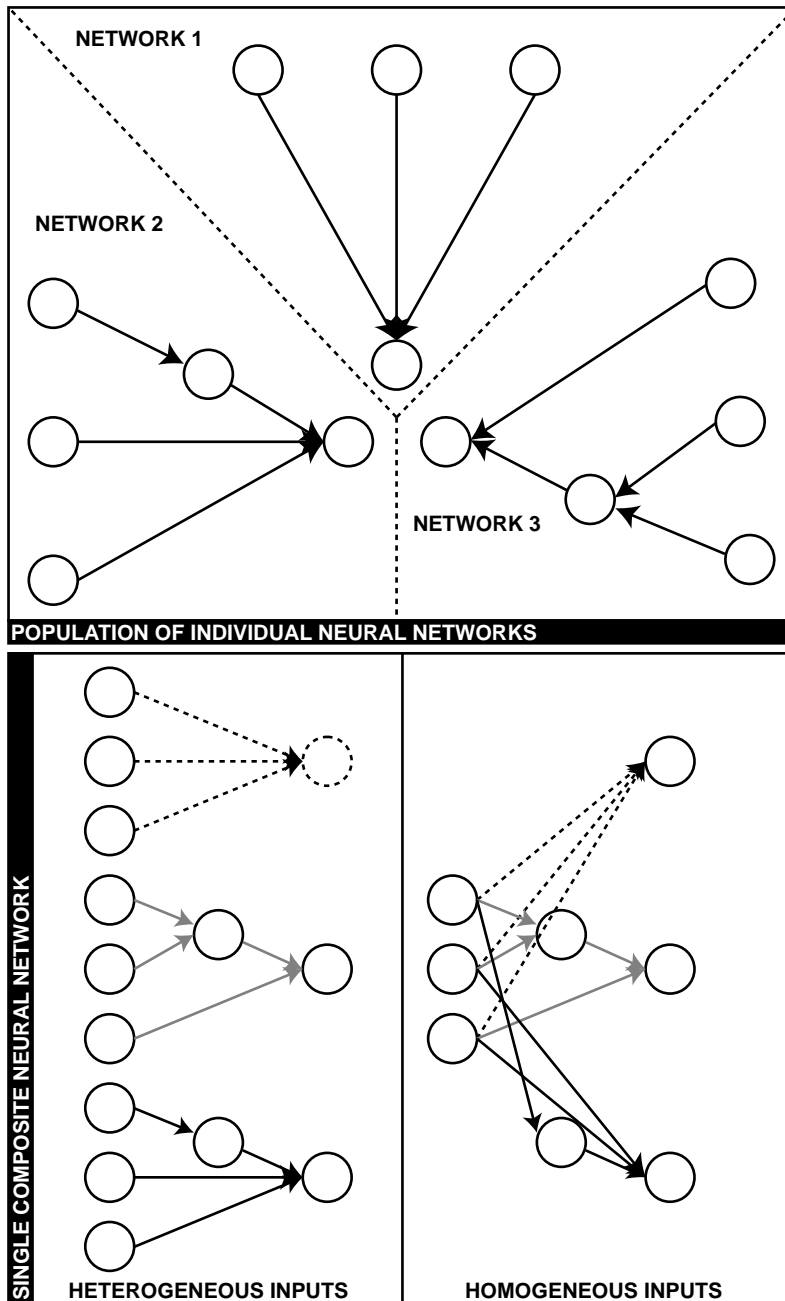


Figure 4.7: Top panel: A representative example population of neural networks consisting of three members. In classic neuroevolution simulations, each of these neural networks are separately evaluated, and the correctness of their outputs is used to judge their fitness. Bottom panel: The same population as in the top panel, but constructed as nodes and connections of a single composite neural network. On the left, the resulting composite network in which each of the constituting sub-networks requires heterogeneous inputs for evaluation. On the right, a composite network in which each of the sub-networks will process the same inputs.

individual networks) instead of the composite network, as the sorting algorithm shown above scales as $\mathcal{O}(N^2)$ with respect to the number of connections. Finally, the connections of the composite network are globally sorted according to their evaluation set index. Following this procedure then guarantees that connections which can be evaluated together are colocated in contiguous memory space. This then allows the origin and destination node indices and connection weights to be perfectly coalesced from DRAM to the individual threads. The resulting population-level composite network is then ready to be evaluated on a GPU or other SIMD coprocessor.

In constructing a composite network from a population of neural networks, an additional optimization that can be made is to refactor all of the input nodes into a single set of inputs. This can occur if each network in the population will be evaluated given homogeneous sets of inputs. If on the other hand, each network will receive heterogeneous inputs, this refactoring cannot be performed. In the bottom panel of Figure 4.7 both possible composite networks are shown, one in which all inputs are explicitly specified (heterogeneous inputs), and one in which a single set of input nodes are fed to the rest of the sub-networks (homogeneous inputs).

In both cases, to evaluate the resulting neural network, a single memory transfer of the input node array (consisting of nodes for all the networks) is copied to the device, the evaluation proceeds concurrently, and finally a single copy of the outputs (again in contiguous memory) finishes the calculation. This is possible because, the input and output nodes of all the networks are positioned in continuous memory space.

Since this network is quite large and has many unconnected regions, the DAG-based algorithm described previously takes maximal advantage of the available component-wise concurrency in the evaluation. Furthermore, the connection weights and node indices are

memory access coalesced for each connection, and the interaction between the host and device occurs only twice (on the boundaries of the evaluation), minimizing any possible communication contention. In summary, by combining the DAG-based concurrent evaluation described in section 4.3.3 with the composite organization of a population of neural networks into a single composite network, instruction execution, memory access, and communication, are fully optimized for execution on many-core processors.

4.5 CUDA implementation

The DAG-based connection sort and construction of the composite neural network described in the previous sections are performed on the host CPU, after which the network connections and nodes are copied to the many-core device for evaluation. The network evaluation performance is benchmarked using the compute unified device architecture (CUDA) [157]. The implemented CUDA kernels can be found in Figure 4.8. There are a total of three kernels for the three necessary actions to be performed: resetting a node to zero, activating a node, and applying a network connection.

As a result of the presorting of operations on the host, the CUDA kernels are extremely simple, bringing the possibility of (thread) branch divergence to an absolute minimum. The only possible divergence that exists is seen on line 43 of Figure 4.8 in which a self-recurrent connection⁸ is handled as a special case. In the case of neural networks with no self-recurrent connections, this algorithm is GPU thread divergence free.

⁸A self-recurrent connection is a connection whose origin node is also its destination node. These connections function as memory in the neural network, returning the output the node from the previous network evaluation.

```

1
2 __global__
3 void device_clear_nodes (uint32_t* list , float* nodes, uint32_t n)
4 {
5     int i = threadIdx.x + blockIdx.x * blockDim.x;
6     if (i<n) {
7         nodes[list[i]] = 0;
8     }
9 }
10
11 __global__
12 void device_activate_nodes (uint32_t* list, float* nodes, uint32_t n)
13 {
14     int i = threadIdx.x + blockIdx.x * blockDim.x;
15     if (i<n) {
16         nodes[list[i]] =
17         device_activate(nodes[list[i]]);
18     }
19 }
20
21 __global__
22 void device_apply_connections (
23     float*    node
24     ,
25     uint32_t* origin
26     ,
27     uint32_t* dest
28     ,
29     float*    weight
30     ,
31     uint32_t  n
32     )
33 {
34     int i = threadIdx.x + blockIdx.x * blockDim.x;
35     if (i<n) {
36         auto& conn_origin = origin[i];
37         auto& conn_dest = dest[i];
38         auto& conn_weight = weight[i];
39         if(conn_origin == conn_dest) { // Special case: self-recurrent node
40             node[conn_origin] *= conn_weight;
41         } else {
42             node[conn_dest] += conn_weight*node[conn_origin];
43         }
44     }
45 }

```

Figure 4.8: NVIDIA CUDA kernels for the proposed concurrent neural network evaluation.

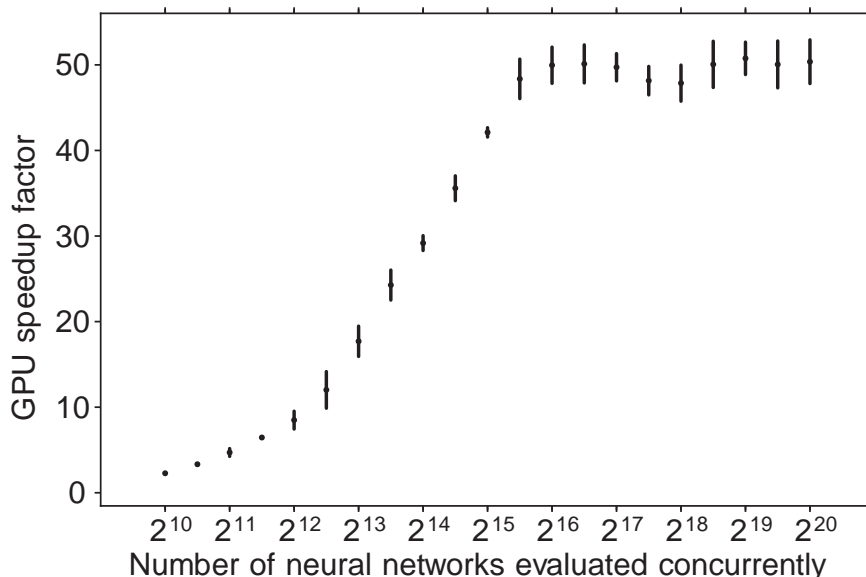


Figure 4.9: GPU speed up factor when evaluating a population of N evolved neural networks concurrently. The ratio of time taken for the sequential evaluation of each network on a single CPU thread to the time for transferring inputs to the device, evaluation on the GPU, and transferring the outputs back to the host. With a population of approximately 65k networks, a performance boost of 50x relative to the serial implementation is observed.

4.5.1 Performance results

In the performance tests that follow, the primary machine on which these algorithms were tested was equipped with a 3800MHz i7-2600 CPU, along with a NVIDIA GTX 1070 GPU. In addition, these results were also verified on a system with a 2400MHz E5-2680v4 CPU and a NVIDIA Tesla k80 GPU. The results reported are those for the former system, as the results from the later system were found to be comparable.

To illustrate the performance of the methods described in this work, a population of neural networks was evolved according to the Neuroevolution of Augmenting Topologies (NEAT) technique. NEAT is an evolutionary algorithm (EA) introduced by Stanley and Miikkulainen [145]. The principle components of NEAT are (1) a method of crossover (mating) to efficiently combine network structures into resulting child networks, (2) the introduction of

speciation to protect new topological innovations that arise, and (3) incrementally growing networks from minimal structure, allowing the networks that form to both optimize and complexify solutions simultaneously [145].

Using NEAT, a populations of neural networks of arbitrary size were evolved. Each of these populations was seeded with a topologically minimal network: the seed network had three input nodes, and one output node. Initially, the three input nodes (two inputs for the XOR plus a bias/offset node) were connected directly to the output node making for a total of 3 connections. These networks were then evolved to solve the exclusive-or operation (XOR).

The simplest solution to the XOR operation is a network of only 5 nodes and 7 connections, which is quite quickly evolved by NEAT. However for the purpose of this test, the networks were allowed to continue evolve, thereby increasing in complexity past the minimal solution, so as to have a larger network structures on average. After 30 generations of evolution, networks with an average of 11 ± 2 connections and 8 ± 1 nodes were produced. As many as 1 million (2^{20}) networks were evolved and evaluated.

Each network was then individually evaluated on the host machine, and the evaluation time tracked for 100 trials. Additionally this population was built into a homogenous-input composite neural network and evaluated on the GPU for an equivalent number of trials using the many-core methods described in this work. In Figure 4.9, the ratio of the time for the separate evaluation on a single CPU core to the composite evaluation on the GPU is compared. Beginning with small populations of 1024 networks, a modest speedup factor of ~ 2.5 is observed. As the number of neural networks evaluated is increased, the GPU utilization increases and strong scaling up to $\sim 65k$ networks is observed with a maximal performance speed up of $\sim 50x$.

In Fig. 4.9, the number of neural networks evaluated concurrently (the horizontal axis) is essentially a metric for operational intensity. The larger the neural network population (bigger problem size) the more arithmetic operations are performed per DRAM memory load (burst). This is principally due to the memory access coalescing of the network connections that is achieved by organizing the population of networks into a single composite network. Each memory access of the stored connections brings with it the needed information for all the neighboring GPU threads, minimizing the number of loads and increasing the amount of floating point operations per memory access.

The behavior observed in Figure 4.9 is well described by the roofline model [158]. The roofline model sets an upper bound on the performance of a compute kernel (network population evaluation, in this case) depending on the kernel’s operational intensity. Because the operational intensity scales with the neural network population size, the performance speedup shown in Fig. 4.9 traces out the effective performance roofline for this system. There are three identifiable performance regions that are observed. Specifically, the algorithm is

- *communication-bound* with population sizes between 2^{10} – 2^{12} neural networks,
- *memory-bound* with population sizes between 2^{12} – 2^{16} neural networks, and
- *compute-bound* with population sizes larger than 2^{16} neural networks.

With few neural networks in the genetic population, the peak performance is dominated by the time it takes to transfer the input and output data from the host to device and back. Even though only two memory transfers are required, the time required to evaluate the population of neural networks is comparable to this communication time and is therefore communication-bound.

However, as the number of networks increase, the peak performance gradually becomes memory-bound by the architecture. That is, the evaluation time is now much greater than the communication time, but the performance is dominated by the memory bandwidth. In this region, the more neural networks that are used, the more connections can be memory access coalesced, which means the GPU threads spend less time waiting for data to arrive from DRAM. Thus, in this region the performance increases with the operational intensity, or the number of neural networks evaluated concurrently.

Beyond 2^{16} neural networks, however, the performance reaches the compute-bound roofline in which it no longer improves with increasing computational load. This is reflective of the underlying algorithms utilization of the hardware. In this region, the number of operations per memory load no longer increases with increasing network population size. In this way, the time each GPU thread waits for connection data to arrive from DRAM has been minimized as much as achievable by the architecture. Thus, increasing the amount of connections to evaluate in parallel (increasing the population size), no longer improves the performance.

While the roofline or performance-plateau seen in Figure 4.9 is dictated by the architecture, the roofline could potentially be improved (a higher speedup achieved) if the underlying algorithm were improved to better utilize features of the architectures. For example, while the DAG-based algorithm described in this work takes great care to ensure memory access coalescing for the evaluated neural network connections, the application of each connection requires the load and store of node memory (the connection origin and destination nodes). Without optimization, these loads and stores are essentially random access, thus requiring a separate memory operation for each node. With consideration of the temporal node access-by, for example, determining an efficient ordering of nodes used in each evaluable connection set—the compute-bound performance roofline could be improved. Furthermore,

temporal consideration for both nodes and connections could be used to take advantage of shared memory on the GPU to further reduce memory latency.

4.6 Conclusion

In this work, new algorithms designed to optimize the concurrent evaluation of topologically divergent neural networks on many-core architectures are introduced. By pre-sorting the connections into evaluable sets, and parallelizing over the networks directed acyclic dependency graphs, nearly all branch divergence is eliminated from execution on SIMD processors. Furthermore, the factorization of many neural networks into a single composite network optimizes the memory access for network connections, and minimizes the host-device communication. When applying these techniques to populations of neural networks that were evolved via neuroevolution, the feedforward evaluation of these networks was significantly accelerated, with peak performance reaching 50 times the evaluation speed for each neural network on a single CPU thread. While this algorithm has been targeted principally for many-core SIMD architectures, multi-core CPUs would likely also greatly benefit from these methods. The refactorization described in section 4.4 is essentially a transposition of the population of neural networks from an array-of-structures into a structure-of-arrays data organization, which will take maximum advantage of per-core CPU cache. Moreover, the DAG-based algorithm described in section 4.3 would be well suited to a CPU thread pool or other task-based concurrency paradigm.

The novel algorithms presented in this work represent the first general-purpose mapping of large numbers of topologically heterogeneous neural networks to many-core architectures. Moreover, the achieved feedforward evaluation speedup is of particular importance to the

field of neuroevolution. The methods described here enable the networks evolved via neuroevolution to harness the compute capabilities of modern many-core architectures. Evolutionary algorithms are easily distributable across many compute nodes (for example, placing a population of neural networks on each node), and the algorithms presented here enable the evaluation of tens-to-hundreds of thousands of structurally diverse neural networks to now be offloaded to many-core accelerators available on these nodes. As the ability to harness distributed heterogeneous computing is a primary feature of modern machine learning frameworks, this work represents a step forward in enabling neuroevolution to better compete in this space.

Chapter 5

Summary & Outlook

Over the past two decades, there has been an impressive number of experimental programs studying Gamow-Teller distributions in pf -shell nuclei. Importantly, it has been found that the nuclear shell model appears to be able to describe the measurements in this region particularly well [13, 90]. This is a significant experimental, theoretical, and computational achievement, as it implies that allowed weak reactions for most iron-group nuclei near stability can be reliably estimated. As many astrophysical phenomenon rely on weak rates for these nuclei, significant constraints on the nuclear physics can now be placed, and other more significant uncertainties pursued. However, weak interaction rates for nuclei beyond the pf -shell, such as the neutron rich nuclei that have been shown to dominate the total electron capture rate in core-collapse supernovae, as well as heavier nuclei that also play an important role, remain poorly constrained. To date, weak interaction rates for these nuclei are often estimated by simple single-particle methods, and in many cases, phenomenological parameterizations which reproduce the data in the pf -shell but likely have orders of magnitude error for heavier and more neutron rich systems [31, 38, 64, 2, 88]. The impact that such uncertainties have on a variety of astrophysical environments remains an important open question in nuclear astrophysics.

As a logical continuation of the efforts of Cole *et al.* [13], where the authors systematically compared the inferred electron capture rates from many measurements and theoretical

calculations for nuclei in the pf -shell, the sensitivity study efforts I led investigated how the errors in this region (and more significantly, those outside the pf -shell) impact the early phases of core-collapse supernovae. This effort allowed us to understand on which nuclei experimental and theoretical efforts should focus. Furthermore, it is continuing to lend insight on how significantly these nuclei determine key characteristics of the events, such as the neutrino emission signal at core bounce, and the gravitational wave signal that would be emitted from a rotating star undergoing core-collapse [2, 3].

Ultimately, this work motivates a systematic study similar to that performed by Cole *et al.* [13] but for neutron-rich nuclei in the sdg -shell. As such an investigation relies on the availability of measurements and theoretical calculations for these nuclei, future efforts should focus in this region. Moving to heavier neutron rich nuclei, however, provides a unique experimental challenge, as there currently is no established method for studying β^+ Gamow-Teller distributions for radioactive nuclei. It is therefore of critical importance to develop new techniques that take advantage of inverse kinematics, where the investigated radioactive nuclei are formed as secondary beams at fast-fragmentation facilities. A promising method is the $(d, {}^2\text{He})$ charge-exchange reaction, wherein a rare isotope beam is produced and impinged on an active target time projection chamber (TPC) filled with deuterium gas. In such a measurement the time projection chamber would be utilized to track the position and energy of the recoiling protons (which are emitted from the ${}^2\text{He}$ system). As the $(d, {}^2\text{He})$ reaction will induce β^+ transitions in the neutron-rich rare isotope beam, these astrophysically important nuclei would be accessible for the first time. Similarly, neutron rich nuclei in the sdg -shell, as well as the very neutron rich systems on the border of the pf and sdg -shells, represent a significant theoretical challenge due to the large many-body configuration space.

Moreover, forbidden transitions (non zero orbital angular momentum transfer) also play

an important role in astrophysical environments, specifically in the case of core-collapse supernovae where the electron chemical potential is large enough that electrons can induce non-negligible rates for these transitions [38]. Unfortunately, configuration-interaction shell model methods for estimating these rates are not presently available, because the extremely large model spaces. Popular alternatives such as quasi-random phase approximations (QRPA) are able to estimate rates for forbidden transitions in large sets of nuclei, however there are also no measurements available from which such estimates can be evaluated. Furthermore, QRPA estimates have been shown to reproduce the data for allowed Gamow-Teller transitions only poorly [13]. Because of the astrophysical importance of forbidden weak interactions in nuclei, significant experimental and theoretical investments should be made in this area.

Computationally, the weak interaction rate library that has been produced as part of this work has received several updates since its implementation described in chapter 2. As it is the first comprehensive set of weak rates across many different nuclear species, its incorporation into the simulation of other astrophysical phenomenon—where weak interactions on nuclei are suspected to play an important role—presents a unique opportunity to learn more about the impact of the weak interaction in nuclear astrophysics.

In chapter 3, a new method for extracting Gamow-Teller transition strengths in the inelastic neutral-current channel was presented. This work runs parallel to the above charged-current weak interaction investigations, as it allows for the indirect constraint of the neutral-current weak response of nuclei which is also of importance in astrophysics. The (${}^6\text{Li}, {}^6\text{Li}' + \gamma$) reaction has been established as a probe of inelastic isovector-spin transfer excitations in nuclei. Furthermore, the Gamow-Teller unit cross section for ${}^6\text{Li}$ inelastic scattering was extracted and agrees well with estimates from charge-exchange and theoretical calculations.

While the method has limited reach due to being experimentally challenging, it enables the direct extraction of inelastic Gamow-Teller transition strength for light nuclei. As the Gamow-Teller transition strength is the primary ingredient to inelastic neutrino-nucleus scattering cross sections, the $({}^6\text{Li}, {}^6\text{Li}' + \gamma)$ reaction provides a novel indirect technique that can supplement, and in some cases replace, the need for multi-year direct measurements with neutrino beams [159].

In the final chapter of this work, the development and performance of a newly established technique in artificial intelligence is described. While wholly separate from the physics previously discussed, these algorithmic advancements seek to enable neuroevolution to take advantage of modern heterogeneous compute architectures, so that scientists with HPC centers at their disposal may better employ machine learning in their respective domains. The principal focus of the algorithm optimizations described in chapter 4 were on improving the feed-forward evaluation time when tens-to-hundreds of thousands of heterogeneous neural networks are evaluated concurrently. The evolution of these neural networks through hyperparameter and structural space presents a novel divergence problem when mapping the evaluation of these networks to many-core architectures. Because the evolution of neural network populations offloads the model choice and refinement process to an evolutionary search algorithm, neuroevolution increases the accessibility of machine learning to novice users, and thus motivates the need for a solution to the above described divergence problem.

The algorithms described in chapter 4 provide a new evaluation paradigm which enables the processing of many heterogeneous neural networks concurrently on many-core architectures. By pre-sorting the connections into evaluatable sets, and parallelizing over the network's directed acyclic dependency graphs, nearly all branch divergence is eliminated. Principally, this is because the relationships between operations in network evaluation can

be ordered so that heterogeneity in network structure is ignored, and that at each step, SIMD parallelism is maximized. Thus, these methods represent a general-purpose mapping of large numbers of structurally diverse neural networks, including recurrent neural networks, to many-core architectures. As the ability to harness distributed heterogeneous computing is a primary feature of modern machine-learning frameworks, these algorithms represent a few of the needed steps toward enabling neuroevolution to lower the machine learning barrier for use in scientific endeavors. Moving forward, the application of this DAG-based method in reverse-mode differentiation for neural-network training would be the next logical step. Furthermore, as evolutionary algorithms employed in neuroevolution can be easily distributed across many CPUs, a distributed implementation of neuroevolution which harnesses the heterogeneous network evaluation described in this work should be developed, as it will greatly increase the search capability of neural-network evolution.

BIBLIOGRAPHY

BIBLIOGRAPHY

- [1] M. R. Mumpower, R. Surman, D.-L. Fang, M. Beard, P. Möller, T. Kawano, and A. Aprahamian, *Physical Review C* **92**, 035807 (2015).
- [2] C. Sullivan, E. O'Connor, R. G. T. Zegers, T. Grubb, and S. M. Austin, *The Astrophysical Journal* **816**, 44 (2016).
- [3] S. Richers, C. D. Ott, E. Abdikamalov, E. O'Connor, and C. Sullivan, *Physical Review D* **95**, 063019 (2017).
- [4] G. Carleo and M. Troyer, *Science* **355**, 602 (2017).
- [5] J. Carrasquilla and R. G. Melko, *Nature Physics* **13**, 431 (2017).
- [6] A. Waltar, in *Proceedings of the Americas Nuclear Energy Symposium* (2004).
- [7] K. Langanke and G. Martínez-Pinedo, *Reviews of Modern Physics* **75**, 819 (2003).
- [8] E. Fermi, *Zeitschrift für Physik* **88**, 161 (1934).
- [9] B. Pontecorvo, *Soviet Journal of Experimental and Theoretical Physics* **9**, 1148 (1959), [*Zh. Eksp. Teor. Fiz.*36,1615(1959)].
- [10] D. Z. Freedman, *Physical Review D* **9**, 1389 (1974).
- [11] T. J. Mazurek, *Astrophysics and Space Science* **35**, 117 (1975).
- [12] K. Sato, *Progress of Theoretical Physics* **54**, 1325 (1975).
- [13] A. L. Cole, T. S. Anderson, R. G. T. Zegers, S. M. Austin, B. a. Brown, L. Valdez, S. Gupta, G. W. Hitt, and O. Fawwaz, *Physical Review C* **86**, 015809 (2012).
- [14] M. Georgiopoulos, R. F. DeMara, A. J. Gonzalez, A. S. Wu, M. Mollaghasemi, E. Gelenbe, M. Kysilka, J. Secretan, C. A. Sharma, and A. J. Alnsour, *IEEE Transactions on Education* **52**, 503 (2009).

- [15] P. Anderson, J. McGuffee, and D. Uminsky, in *Proceedings of the 45th ACM Technical Symposium on Computer Science Education*, SIGCSE '14 (ACM, New York, NY, USA, 2014) pp. 705–706.
- [16] F. Pedregosa, G. Varoquaux, A. Gramfort, V. Michel, B. Thirion, O. Grisel, M. Blondel, P. Prettenhofer, R. Weiss, V. Dubourg, J. Vanderplas, A. Passos, D. Cournapeau, M. Brucher, M. Perrot, and E. Duchesnay, *The Journal of Machine Learning Research* **12**, 2825 (2011).
- [17] M. Abadi, P. Barham, J. Chen, Z. Chen, A. Davis, J. Dean, M. Devin, S. Ghemawat, G. Irving, M. Isard, M. Kudlur, J. Levenberg, R. Monga, S. Moore, D. G. Murray, B. Steiner, P. Tucker, V. Vasudevan, P. Warden, M. Wicke, Y. Yu, and X. Zheng, in *Proceedings of the 12th USENIX Conference on Operating Systems Design and Implementation*, OSDI'16 (USENIX Association, Berkeley, CA, USA, 2016) pp. 265–283.
- [18] C. Thornton, F. Hutter, H. H. Hoos, and K. Leyton-Brown, in *Proceedings of the 19th ACM SIGKDD International Conference on Knowledge Discovery and Data Mining*, KDD '13 (ACM, New York, NY, USA, 2013) pp. 847–855.
- [19] M. Claesen and B. D. Moor, Computing Research Repository **abs/1502.02127** (2015), arXiv:1502.02127 .
- [20] G. E. Hinton, “A Practical Guide to Training Restricted Boltzmann Machines,” in *Neural Networks: Tricks of the Trade: Second Edition*, edited by G. Montavon, G. B. Orr, and K.-R. Müller (Springer Berlin Heidelberg, Berlin, Heidelberg, 2012) pp. 599–619.
- [21] M. Claesen, J. Simm, D. Popovic, Y. Moreau, and B. D. Moor, Computing Research Repository **abs/1412.1114** (2014), arXiv:1412.1114 .
- [22] S. Viaene, *IT Professional* **15**, 12 (2013).
- [23] M. Feurer, A. Klein, K. Egensperger, J. Springenberg, M. Blum, and F. Hutter, in *Advances in Neural Information Processing Systems 28*, edited by C. Cortes, N. D. Lawrence, D. D. Lee, M. Sugiyama, and R. Garnett (Curran Associates, Inc., 2015) pp. 2962–2970.
- [24] R. Miikkulainen, J. Z. Liang, E. Meyerson, A. Rawal, D. Fink, O. Francon, B. Raju, H. Shahrzad, A. Navruzyan, N. Duffy, and B. Hodjat, Computing Research Repository **abs/1703.00548** (2017), arXiv:1703.00548 .

- [25] C. Fernando, D. Banarse, M. Reynolds, F. Besse, D. Pfau, M. Jaderberg, M. Lantot, and D. Wierstra, Computing Research Repository [abs/1606.02580](https://arxiv.org/abs/1606.02580) (2016), arXiv:1606.02580 .
- [26] X. Yao, Proceedings of the IEEE **87**, 1423 (1999).
- [27] A. Heger, K. Langanke, G. Martínez-Pinedo, and S. E. Woosley, Physical Review Letters **86**, 1678 (2001).
- [28] G. Martínez-Pinedo, Y. H. Lam, K. Langanke, R. G. T. Zegers, and C. Sullivan, Physical Review C **89**, 045806 (2014).
- [29] K. Iwamoto, F. Brachwitz, K. Nomoto, N. Kishimoto, H. Umeda, W. R. Hix, and F.-K. Thielemann, The Astrophysical Journal Supplement Series **125**, 439 (1999).
- [30] F. Brachwitz, D. J. Dean, W. R. Hix, K. Iwamoto, K. Langanke, G. Martnez-Pinedo, K. Nomoto, M. R. Strayer, F.-K. Thielemann, and H. Umeda, The Astrophysical Journal **536**, 934 (2000).
- [31] W. R. Hix, O. E. B. Messer, A. Mezzacappa, M. Liebendoerfer, J. Sampaio, K. Langanke, D. J. Dean, and G. Martínez-Pinedo, Physical Review Letters **91**, 201102 (2003).
- [32] H.-T. Janka, K. Langanke, A. Marek, G. Martnez-Pinedo, and B. Mller, Physics Reports **442**, 38 (2007), the Hans Bethe Centennial Volume 1906-2006.
- [33] S. Gupta, E. F. Brown, H. Schatz, P. Möller, and K.-L. Kratz, The Astrophysical Journal **662**, 1188 (2007).
- [34] H. Schatz, S. Gupta, P. Möller, M. Beard, E. F. Brown, A. T. Deibel, L. R. Gasques, W. R. Hix, L. Keek, R. Lau, A. W. Steiner, and M. Wiescher, Nature **505**, 62 (2014).
- [35] S. Goriely, A. Bauswein, O. Just, E. Pillumbi, and H.-T. Janka, Monthly Notices of the Royal Astronomical Society **452**, 3894 (2015).
- [36] K. Langanke and G. Martínez-Pinedo, Nuclear Physics A **673**, 481 (2000).
- [37] T. Oda, M. Hino, K. Muto, M. Takahara, and K. Sato, Atomic Data and Nuclear Data Tables **56**, 231 (1994).

- [38] K. Langanke, G. Martínez-Pinedo, J. M. Sampaio, D. J. Dean, W. R. Hix, O. E. B. Messer, A. Mezzacappa, M. Liebendörfer, H.-T. Janka, and M. Rampp, *Physical Review Letters* **90**, 241102 (2003).
- [39] N. Paar, G. Colò, E. Khan, and D. Vretenar, *Physical Review C* **80**, 055801 (2009).
- [40] P. Möller and J. Randrup, *Nuclear Physics A* **514**, 1 (1990).
- [41] A. A. Dzhiboev, A. I. Vdovin, V. Y. Ponomarev, J. Wambach, K. Langanke, and G. Martínez-Pinedo, *Physical Review C* **81**, 015804 (2010).
- [42] Y. F. Niu, N. Paar, D. Vretenar, and J. Meng, *Physical Review C* **83**, 045807 (2011).
- [43] J.-U. Nabi and H. V. Klapdor-Kleingrothaus, *Atomic Data and Nuclear Data Tables* **88**, 237 (2004).
- [44] M. Scott, Y. Shimbara, S. M. Austin, D. Bazin, B. A. Brown, J. M. Deaven, Y. Fujita, C. J. Guess, S. Gupta, G. W. Hitt, D. Koeppe, R. Meharchand, M. Nagashima, G. Perdikakis, A. Prinke, M. Sasano, C. Sullivan, L. Valdez, and R. G. T. Zegers, *Physical Review C* **90**, 025801 (2014).
- [45] S. Noji, R. Zegers, S. M. Austin, T. Baugher, D. Bazin, B. Brown, C. Campbell, A. Cole, H. Doster, A. Gade, C. Guess, S. Gupta, G. Hitt, C. Langer, S. Lipschutz, E. Lunderberg, R. Meharchand, Z. Meisel, G. Perdikakis, J. Pereira, F. Recchia, H. Schatz, M. Scott, S. Stroberg, C. Sullivan, L. Valdez, C. Walz, D. Weisshaar, S. Williams, and K. Wimmer, *Physical Review Letters* **112**, 252501 (2014).
- [46] A. Poves, J. Snchez-Solano, E. Caurier, and F. Nowacki, *Nuclear Physics A* **694**, 157 (2001).
- [47] M. Honma, T. Otsuka, B. Brown, and T. Mizusaki, *The European Physical Journal A - Hadrons and Nuclei* **25**, 499 (2005).
- [48] E. O'Connor and C. D. Ott, *Classical and Quantum Gravity* **27**, 114103 (2010).
- [49] A. Dubey, K. Antypas, M. K. Ganapathy, L. B. Reid, K. Riley, D. Sheeler, A. Siegel, and K. Weide, *Parallel Computing* **35**, 512 (2009).
- [50] B. Fryxell, K. Olson, P. Ricker, F. X. Timmes, M. Zingale, D. Q. Lamb, P. MacNeice, R. Rosner, J. W. Truran, and H. Tufo, *The Astrophysical Journal Supplement Series* **131**, 273 (2000).

- [51] H. Dimmelmeier, J. Novak, J. A. Font, J. M. Ibáñez, and E. Müller, *Physical Review D* **71**, 064023 (2005).
- [52] Dimmelmeier, H., Font, J. A., and Mller, E., *A&A* **393**, 523 (2002).
- [53] C. Iliadis, *Nuclear Physics of Stars, by Christian Iliadis. ISBN 978-3-527-40602-9. Published by Wiley-VCH Verlag, Weinheim, Germany, 2007.* (Wiley-VCH Verlag, 2007).
- [54] K. Langanke and G. Martnez-Pinedo, *Nuclear Physics A* **928**, 305 (2014), special Issue Dedicated to the Memory of Gerald E Brown (1926-2013).
- [55] G. Martínez-Pinedo, K. Langanke, and D. J. Dean, *The Astrophysical Journal Supplement Series* **126**, 493 (2000).
- [56] H. Bethe, G. Brown, J. Applegate, and J. Lattimer, *Nuclear Physics A* **324**, 487 (1979).
- [57] G. M. Fuller, W. A. Fowler, and M. J. Newman, *The Astrophysical Journal* **252**, 715 (1982).
- [58] A. Juodagalvis, K. Langanke, W. Hix, G. Martínez-Pinedo, and J. Sampaio, *Nuclear Physics A* **848**, 454 (2010).
- [59] E. O'Connor, *The Astrophysical Journal Supplement Series* **219**, 24 (2015).
- [60] K. Langanke, E. Kolbe, and D. J. Dean, *Physical Review C* **63**, 032801 (2001).
- [61] S. W. Bruenn, *The Astrophysical Journal Supplement Series* **58**, 771 (1985).
- [62] G. M. Fuller, W. A. Fowler, and M. J. Newman, *The Astrophysical Journal* **293**, 1 (1985).
- [63] M. Steffen, *Astronomy & Astrophysics* **239**, 443 (1990).
- [64] A. Juodagalvis, J. M. Sampaio, K. Langanke, and W. R. Hix, *Journal of Physics G: Nuclear and Particle Physics* **35**, 014031 (2008).
- [65] A. Burrows, S. Reddy, and T. a. Thompson, *Nuclear Physics A* **777**, 356 (2006).

- [66] C. J. Horowitz, *Physical Review D* **65**, 043001 (2002).
- [67] C. J. Horowitz, *Physical Review D* **55**, 4577 (1997).
- [68] K. Langanke, G. Martínez-Pinedo, and J. Sampaio, *Physical Review C* **64**, 055801 (2001).
- [69] M. Hempel and J. Schaffner-Bielich, *Nuclear Physics A* **837**, 210 (2010).
- [70] A. W. Steiner, M. Hempel, and T. Fischer, *The Astrophysical Journal* **774**, 17 (2013).
- [71] S. Typel, G. Röpke, T. Klähn, D. Blaschke, and H. H. Wolter, *Physical Review C* **81**, 015803 (2010).
- [72] H. Toki, D. Hirata, Y. Sugahara, K. Sumiyoshi, and I. Tanihata, *Nuclear Physics A* **588**, c357 (1995).
- [73] T. Fischer, M. Hempel, I. Sagert, Y. Suwa, and J. Schaffner-Bielich, *The European Physical Journal A* **50**, 46 (2014).
- [74] P. Möller, J. Nix, W. Myers, and W. Swiatecki, *Atomic Data and Nuclear Data Tables* **59**, 185 (1995).
- [75] P. Möller, J. Nix, and K.-L. Kratz, *Atomic Data and Nuclear Data Tables* **66**, 131 (1997).
- [76] L. Geng, H. Toki, and J. Meng, *Progress of Theoretical Physics* **113**, 785 (2005).
- [77] G. Audi, A. Wapstra, and C. Thibault, *Nuclear Physics A* **729**, 337 (2003).
- [78] S. E. Woosley and T. A. Weaver, *The Astrophysical Journal Supplement Series* **101**, 181 (1995).
- [79] S. Woosley and A. Heger, *Physics Reports* **442**, 269 (2007).
- [80] E. O'Connor and C. D. Ott, *The Astrophysical Journal* **730**, 70 (2011).
- [81] M. Liebendorfer, *The Astrophysical Journal* **633**, 1042 (2005).
- [82] C. F. J. Wu, *The Annals of Statistics* **14**, 1261 (1986).

- [83] E. O'Connor and C. D. Ott, *The Astrophysical Journal* **762**, 126 (2013).
- [84] T. Suzuki, H. Toki, and K. Nomoto, *The Astrophysical Journal* **817**, 163 (2016).
- [85] M. Honma, T. Otsuka, T. Mizusaki, M. Hjorth-Jensen, and B. A. Brown, *Journal of Physics: Conference Series* **20**, 7 (2005).
- [86] J. Pruet and G. M. Fuller, *The Astrophysical Journal Supplement Series* **149**, 189 (2003).
- [87] A. R. Raduta, F. Gulminelli, and M. Oertel, *Physical Review C* **95**, 025805 (2017).
- [88] R. Titus, C. Sullivan, R. G. T. Zegers, B. A. Brown, and B. Gao, *Journal of Physics G: Nuclear and Particle Physics* (2017).
- [89] K. Scholberg, *Annual Review of Nuclear and Particle Science* **62**, 81 (2012).
- [90] K. Langanke and G. Martinez-Pinedo, *Nuclear Physics A* **928**, 305 (2014), special Issue Dedicated to the Memory of Gerald E Brown (1926-2013).
- [91] W. C. Haxton, *Physical Review Letters* **60**, 1999 (1988).
- [92] W. R. Hix, A. Mezzacappa, O. E. B. Messer, and S. W. Bruenn, *Journal of Physics G: Nuclear and Particle Physics* **29**, 2523 (2003).
- [93] B. Bodmann, N. Booth, F. Burtak, A. Dodd, G. Drexlin, V. Eberhard, K. Eitel, J. Edgington, E. Finckh, H. Gemmeke, G. Giorginis, A. Glombik, T. Gorringer, W. Grandegger, T. Hanika, J. Höβl, M. Kleifges, J. Kleinfeller, W. Kretschmer, A. Malik, R. Maschuw, R. Meyer, P. Plischke, J. Rapp, F. Raupp, F. Schilling, B. Seligmann, J. Wochele, J. Wolf, S. Wölffe, and B. Zeitnitz, *Physics Letters B* **280**, 198 (1992).
- [94] R. Imlay, *Nuclear Physics A* **A629**, 531 (1998).
- [95] A. Tamii, Y. Fujita, H. Matsubara, T. Adachi, J. Carter, M. Dozono, H. Fujita, K. Fujita, H. Hashimoto, K. Hatanaka, T. Itahashi, M. Itoh, T. Kawabata, K. Nakanishi, S. Ninomiya, A. Perez-Cerdan, L. Popescu, B. Rubio, T. Saito, H. Sakaguchi, Y. Sakemi, Y. Sasamoto, Y. Shimbara, Y. Shimizu, F. Smit, Y. Tameshige, M. Yosoi, and J. Zenhiro, *Nuclear Instruments and Methods in Physics Research Section A: Accelerators, Spectrometers, Detectors and Associated Equipment* **605**, 326 (2009).

- [96] A. Tamii, I. Poltoratska, P. von Neumann-Cosel, Y. Fujita, T. Adachi, C. A. Bertulani, J. Carter, M. Dozono, H. Fujita, K. Fujita, K. Hatanaka, D. Ishikawa, M. Itoh, T. Kawabata, Y. Kalmykov, A. M. Krumbholz, E. Litvinova, H. Matsubara, K. Nakanishi, R. Neveling, H. Okamura, H. J. Ong, B. Özel-Tashenov, V. Y. Ponomarev, A. Richter, B. Rubio, H. Sakaguchi, Y. Sakemi, Y. Sasamoto, Y. Shimbara, Y. Shimizu, F. D. Smit, T. Suzuki, Y. Tameshige, J. Wambach, R. Yamada, M. Yosoi, and J. Zenihiro, *Physical Review Letters* **107**, 062502 (2011).
- [97] I. Poltoratska, P. von Neumann-Cosel, A. Tamii, T. Adachi, C. A. Bertulani, J. Carter, M. Dozono, H. Fujita, K. Fujita, Y. Fujita, K. Hatanaka, M. Itoh, T. Kawabata, Y. Kalmykov, A. M. Krumbholz, E. Litvinova, H. Matsubara, K. Nakanishi, R. Neveling, H. Okamura, H. J. Ong, B. Özel-Tashenov, V. Y. Ponomarev, A. Richter, B. Rubio, H. Sakaguchi, Y. Sakemi, Y. Sasamoto, Y. Shimbara, Y. Shimizu, F. D. Smit, T. Suzuki, Y. Tameshige, J. Wambach, M. Yosoi, and J. Zenihiro, *Physical Review C* **85**, 041304 (2012).
- [98] D. I. Sober, B. C. Metsch, W. Knüpfer, G. Eulenberg, G. Kuchler, A. Richter, E. Spamer, and W. Steffen, *Physical Review C* **31**, 2054 (1985).
- [99] O. Burda, N. Botha, J. Carter, R. W. Fearick, S. V. Förtsch, C. Fransen, H. Fujita, J. D. Holt, M. Kuhar, A. Lenhardt, P. von Neumann-Cosel, R. Neveling, N. Pietralla, V. Y. Ponomarev, A. Richter, O. Scholten, E. Sideras-Haddad, F. D. Smit, and J. Wambach, *Physical Review Letters* **99**, 092503 (2007).
- [100] K. Langanke, G. Martínez-Pinedo, P. von Neumann-Cosel, and A. Richter, *Physical Review Letters* **93**, 202501 (2004).
- [101] T. W. Donnelly and R. D. Peccei, *Physics Reports* **50**, 1 (1979).
- [102] S. M. Austin, N. Anantaraman, and J. S. Winfield, *Canadian Journal of Physics* **65**, 609 (1987).
- [103] D. Tilley, C. Cheves, J. Godwin, G. Hale, H. Hofmann, J. Kelley, C. Sheu, and H. Weller, *Nuclear Physics A* **708**, 3 (2002).
- [104] M. A. Franey and W. G. Love, *Physical Review C* **31**, 488 (1985).
- [105] M. Fujiwara, H. Akimune, I. Daito, H. Fujimura, Y. Fujita, K. Hatanaka, H. Ikegami, I. Katayama, K. Nagayama, N. Matsuoka, S. Morinobu, T. Noro, M. Yoshimura, H. Sakaguchi, Y. Sakemi, A. Tamii, and M. Yosoi, *Nuclear Instruments and Methods in Physics Research Section A: Accelerators, Spectrometers, Detectors and Associated Equipment* **422**, 484 (1999).

- [106] H. Matsubara, *Isoscalar and isovector spin-M1 transitions from the even-even, $N = Z$ nuclei across the sd-shell region*, Ph.D. thesis, Osaka University (2010).
- [107] A. Tamii, H. Sakaguchi, H. Takeda, M. Yosoi, H. Akimune, M. Fujiwara, H. Ogata, M. Tanaka, and H. Togawa, *IEEE Transactions on Nuclear Science* **43**, 2488 (1996).
- [108] M. Cromaz, V. Riot, P. Fallon, S. Gros, B. Holmes, I. Lee, A. Macchiavelli, C. Vu, H. Yaver, and S. Zimmermann, *Nuclear Instruments and Methods in Physics Research Section A: Accelerators, Spectrometers, Detectors and Associated Equipment* **597**, 233 (2008).
- [109] J. T. Anderson, M. Albers, M. Alcorta, C. Campbell, M. P. Carpenter, C. J. Chiara, M. Cromaz, H. M. David, D. Doering, D. T. Doherty, C. R. Hoffman, R. V. F. Janssens, J. Joseph, T. L. Khoo, A. Kreps, T. Lauritsen, I. Y. Lee, C. Lionberger, C. J. Lister, T. Madden, M. B. Oberling, A. M. Rogers, D. Seweryniak, P. Wilt, S. Zhu, and S. Zimmermann, in *2012 IEEE Nuclear Science Symposium and Medical Imaging Conference Record (NSS/MIC)* (IEEE, 2012) pp. 1536–1540.
- [110] A. Tamii, *Polarization transfer observables for proton inelastic scattering from ^{12}C at zero degrees*, Ph.D. thesis, Kyoto University (1999).
- [111] P. Bender, E. Lunderberg, C. Sullivan, *et al.*, “CAGRA-GrandRaiden/GRUTinizer: 1st Post RCNP CAGRA+GR Experimental Campaign Release,” (2017).
- [112] E. Lunderberg, *Subbarrier coulomb excitation at REA3, commissioning of the SeGA-Janus experimental setup*, Ph.D. thesis, Michigan State University (2017).
- [113] M. P. C. S. Zhu, private communication (2017).
- [114] M. A. Moinester, *Canadian Journal of Physics* **65**, 660 (1987).
- [115] J. Cook and J. Carr, Computer program FOLD. Florida State University (unpublished); based on F. Petrovich and D. Stanley, *Nuclear Physics A* 275:487, 1977; modified as described in J. Cook *et al.*, *Physical Review C* 30:1538, 1984; R.G.T. Zegers (2005), unpublished.
- [116] R. G. T. Zegers, T. Adachi, H. Akimune, S. M. Austin, A. M. van den Berg, B. A. Brown, Y. Fujita, M. Fujiwara, S. Galès, C. J. Guess, M. N. Harakeh, H. Hashimoto, K. Hatanaka, R. Hayami, G. W. Hitt, M. E. Howard, M. Itoh, T. Kawabata, K. Kawase, M. Kinoshita, M. Matsubara, K. Nakanishi, S. Nakayama, S. Okumura, T. Ohta, Y. Sakemi, Y. Shimbara, Y. Shimizu, C. Scholl, C. Simenel, Y. Tameshige, A. Tamii, M. Uchida, T. Yamagata, and M. Yosoi, *Physical Review Letters* **99**, 202501 (2007).

- [117] G. Perdikakis, R. G. T. Zegers, S. M. Austin, D. Bazin, C. Caesar, J. M. Deaven, A. Gade, D. Galaviz, G. F. Grinyer, C. J. Guess, C. Herlitzius, G. W. Hitt, M. E. Howard, R. Meharchand, S. Noji, H. Sakai, Y. Shimbara, E. E. Smith, and C. Tur, *Physical Review C* **83**, 054614 (2011).
- [118] M. Scott, R. G. T. Zegers, R. Almus, S. M. Austin, D. Bazin, B. A. Brown, C. Campbell, A. Gade, M. Bowry, S. Galès, U. Garg, M. N. Harakeh, E. Kwan, C. Langer, C. Loelius, S. Lipschutz, E. Litvinova, E. Lunderberg, C. Morse, S. Noji, G. Perdikakis, T. Redpath, C. Robin, H. Sakai, Y. Sasamoto, M. Sasano, C. Sullivan, J. A. Tostevin, T. Uesaka, and D. Weisshaar, *Physical Review Letters* **118**, 172501 (2017).
- [119] B. A. Brown *et al.*, (2004), NSCL report MSUCL-1289 (unpublished).
- [120] S. Cohen and D. Kurath, *Nuclear Physics* **73**, 1 (1965).
- [121] E. K. Warburton and B. A. Brown, *Physical Review C* **46**, 923 (1992).
- [122] B. Alex Brown, *Physical Review C* **58**, 220 (1998).
- [123] K. Schwarz, C. Samanta, M. Fujiwara, H. Rebel, R. De Leo, N. Matsuoka, H. Utsunomiya, H. Akimune, I. Daito, H. Fujimura, F. Ihara, K. Ishibashi, Y. Maeda, T. Yamanaka, H. Yoshida, A. Okihana, T. Yoshimura, P. van Aarle, W. Uijen, M. Ito, and Y. Sakuragi, *The European Physical Journal A* **7**, 367 (2000).
- [124] J. Raynal, Notes on ECIS97 (unpublished).
- [125] G. Perdikakis, R. G. T. Zegers, S. M. Austin, D. Bazin, C. Caesar, J. M. Deaven, A. Gade, D. Galaviz, G. F. Grinyer, C. J. Guess, C. Herlitzius, G. W. Hitt, M. E. Howard, R. Meharchand, S. Noji, H. Sakai, Y. Shimbara, E. E. Smith, and C. Tur, *Physical Review C* **83**, 054614 (2011).
- [126] B. Bodmann, N. Booth, F. Burtak, A. Dodd, G. Drexlin, V. Eberhard, J. Edgington, E. Finckh, H. Gemmeke, G. Giorginis, A. Glombik, T. Gorringer, W. Grandegger, T. Hanika, M. Kleifges, J. Kleinfeller, W. Kretschmer, A. Malik, R. Maschuw, R. Meyer, P. Plischke, F. Raupp, F. Schilling, B. Seligmann, J. Wochele, J. Wolf, S. Wölffe, and B. Zeitnitz, *Physics Letters B* **267**, 321 (1991).
- [127] T. N. Taddeucci, L. Alamos, T. A. Carey, C. Gaarde, J. Larsen, D. Horen, O. R. National, O. Ridge, J. Rapaport, and E. Sugarbaker, **469**, 125 (1987).
- [128] H. Matsubara, A. Tamii, H. Nakada, T. Adachi, J. Carter, M. Dozono, H. Fujita, K. Fujita, Y. Fujita, K. Hatanaka, W. Horiuchi, M. Itoh, T. Kawabata,

- S. Kuroita, Y. Maeda, P. Navrátil, P. von Neumann-Cosel, R. Neveling, H. Okamura, L. Popescu, I. Poltoratska, A. Richter, B. Rubio, H. Sakaguchi, S. Sakaguchi, Y. Sakemi, Y. Sasamoto, Y. Shimbara, Y. Shimizu, F. D. Smit, K. Suda, Y. Tameshige, H. Tokieda, Y. Yamada, M. Yosoi, and J. Zenihiro, *Physical Review Letters* **115**, 102501 (2015).
- [129] T. N. Taddeucci, C. A. Goulding, and T. A. Carey, *Nuclear Physics* **A469**, 125 (1987).
- [130] M. N. Harakeh and A. van der Woude, *Giant Resonances: Fundamental High-Frequency Modes of Nuclear Excitations* (Oxford University Press, New York, 2001).
- [131] J. Fridmann *et al.*, *Physical Review C* **74**, 034313 (2006).
- [132] S. van der Werf, “Normod,” Unpublished.
- [133] N. Anantaraman *et al.*, *Physical Review C* **44**, 398 (1991).
- [134] A. Nadasen *et al.*, *Physical Review C* **39**, 536 (1989).
- [135] H. Laurent, S. Gals, D. Beaumel, G. Crawford, J. Finck, S. Fortier, J. Maison, C. Masolo, D. Mercer, J. Winfield, and G. Yoo, *Nuclear Physics A* **569**, 297 (1994).
- [136] S. Paschalis, I. Lee, A. Macchiavelli, C. Campbell, M. Cromaz, S. Gros, J. Pavan, J. Qian, R. Clark, H. Crawford, D. Doering, P. Fallon, C. Lionberger, T. Loew, M. Petri, T. Stezelberger, S. Zimmermann, D. Radford, K. Lagergren, D. Weisshaar, R. Winkler, T. Glasmacher, J. Anderson, and C. Beausang, *Nuclear Instruments and Methods in Physics Research Section A: Accelerators, Spectrometers, Detectors and Associated Equipment* **709**, 44 (2013).
- [137] T. Lauritsen, A. Korichi, S. Zhu, A. Wilson, D. Weisshaar, J. Dudouet, A. Ayangeakaa, M. Carpenter, C. Campbell, E. Clment, H. Crawford, M. Cromaz, P. Fallon, J. Greene, R. Janssens, T. Khoo, N. Lalovi, I. Lee, A. Macchiavelli, R. Perez-Vidal, S. Pietri, D. Radford, D. Ralet, L. Riley, D. Seweryniak, and O. Stezowski, *Nuclear Instruments and Methods in Physics Research Section A: Accelerators, Spectrometers, Detectors and Associated Equipment* **836**, 46 (2016).
- [138] D. Weisshaar, D. Bazin, P. Bender, C. Campbell, F. Recchia, V. Bader, T. Baugher, J. Belarge, M. Carpenter, H. Crawford, M. Cromaz, B. Elman, P. Fallon, A. Forney, A. Gade, J. Harker, N. Kobayashi, C. Langer, T. Lauritsen, I. Lee, A. Lemasson, B. Longfellow, E. Lunderberg, A. Macchiavelli, K. Miki, S. Momiyama, S. Noji, D. Radford, M. Scott, J. Sethi, S. Stroberg, C. Sullivan, R. Titus, A. Wiens, S. Williams,

- K. Wimmer, and S. Zhu, Nuclear Instruments and Methods in Physics Research Section A: Accelerators, Spectrometers, Detectors and Associated Equipment **847**, 187 (2017).
- [139] U. Garg, private communication (2017).
- [140] W. S. McCulloch and W. Pitts, The Bulletin of Mathematical Biophysics **5**, 115 (1943).
- [141] B. Cheng and D. M. Titterington, Statistical Science **9**, 2 (1994).
- [142] A. J. Turner and J. F. Miller, Evolutionary Intelligence **7**, 135 (2014).
- [143] S. M. Carroll and B. W. Dickinson, International 1989 Joint Conference on Neural Networks , 607 (1989).
- [144] J. Hu, J. Zhang, C. Zhang, and J. Wang, Neurocomputing **171**, 63 (2016).
- [145] K. O. Stanley and R. Miikkulainen, Evolutionary Computation **10**, 99 (2002).
- [146] C. Peterson, Nuclear Physics News **2**, 14 (1992).
- [147] P. Baldi, P. Sadowski, and D. Whiteson, Nature Communications **5**, 4308 (2014).
- [148] A. Aurisano, A. Radovic, D. Rocco, A. Himmel, M. Messier, E. Niner, G. Pawloski, F. Psihas, A. Sousa, and P. Vahle, Journal of Instrumentation **11**, P09001 (2016).
- [149] T. Aaltonen, J. Adelman, T. Akimoto, M. G. Albrow, B. Álvarez González, S. Amelio, D. Amidei, A. Anastassov, A. Annovi, J. Antos, G. Apollinari, A. Apresyan, T. Arisawa, A. Artikov, W. Ashmanskas, A. Attal, A. Aurisano, F. Azfar, P. Azzurri, W. Badgett, A. Barbaro-Galtieri, V. E. Barnes, B. A. Barnett, V. Bartsch, G. Bauer, P.-H. Beauchemin, F. Bedeschi, P. Bednar, D. Beecher, S. Behari, G. Bellottini, J. Bellinger, D. Benjamin, A. Beretvas, J. Beringer, A. Bhatti, M. Binkley, D. Bisello, I. Bizjak, R. E. Blair, C. Blocker, B. Blumenfeld, A. Bocci, A. Bodek, V. Boisvert, G. Bolla, D. Bortoletto, J. Boudreau, A. Boveia, B. Brau, A. Bridgeman, L. Brigliadori, C. Bromberg, E. Brubaker, J. Budagov, H. S. Budd, S. Budd, K. Burkett, G. Busetto, P. Bussey, A. Buzatu, K. L. Byrum, S. Cabrera, C. Calancha, M. Campanelli, M. Campbell, F. Canelli, A. Canepa, D. Carlsmith, R. Carosi, S. Carrillo, S. Carron, B. Casal, M. Casarsa, A. Castro, P. Catastini, D. Cauz, V. Cavaliere, M. Cavalli-Sforza, A. Cerri, L. Cerrito, S. H. Chang, Y. C. Chen, M. Chertok, G. Chiarelli, G. Chlachidze, F. Chlebana, K. Cho, D. Chokheli, J. P. Chou, G. Choudalakis, S. H. Chuang, K. Chung, W. H. Chung, Y. S. Chung, C. I. Ciobanu,

M. A. Ciocci, A. Clark, D. Clark, G. Compostella, M. E. Convery, J. Conway, K. Copic, M. Cordelli, G. Cortiana, D. J. Cox, F. Crescioli, C. Cuenca Almenar, J. Cuevas, R. Culbertson, J. C. Cully, D. Dagenhart, M. Datta, T. Davies, P. de Barbaro, S. De Cecco, A. Deisher, G. De Lorenzo, M. Dell'Orso, C. Deluca, L. Demortier, J. Deng, M. Deninno, P. F. Derwent, G. P. di Giovanni, C. Dionisi, B. Di Ruzza, J. R. Dittmann, M. D'Onofrio, S. Donati, P. Dong, J. Donini, T. Dorigo, S. Dube, J. Efron, A. Elagin, R. Erbacher, D. Errede, S. Errede, R. Eusebi, H. C. Fang, S. Farrington, W. T. Fedorko, R. G. Feild, M. Feindt, J. P. Fernandez, C. Ferrazza, R. Field, G. Flanagan, R. Forrest, M. Franklin, J. C. Freeman, I. Furic, M. Gallinaro, J. Galyardt, F. Garbersen, J. E. Garcia, A. F. Garfinkel, K. Genser, H. Gerberich, D. Gerdes, A. Gessler, S. Giagu, V. Giakoumopoulou, P. Giannetti, K. Gibson, J. L. Gimmell, C. M. Ginsburg, N. Giokaris, M. Giordani, P. Giromini, M. Giunta, G. Giurgiu, V. Glagolev, D. Glenzinski, M. Gold, N. Goldschmidt, A. Golossanov, G. Gomez, G. Gomez-Ceballos, M. Goncharov, O. González, I. Gorelov, A. T. Goshaw, K. Goulianos, A. Gresele, S. Grinstein, C. Grosso-Pilcher, R. C. Group, U. Grundler, J. Guimaraes da Costa, Z. Gunay-Unalan, C. Haber, K. Hahn, S. R. Hahn, E. Halkiadakis, B.-Y. Han, J. Y. Han, R. Handler, F. Happacher, K. Hara, D. Hare, M. Hare, S. Harper, R. F. Harr, R. M. Harris, M. Hartz, K. Hatakeyama, J. Hauser, C. Hays, M. Heck, A. Heijboer, B. Heinemann, J. Heinrich, C. Henderson, M. Herndon, J. Heuser, S. Hewamanage, D. Hidas, C. S. Hill, D. Hirschbuehl, A. Hocker, S. Hou, M. Houlden, S.-C. Hsu, B. T. Huffman, R. E. Hughes, U. Husemann, J. Huston, J. Incandela, G. Introzzi, M. Iori, A. Ivanov, E. James, B. Jayatilaka, E. J. Jeon, M. K. Jha, S. Jindariani, W. Johnson, M. Jones, K. K. Joo, S. Y. Jun, J. E. Jung, T. R. Junk, T. Kamon, D. Kar, P. E. Karchin, Y. Kato, R. Kephart, J. Keung, V. Khotilovich, B. Kilminster, D. H. Kim, H. S. Kim, J. E. Kim, M. J. Kim, S. B. Kim, S. H. Kim, Y. K. Kim, N. Kimura, L. Kirsch, S. Klimenko, B. Knuteson, B. R. Ko, S. A. Koay, K. Kondo, D. J. Kong, J. Konigsberg, A. Korytov, A. V. Kotwal, M. Krepes, J. Kroll, D. Krop, N. Krumnack, M. Kruse, V. Krutelyov, T. Kubo, T. Kuhr, N. P. Kulkarni, M. Kurata, Y. Kusakabe, S. Kwang, A. T. Laasanen, S. Lami, S. Lammel, M. Lancaster, R. L. Lander, K. Lannon, A. Lath, G. Latino, I. Lazzizzera, T. LeCompte, E. Lee, S. W. Lee, S. Leone, J. D. Lewis, C. S. Lin, J. Linacre, M. Lindgren, E. Lipeles, A. Lister, D. O. Litvintsev, C. Liu, T. Liu, N. S. Lockyer, A. Loginov, M. Loreti, L. Lovas, R.-S. Lu, D. Lucchesi, J. Lueck, C. Luci, P. Lujan, P. Lukens, G. Lungu, L. Lyons, J. Lys, R. Lysak, E. Lytken, P. Mack, D. MacQueen, R. Madrak, K. Maeshima, K. Makhoul, T. Maki, P. Maksimovic, S. Malde, S. Malik, G. Manca, A. Manousakis-Katsikakis, F. Margaroli, C. Marino, C. P. Marino, A. Martin, V. Martin, M. Martínez, R. Martínez-Ballarín, T. Maruyama, P. Mastrandrea, T. Masubuchi, M. E. Mattson, P. Mazzanti, K. S. McFarland, P. McIntyre, R. McNulty, A. Mehta, P. Mehtala, A. Menzione, P. Merkel, C. Mesropian, T. Miao, N. Miladinovic, R. Miller, C. Mills, M. Milnik, A. Mitra, G. Mitselmakher, H. Miyake, N. Moggi, C. S. Moon, R. Moore, M. J. Morello, J. Morlok, P. Movilla Fernandez, J. Mülmenstädt, A. Mukherjee, T. Muller, R. Mumford, P. Murat, M. Mussini, J. Nachtman, Y. Nagai, A. Nagano, J. Naganoma, K. Nakamura, I. Nakano, A. Napier, V. Necula, C. Neu, M. S. Neubauer, J. Nielsen, L. Nodulman, M. Norman, O. Norriella, E. Nurse, L. Oakes, S. H. Oh, Y. D. Oh, I. Oksuzian, T. Okusawa, R. Orava, K. Osterberg, S. Pagan Griso, C. Pagliarone, E. Palencia, V. Pa-

padimitriou, A. Papaikonomou, A. A. Paramonov, B. Parks, S. Pashapour, J. Patrick, G. Pauletta, M. Paulini, C. Paus, D. E. Pellett, A. Penzo, T. J. Phillips, G. Piacentino, E. Pianori, L. Pinera, K. Pitts, C. Plager, L. Pondrom, O. Poukhov, N. Pounder, F. Prakhoshyn, A. Pronko, J. Proudfoot, F. Ptohos, E. Pueschel, G. Punzi, J. Pursley, J. Rademacker, A. Rahaman, V. Ramakrishnan, N. Ranjan, I. Redondo, B. Reiser, V. Rekovic, P. Renton, M. Rescigno, S. Richter, F. Rimondi, L. Ristori, A. Robson, T. Rodrigo, T. Rodriguez, E. Rogers, S. Rolli, R. Roser, M. Rossi, R. Rossin, P. Roy, A. Ruiz, J. Russ, V. Rusu, H. Saarikko, A. Safonov, W. K. Sakumoto, O. Saltó, L. Santi, S. Sarkar, L. Sartori, K. Sato, A. Savoy-Navarro, T. Scheidle, P. Schlabach, A. Schmidt, E. E. Schmidt, M. A. Schmidt, M. P. Schmidt, M. Schmitt, T. Schwarz, L. Scodellaro, A. L. Scott, A. Scribano, F. Scuri, A. Sedov, S. Seidel, Y. Seiya, A. Semenov, L. Sexton-Kennedy, A. Sfyrla, S. Z. Shalhout, T. Shears, R. Shekhar, P. F. Shepard, D. Sherman, M. Shimojima, S. Shiraishi, M. Shochet, Y. Shon, I. Shreyber, A. Sidoti, P. Sinervo, A. Sisakyan, A. J. Slaughter, J. Slaunwhite, K. Sliwa, J. R. Smith, F. D. Snider, R. Snihur, A. Soha, S. Somalwar, V. Sorin, J. Spalding, T. Spreitzer, P. Squillacioti, M. Stanitzki, R. St.Denis, B. Stelzer, O. Stelzer-Chilton, D. Stentz, J. Strologas, D. Stuart, J. S. Suh, A. Sukhanov, I. Suslov, T. Suzuki, A. Taffard, R. Takashima, Y. Takeuchi, R. Tanaka, M. Tecchio, P. K. Teng, K. Terashi, J. Thom, A. S. Thompson, G. A. Thompson, E. Thomson, P. Tipton, V. Tiwari, S. Tkaczyk, D. Toback, S. Tokar, K. Tollefson, T. Tomura, D. Tonelli, S. Torre, D. Torretta, P. Totaro, S. Tourneur, Y. Tu, N. Turini, F. Ukegawa, S. Vallecorsa, N. van Remortel, A. Varganov, E. Vataga, F. Vázquez, G. Velez, C. Vellidis, V. Veszpremi, M. Vidal, R. Vidal, I. Vila, R. Vilar, T. Vine, M. Vogel, I. Volobouev, G. Volpi, F. Würthwein, P. Wagner, R. G. Wagner, R. L. Wagner, J. Wagner-Kuhr, W. Wagner, T. Wakisaka, R. Wallny, S. M. Wang, A. Warburton, D. Waters, M. Weinberger, W. C. Wester, B. Whitehouse, D. Whiteson, S. Whiteson, A. B. Wicklund, E. Wicklund, G. Williams, H. H. Williams, P. Wilson, B. L. Winer, P. Wittich, S. Wolbers, C. Wolfe, T. Wright, X. Wu, S. M. Wynne, S. Xie, A. Yagil, K. Yamamoto, J. Yamaoka, U. K. Yang, Y. C. Yang, W. M. Yao, G. P. Yeh, J. Yoh, K. Yorita, T. Yoshida, G. B. Yu, I. Yu, S. S. Yu, J. C. Yun, L. Zanello, A. Zanetti, I. Zaw, X. Zhang, Y. Zheng, and S. Zucchelli (CDF Collaboration), *Physical Review Letters* **102**, 152001 (2009).

- [150] J. Renner, A. Farbin, J. M. Vidal, J. Benlloch-Rodríguez, A. Botas, P. Ferrario, J. Gómez-Cadenas, V. Álvarez, C. Azevedo, F. Borges, S. Cárcel, J. Carrión, S. Cebrián, A. Cervera, C. Conde, J. Díaz, M. Diesburg, R. Esteve, L. Fernandes, A. Ferreira, E. Freitas, A. Goldschmidt, D. González-Díaz, R. Gutiérrez, J. Hauptman, C. Henriques, J. H. Morata, V. Herrero, B. Jones, L. Labarga, A. Laing, P. Lebrun, I. Liubarsky, N. López-March, D. Lorca, M. Losada, J. Martín-Albo, G. Martínez-Lema, A. Martínez, F. Monrabal, C. Monteiro, F. Mora, L. Moutinho, M. Nebot-Guino, P. Novella, D. Nygren, B. Palmeiro, A. Para, J. Pérez, M. Querol, L. Ripoll, J. Rodríguez, F. Santos, J. dos Santos, L. Serra, D. Shuman, A. Simón, C. Sofka, M. Sorel, J. Toledo, J. Torrent, Z. Tsamalaidze, J. Veloso, J. White, R. Webb, N. Yahlali, and H. Yepes-Ramírez, *Journal of Instrumentation* **12**, T01004 (2017).

- [151] M. Jaderberg, V. Dalibard, S. Osindero, W. M. Czarnecki, J. Donahue, A. Razavi, O. Vinyals, T. Green, I. Dunning, K. Simonyan, C. Fernando, and K. Kavukcuoglu, (2017), arXiv:1711.09846 .
- [152] B. J. Wythoff, *Chemometrics and Intelligent Laboratory Systems* **18**, 115 (1993).
- [153] H. H. B. Sørensen (Springer, Berlin, Heidelberg, 2012) pp. 377–386.
- [154] J. Gauci and K. Stanley, in *Proceedings of the 9th Annual Conference on Genetic and Evolutionary Computation, GECCO '07* (ACM, New York, NY, USA, 2007) pp. 997–1004.
- [155] N. Chatterjee, M. O'Connor, G. H. Loh, N. Jayasena, and R. Balasubramonian, in *Proceedings of the International Conference for High Performance Computing, Networking, Storage and Analysis, SC '14* (IEEE Press, Piscataway, NJ, USA, 2014) pp. 128–139.
- [156] G. Wang, S. Chen, X. Zhang, and Z. Zhou, *Information Processing Letters* **112**, 823 (2012).
- [157] NVIDIA Corporation, *NVIDIA CUDA Compute Unified Device Architecture Programming Guide* (NVIDIA Corporation, 2007).
- [158] S. Williams, A. Waterman, and D. Patterson, *Communications of the ACM* **52**, 65 (2009).
- [159] KARMEN Collaboration, *Physics Letters B* **B267**, 321 (1991)